Silesian
University
of Technology

Faculty of Energy and Environmental Engineering
Department of Thermal Technology
Discipline of Environmental Engineering, Mining, and Energy

Mieszko Tokarski

Computational and experimental analysis of a condensation hood

PhD Thesis

Supervisor: Ziemowit Ostrowski, PhD, DSc, Assoc. Prof.
Auxiliary Supervisor: Arkadiusz Ryfa, PhD, Asst. Prof.

Gliwice, September 2021

Contents

Acknowledgements

First and foremost, I would like to express my great gratitude to my supervisors Dr Ziemowit Ostrowski and Dr Arkadiusz Ryfa, who guided me in doing this thesis. They provided me with invaluable advice and helped me in difficult periods. Dr Arkadiusz Ryfa contributed tremendously to the successful completion of the project, within which this thesis was carried out.

Secondly, I would like to thank Prof. Andrzej J. Nowak who helped me by giving me advices, providing knowledge and experience beyond the comprehension.

Also I would like to thank Retech company in the persons of Mr. Bogusław Ziarko, Mr. Krzysztof Ziarko, Mr. Andrzej Ziarko, and Mr. Andrzej Kuroś, for invaluable help and patience in fulfilling the expected and unexpected tasks and my requests.

At last, but not in least, I would like to thank my family, friends, and everyone who helped and motivated me to work on this work for their support. Without that support, I couldn't have succeeded in completing this work.

The financial assistance was provided by grant no. POIR.03.02.01-18-0019 15-00 funded by the Polish Agency for Enterprise Development (PARP), Poland, and I would like to acknowledge it here.

Nomenclature

Latin symbols

$\dot{H}$	enthalpy rate, kW
$\dot{m}$	mass flow rate, kg/s
$\dot{Q}$	rate of heat flow, kW
A	area, m^2
c	specific heat, kJ/(kg K)
d	diameter, m
h	specific enthalpy, kJ/kg
k	thermal conductivity, W/(m$^2 \cdot$ K)
L	length, m
M	molar mass, kg/kmol
p	pressure, Pa
R	thermal resistance, (m$^2 \cdot$ K)/W
T	temperature, K
t	temperature, °C
V	volume, m^3
w	humidity ratio, (kg of moisture)/(kg of dry air)

Greek symbols

η	efficiency, %
ϕ	relative humidity, -
ρ	density, kg/m^3

σ, n	thickness, m
ε	correction factor, -
h	heat transfer coefficient, $kW/(m^2 \cdot K)$
v	velocity, m/s

Superscripts

$\overline{}$	mean value

Subscripts

$I - V$	balance element
a	air
ad	additional
av	average
$bundle$	pipe bundle
c	convection
ch	condensation-hood
$component$	here: air or steam
$cond$	condensate
da	dry air
fg	vaporization
ha	humid air
l	liquid
p	at constant pressure
ref	reference
s	saturation
st	source term
$steam$	steam
v	moisture

Abbreviations

BC	Boundary Condition
CH	Condensation Hood
CS	Combi steamer
F	Fan
HE	Heat Exchanger
L & P	Left & Right, respectively
MC	Modified Construction
OC	Original Construction
RC	Redesigned (New) Construction
UDF	User Defined Function
UI	Uniformity Index, -
WP	Wall Pipe

Dimensionless Numbers

Nu	Nusselt Number, -
Pr	Prantl Number, -
Re	Reynolds Number, -

Chapter 1

Introduction

Due to technological progress, a living standard and wealth increase along with the quality of goods and services improvement. Such a situation fuels market competition in many industry branches leading to the improvement of cost efficiency, work conditions, quality, and diversity of the final products. A good example of how technology pervades industry is catering sector, and to be more specific - a combi-steamer: a device of numerous advantages characterised by its considerable versatility that transformed the majority of contemporary kitchens over the last two decades. In case of gastronomy, establishments and facilities attach a lot of value to as trivial thing as a floor space. A single combi-steamer can replace even several conventional appliances maintaining their functionality, productivity, and allowing for a programmable operation - a time- and effort-saving feature especially valuable in labor-intensive work like gastronomy. The combi-steamer utilises steam in the food preparation process after which the steam, accompanied by odour, becomes a primary byproduct that can negatively affect the work area, staff, and meals if not removed promptly after release. Dedicated infrastructure for steam and odour removal is expensive, often problematic, occupies additional space, and requires the combi-steamer to be in a fixed location. When the oven's mobility becomes essential for the kitchen to work normally, so-called condensation hoods (CH) come up as a cheaper and promising alternative.

The condensation hood is an additional combi-steamer component and does not require any additional floor space. CH captures the steam produced by the combi-steamers, condenses it, and returns the condensate back to the oven by gravitational force or directly to the sewage. Hence, additional mobility of the oven is provided so any stationary infrastructure becomes unnecessary. Such mobility brings also additional benefits: combi-steamers with condensation hoods can be used in places without proper infrastructure and the kitchen's work organisation including transport, cleaning, and technical maintenance becomes easier and more flexible. Additionally, combi-steamers with condensation hoods tend to be more cost-efficient and more energy saving than conventional appliances. That is why the condensation hoods, along with combi-steamers, are nowadays an omnipresent and an inherent element of the modern gastronomy facility [22, 17].

The compact design of the CH and the number of heat and flow processes that take place in this device, make an investigation of such an appliance a very demanding task. The core element of the condensation hood is a heat exchanger (HE) – the most expensive part that requires the most manufacturing time and effort. The HE works as an air-cooled steam condenser. The combi-steamer provides an air-steam mixture of unknown fractions to the CH. Next, the steam contained in the mixture is condensed and the rest (uncondensed steam) is diluted in the coolant air and finally released to the environment (the kitchen). In the ideal case, the whole steam produced by the combi-steamer should be condensed and returned to the oven. Otherwise, the work zone will likely be contaminated by excessive water vapour, which may have a negative impact on a food under preparation, electrical devices, and on the staff's comfort. For this reason, the condensation hood should be as efficient as possible, and hence, the design and investigation of such appliances in terms of condensation efficiency requires advanced engineering tools, such as computational fluid dynamics (CFD). CFD allows for a preliminary diagnosis and improvement of the device's first concept before it is constructed, installed, and tested. Due to different reasons, e.g., limited computational resources and time, the development of a reliable CFD model often comprises of a compromise between the exact representation of the important phenomena and a simplified approach to simulate them. However, to keep the compromise's impact on the results insignificant, a comprehensive knowledge concerning the ways for simulation of those phenomena is required [36].

Despite the well-established position in the market, any scientific publications analysing conjugate heat and mass transfer processes encountered in the condensation hoods are practically not available. However, component phenomena are typical and their modelling approach has already been investigated in other applications. The most important phenomenon is the condensation of the air-steam mixture coupled with the species transportation process [10, 46, 11, 8, 49], the heat transfer in externally finned pipes with plain circular fins [18, 1, 12, 6, 26, 37], the heat transfer and fluid flow in internally finned pipes [21, 19, 48, 34, 23, 28], and also tube bundle configuration analysis [30, 9, 7, 16, 35, 51, 45, 25].

The condensation hood consists of two main parts: an inlet part covering the filters and baffles, and a fan that forces the air (from the environment) to flow through the device; and the second part consisting of the heat exchanger and the outlet zone. In heat exchanger the humid air from the environment (low moisture content) works as a coolant while (most probably) mixture of the air and steam (high moisture content) provided by the combi-steamer is cooled. As a result of this cooling, the high moisture content (steam) eventually condensates. While pure steam condensation process is well described in most heat transfer-related handbooks, in the presence of non-condensable gases (like in most cases - the air) such process still needs further investigation according to a specific needs. For instance, Jiqiang Su [38] with use of commercial CFD software and experimental data, investigated the impact of air content on steam condensation process over a vertical surface. Guangming Fan [14] developed a new empirical correlation for steam condensation in terms of pressure, air content, and wall subcooling in a vertical smooth tube. Noori Rahim Abadi [31] examined numerically the steam condensation process inside a long, inclined, smooth tube at different saturation temperatures with assumption of the flow field being three-dimensional, unsteady and turbulent. He also carried out a thorough literature review dedicated to condensation inside smooth tubes. Haozhi Bian [8] took up steam condensation process in tube bundles and performed numerical simulations on various cases. His research showed that tube bundles' configuration has a significant effect on the heat transfer coefficient in comparison to a single tube case. Alan O'Donovan [32] investigated experimentally and mathematically pressure drop impact on the steam condensation process in air-cooled tube bundles. Due to a combination of frictional, momentum and gravitational effects and excessive pressure drop may significantly affect the heat exchanger's output. G. I. Tarasov [40] carried out experimental studies of heat transfer during steam condensation on slightly inclined tubes' bundle with and without non-condensable gases at different steam pressures. Guangming Fan [15] in his work conducted experimental study of pure steam and air-steam mixture condensation on vertical corrugated and smooth tubes, respectively. Those studies were carried out under different pressures and air content of the air-steam mixture.

Wide-ranging experimental and numerical studies regarding the steam condensation process in terms of numerous parameters prove that the condensation phenomenon (especially air-steam mixture) still needs investigation. Thus, the design of an efficient air-cooled condenser becomes challenging along with conducting reliable measurements.

The heat exchanger under consideration works with ambient humid air as a coolant. This type of heat exchanger is widely used in diverse applications and scales - from cooling electronic components [47] through refrigeration [41], as a car coolers [20], and air conditioning [24] to a large scale condensers used in power and chemical industries [41, 2]. Those solutions have one thing in common - the heat is transferred from a hot fluid to an ambient air. The air flows outside of the pipes, while the steam condenses inside, so the dominant thermal resistance occurs on the air side as the convective heat transfer coefficient is higher for condensation [9]. For this reason, pipes are frequently externally finned.

The typical configuration is different when water is used as a coolant. Water flows inside the pipes while the steam condenses on the outside of the pipes. As the heat transfer coefficient for water is higher than for air, and there is no need for applying fins. As for the initial condensation hood, steam condenses outside the pipes and the coolant (humid air) flows through the pipes. As a consequence, there is a need of reducing the thermal resistance inside the tubes. Therefore, an internally finned pipes (with longitudinal fins) are used. Such a solution, although widely used in many industrial branches like power engineering [50, 29, 48], petroleum processing [48] or electronics [48, 21, 29], is not described in detail by standard general dimensionless correlations. Majority of works concerning internally finned tubes in various applications are focused on numerical [50, 48, 29] and/or experimental studies [19, 50] in laminar [21] and/or turbulent flow regimes [50, 29, 48] in strictly specified, particular cases.

For this reason, design of such devices, regardless of the application, requires substantial resources accompanied by extensive research. This is also the reason for this PhD Thesis that was carried out within project no. POIR.03.02.01-18-0019/15-00 funded by the Polish Agency for Enterprise Development, Poland, in cooperation with industrial partner - Retech Ltd. The project, titled "Wdrożenie do produkcji nowej generacji pochłaniaczy pary do pieców konwekcyjno-parowych / Implementation of a new generation of condensation hoods for combi-steamers". The project covers further development of the existing appliance by means of numerical methods.

Chapter 2

Aim and scope of the work

The main aim of this thesis was the development of a new generation of condensation hoods that could be then introduced to the market.

The thesis covers the analysis of the processes involved in steam condensation and heat exchange in condensation hoods. Then, the numerical models of three condensation hood constructions were developed: original (OC), modified (MC), and redesigned (RC).

All numerical models were developed in Ansys Fluent and each was validated against experimentally collected data. In Figure 2.1 a general organisation of this work is presented.

The first model concerns the **original construction** (OC), already produced and tested experimentally device [42]. The model was used as a benchmark to diagnose the condensation hood, learn how to set up the model, and to find potential improvements. Its development and validation is described in [44].

The model of the **modified construction** (MC) was developed based on the original construction and includes the most promising improvements to its HE design maintaining rest of the device unchanged. As a result, the construction has been simplified with high condensation efficiency maintained. Once the numerical results regarding the condensation efficiency were satisfying, a CH prototype has been built and tested in a laboratory environment. Development and validation of this model is also described in [44].

Model of the **redesigned construction** (RC) covers a thorough redesign of the heat exchanger, which allowed to utilise available space more efficiently. As a conse-

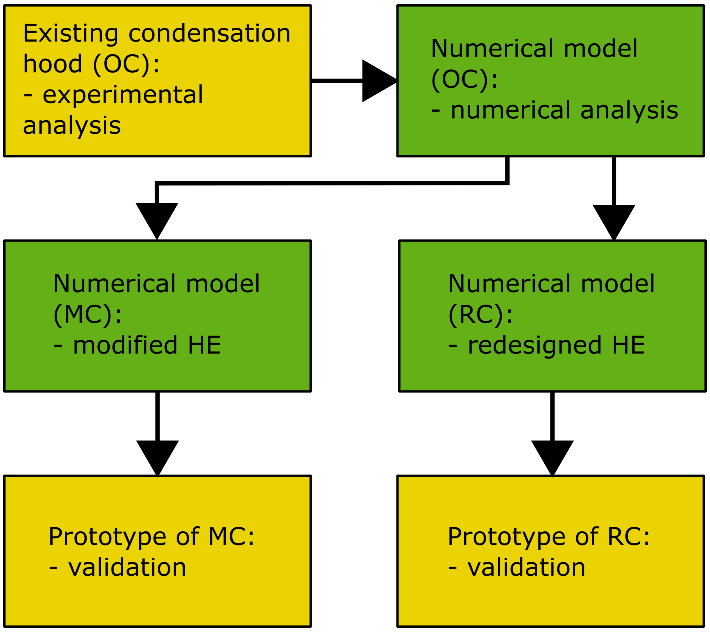

Figure 2.1: General plan of this thesis. OC - original construction; MC - modified construction; RC - redesigned construction.

quence, even higher condensation efficiency (compared to both previous constructions) has been achieved. The design of RC was used to build a second prototype, whose development and validation is presented in [43].

Chapter 3

Condensation hood - construction and operation principle

The condensation hood is a device designed to work with a combi-steamer. Both appliances share steam-condensate cycle, as presented in the right hand side part of Figure 3.1, while in left hand side part of Figure 3.1 a standalone oven is showed. As indicates Figure 3.1 (right), the water is provided to the combi-steamer by water supply (1), then evaporated in steam generator (d), and directed to the working chamber (e), where food is being prepared. In the working chamber, the steam has direct contact with food, which means it can carry grease, scents, and solid particles. Such polluted steam mixes with air and is released to the kitchen (c) through steam outlet IV and during opening oven's door (V) to load/unload or inspect the working chamber (e). The steam outlet IV can be just as presented, but also can consist of an additional vent to lead out the steam from the kitchen, or, as shown in Figure 3.1.b, can connect the oven with the condensation hood. The condensation hood, supplied by the oven with the steam-air mixture, condenses the steam in HE and returns the condensate back to the combi-steamer, as indicated by arrow (III). The returned condensate can be evaporated in the steam generator (d) again, which results in less water and energy consumption - the condensate is subcooled but still warmer than fresh water from the water supply. However, not all steam is condensed, so the system is not fully closed - some of the steam is mixed with coolant air (I), that is sucked by the fan (F), then flows through the HE and is released back to the kitchen (c), as indicated by arrow (II).

The condensation hood's schematic diagram is presented in Figure 3.2, where inlets

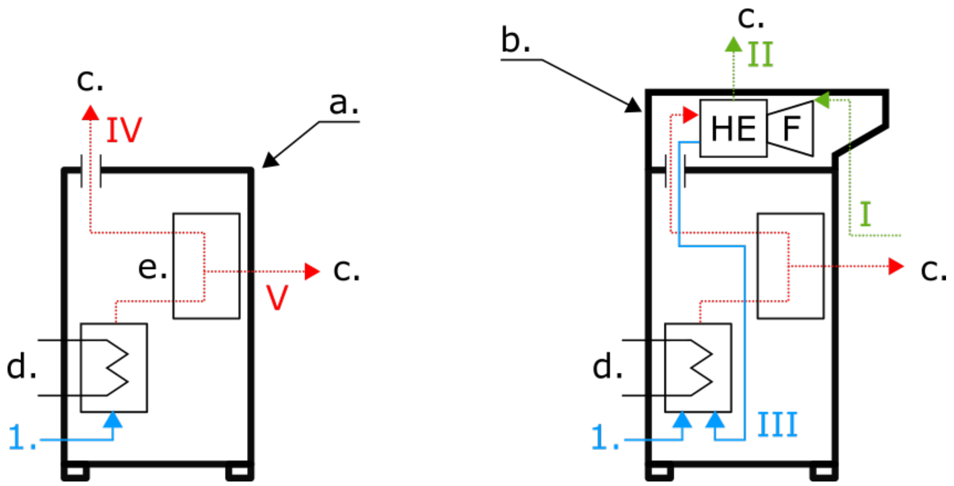

Figure 3.1: Condensation hood & its purpose: standalone combi-steamer (left hand side); combi-steamer with condensation hood (right hand side); HE - heat exchanger; F - fan; a. - combi-steamer; b. - condensation hood; c. - kitchen; d. - steam generator; e. - working chamber; 1. - water supply; V. - steam released from working chamber; I - coolant air intake; II - air outlet; III. - condensate outlet (recirculation); IV - steam outlet.

and outlets mentioned in Figure 3.1 are also indicated. The figure presents the main flow direction throughout the condensation hood. Air flow is forced by a fan (F) located in the middle of the device and is sucked through the air inlet (I). Then, the air is pushed into a heat exchanger HE. Next, while leaving the HE, the air is released to the environment. The steam is provided by the combi steamer via inlet (IV) directly to the HE where is condensed by the coolant air. The condensate leaves the heat exchanger through the outlet (III), leaves the CH, and is returned to the oven.

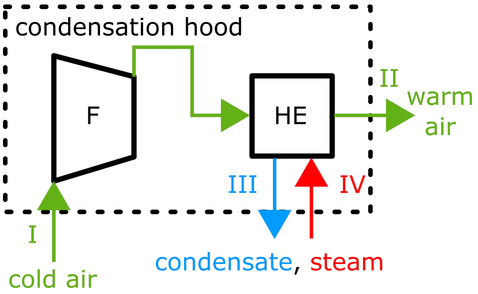

Figure 3.2: Condensation hood - main flows. F - fan; HE - heat exchanger; I - air inlet; II - air outlet; III - condensate outlet; IV - steam inlet.

Chapter 4

Original construction

4.1 Operation principle

In this chapter, a condensation hood already produced by Retech Ltd. is described. The device is called ConvoVent 4 and is designed for ConvoTherm 4 combi-ovens. Figure 4.1 presents the discussed appliance located at the top of an exemplary oven.

Figure 4.1: ConvoVent 4 condensation hood and a combi-steamer. *Courtesy of Retech Ltd. Used by permission.*

Contrary to Chapter 3, where general condensation hood operation principle is described, the original condensation hood is discussed in detail here.

The original construction is presented in Figure 4.2, where core elements are highlighted. The coolant air (green arrow) is sucked by the fan (1) located in the central part of the device through the inlet (I) consisting of a front baffle. The baffle consists of several metal sheets bent vertically in blind-like way to prevent particulate matter entering the CH and for aesthetic purposes.

Then, the air flows through a grease filter located in the rectangular openings on both sides of the fan. Sucked by the fan, the air gets to the central air distribution chamber (2) (dashed black rectangle in Figure 4.2.b), that separates tube bundles (4) – (4.a) and (4.b) – and is pushed further into the bundles (4). After leaving the bundles, the air gets to peripheral air pockets (3), where the flow direction changes upwards to eventually leave the appliance through the air outlet (II), as indicated by the green arrows in Figure 4.2.d, located above the heat exchanger. Outlet (II) consists of a final filter made of a fine two-layered fabric separating droplets and fine solid particles.

Both steam inlets (IV) are located on the left hand side at the very beginning of the bundle (4.a), which means the bundle (4.a) is provided with steam directly, whereas bundle (4.b) is additionally separated by a relatively narrow connecting channel (5) indicated as a dashed box in Figure 4.2.a. This significantly extends the way the steam needs to flow. While the steam condensates on the pipes, the condensate flows in the opposite direction according to the slope of the bottom wall (Figure 4.2.c), to the condensate outlet III - where the condensate flows in counterflow to the steam through the same conduit.

Uncondensed steam should travel through the apertures (6) – presented in Figure 4.2.b and 4.2.c as white dashed rectangles – where is diluted in the coolant air, then introduced to the distribution chamber (2), and further into the pipes. Apertures (6) - one per bundle - connect the heat exchanger's steam side to the fan inlet zone's air side.

Figure 4.3.a highlights the fan and the HE presented in detail in Figure 4.3.b and in Figure 4.3.c. The heat exchanger consists of two pipe bundles connected by a narrow channel. The bundles consist of 24 pipes per bundle (48 pipes in total) in an in-line arrangement: 3 rows and 8 columns as presented in Figure 4.3.c. The coolant air (green arrows) is pushed by the fan into the space between the bundles and then distributed to the pipes. On the steam side, both steam inlets are located in the left hand side

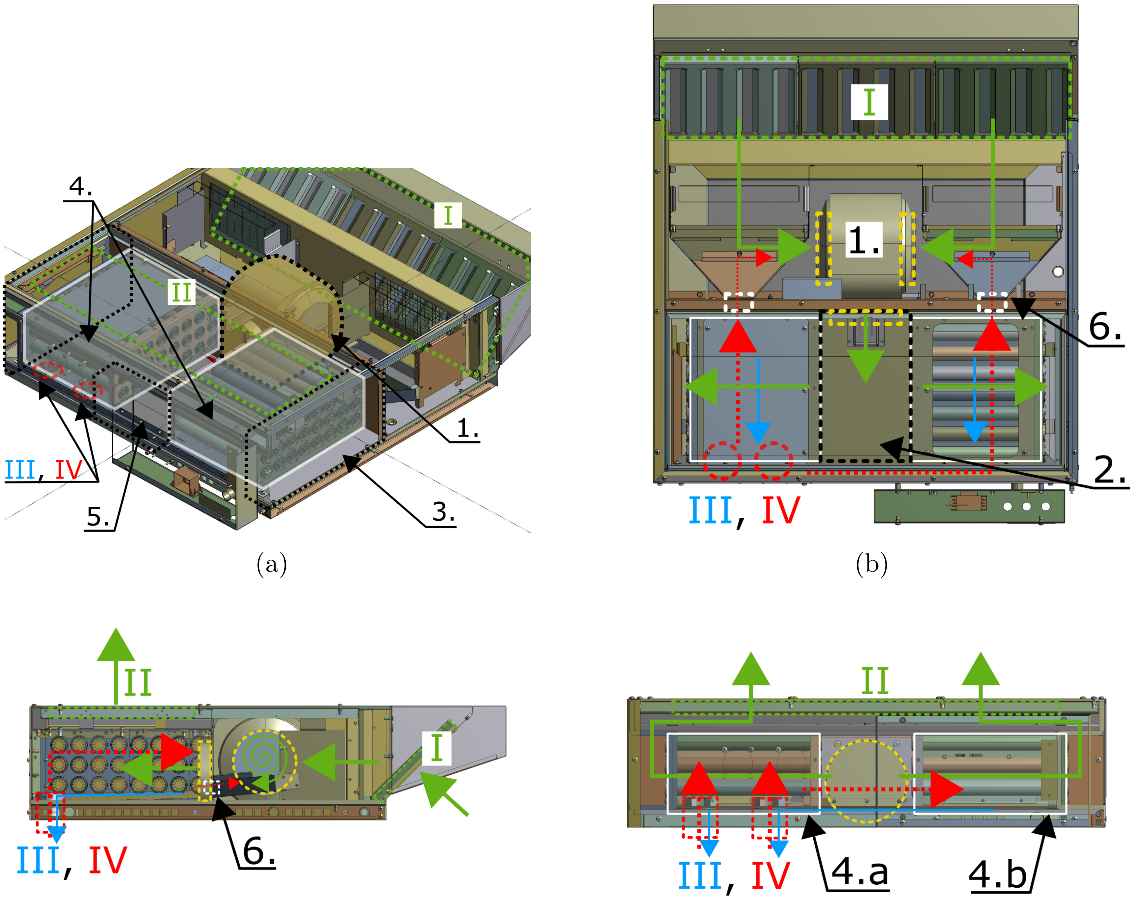

(a) (b)

(c) (d)

Figure 4.2: Condensation hood - original construction: a) top view; b) side view; c) rear view; I - coolant air intake; II - air outlet; III. - condensate outlet; IV - steam inlet; 1 - fan; 2 - air distribution chamber; 3 - air pockets; 4.a - left hand side tube bundle; 4.b - right hand side tube bundle; 5 - bundle connection channel; 6 - apertures. Figure adapted from images courtesy of Retech Ltd.

bundle. Such a situation suggests that the steam will more likely propagate into the left hand side bundle than into the right hand side due to the longer travelling path and higher flow resistance. The steam flows through the bundle as indicated by the red arrows in Figure 4.3.c, where two baffles (two per bundle) extend path the steam needs to cover. The baffles are symmetrical in both bundles. The first one is located between the 4th and 5th column and allows the steam to pass it beneath, while the second baffle is located between the 7th and 8th column and is passed by the steam from above. In Figure 4.3.c a sloped bundle bottom is indicated, which enables gravitational condensate removal from the HE according to the blue arrow.

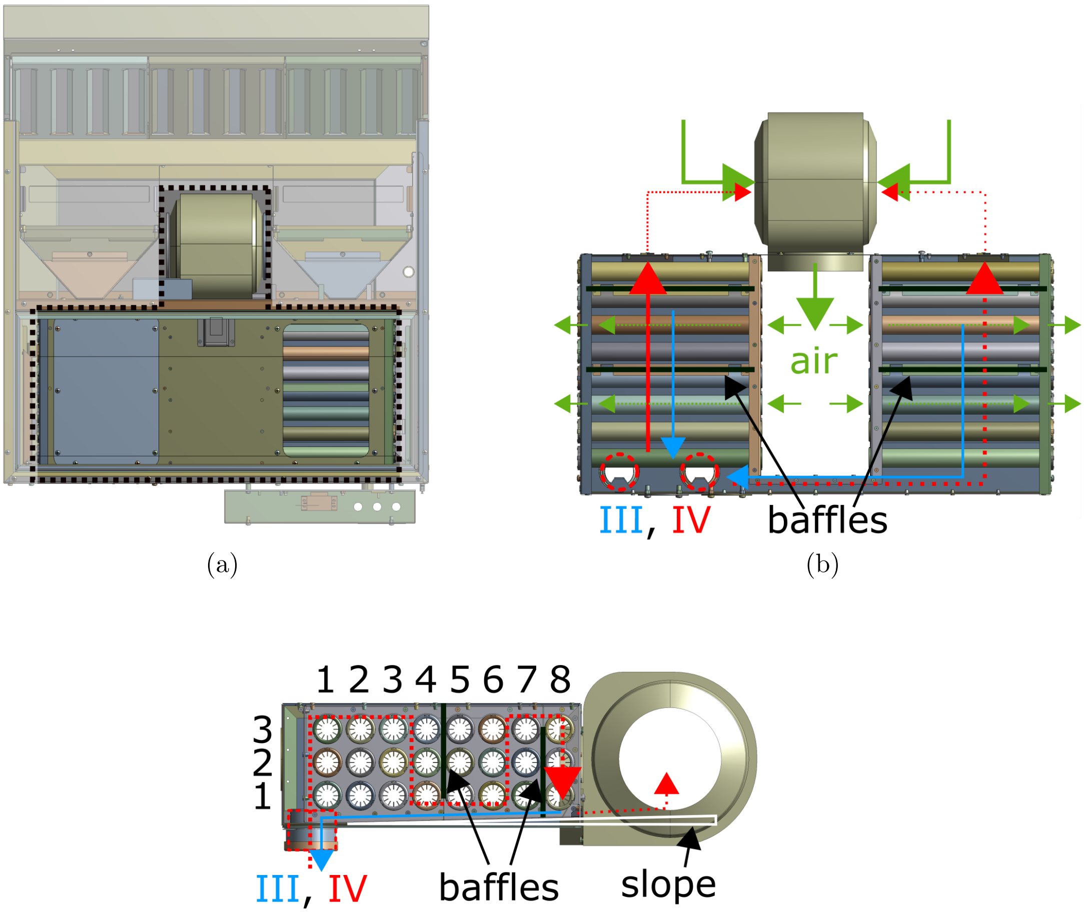

(a) (b)

(c)

Figure 4.3: Condensation hood - original construction: a) top view; b) HE top view; c) HE side view; III. - condensate outlet; IV - steam inlet; vertical 1-3 - row numbers; horizontal 1-8 - column numbers. Figure adapted from images courtesy of Retech Ltd.

As the steam condenses on the tube's outer wall and the coolant air flows inside, the dominant thermal resistance occurs on the air side. Thus, the pipes are internally finned as shown in Figure 4.4. In Figure 4.4.a a tube cross section is presented with main dimensions indicated, whereas in Figure 4.4.b whole pipe is shown in isometrical view with main flow direction. There are 12 equally distant longitudinal fins inside the pipe, each fin of the same thickness as the external wall: δ=0.001 m. Fin height L_{fin} = 0.006 m corresponds to about a quarter of the tube diameter D_{pipe} = 0.03 m. The pipe's outer wall is smooth and the pipe is 0.282 m long.

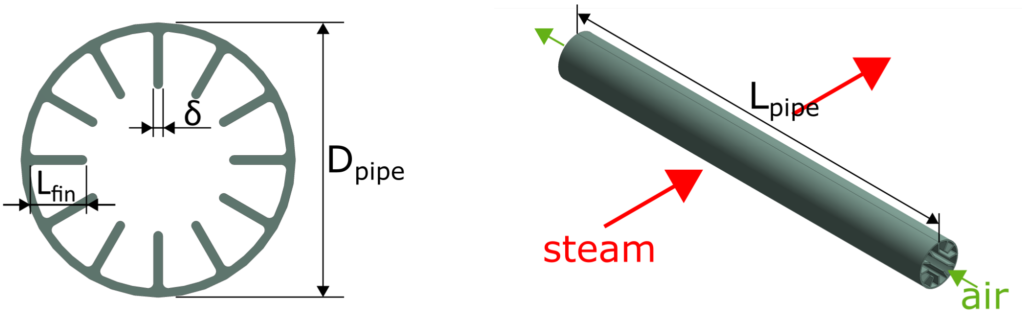

(a) (b)

Figure 4.4: Tube used in the condensation hood: a) cross sectional view; b) isometric view. $D_{pipe} = 0.03$ m - pipe external diameter; $\delta = 0.001$ m - wall and fin thickness; $L_{fin} = 0.006$ m - fin height; $L_{pipe} = 0.282$ m - pipe length. Figure adapted from images courtesy of Retech Ltd.

4.2 Measurements

In the condensation hood, the steam condenses outside the pipes and coolant (humid air) flows through the pipes. Hence, there is a need to reduce the thermal resistance on the coolant side. Therefore, an internally finned pipes (with longitudinal fins) are used. Although fins are widely applied in many industrial branches like power engineering [29, 48], petroleum processing [48] or electronics [21, 29], solution with internal fins is not described in detail by well-known standard general dimensionless correlations. Majority of works concerning internally finned tubes are focused on numerical and experimental studies [48, 29, 19, 21], where experimental data is required for validation.

A comprehensive investigation of the CH equipped with a nonstandard heat exchanger, that covers numerical model development and improvements to the construction, requires extensive experimental work and multiple measurements. A mathematical model of conjugate heat and mass transfer processes, including condensation of steam taking place within CH was developed to assess and validate the experimental data. The model is based on mass and energy balance equations, similarly as in other publications [39, 27, 13, 33, 52].

Mass flow rates were measured along with temperature and air humidity. Steam generator was built to control the flow of the steam through the device. Its interaction with a dedicated combi-steamer was also investigated.

4.2.1 Mathematical model

Preliminary diagnosis of the condensation hood requires a mathematical model. This model is based on three balances written for steady-state: mass balance of dry air, moisture balance, and energy balance. It requires information about the velocity, temperature, and humidity at the inlets and outlets of the device. Figure 4.5 presents the hood's inlets, outlets, and necessary quantities at the points I-V:

I - air inlet: temperature, relative humidity and velocity.

II – air outlet: temperature, relative humidity and velocity.

III – condensate outlet: mass and time.

IV – steam inlet: temperature.

V – heat losses: temperature of the housing.

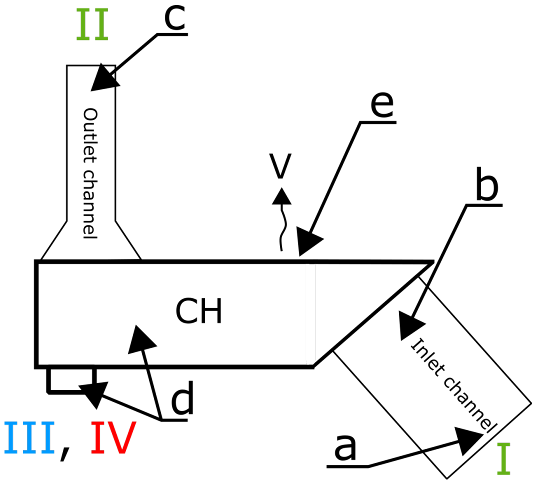

Figure 4.5: Locations of measured quantities at point: (a): t, p; (b) and (c): t, v, ϕ; (d): t, v; (e): t; t - temperature, v - velocity, ϕ - humidity, p - pressure.

Mass balance of dry air

According to the mass conservation principle, in open systems in steady-state, total amount of matter, that is inflowing and outflowing of the system, should be equal. However, there is always some uncertainty resulting from the measurement error. Hence, the mass balance of dry air takes the form

$$\dot{m}_{da,I} = \dot{m}_{da,II} + \Delta\dot{m}_{da} \tag{4.1}$$

where $\dot{m}_{da,I}$ and $\dot{m}_{da,II}$ are mass flow rates of dry air at air inlet and outlet respectively, kg/s, $\Delta\dot{m}_{da}$ is balance of dry air inconsistency, kg/s. This last quantity is in some sense a measure of the measurement accuracy of dry air mass flow rates at points *I* and *II*.

Direct measurements bring information about the mass flow rate of humid air and the obtained results need to be converted considering the air humidity ratio [9]. To do so, according to Eq.(4.2) humidity ratio is needed.

$$\begin{aligned} \dot{m}_{da,I} &= \dot{m}_{ha,I}\tfrac{1}{(1+w_I)} \\ \dot{m}_{da,II} &= \dot{m}_{ha,II}\tfrac{1}{(1+w_{II})} \end{aligned} \tag{4.2}$$

where $\dot{m}_{ha,I}$ and $\dot{m}_{ha,II}$ are mass flow rates of humid air at point (I) and (II), respectively, kg/s, w_I and w_{II} are humidity ratios at points (I) and (II), respectively, (kg of moisture)/(kg of dry air).

Mass flow rate of humid air can be expressed as

$$\begin{aligned} \dot{m}_{ha,I} &= A_I\overline{v}_I\rho_{ha,I} \\ \dot{m}_{ha,II} &= A_{II}\overline{v}_{II}\rho_{ha,II} \end{aligned} \tag{4.3}$$

where A_I and A_{II} are cross-sectional areas of the channels at points (I) and (II), respectively, m^2, $\overline{v}_I$ and $\overline{v}_{II}$ are average air velocities at points (I) and (II), respectively, m/s, and $\rho_{ha,I}$ and $\rho_{ha,II}$ are air density at points (I) and (II), respectively, kg/m^3.

Humidity ratio [9] in Eq.(4.2) is defined as

$$\begin{aligned} w_I &= \tfrac{\phi_I p_s}{p_{ref}-\phi_I p_{s,I}}\tfrac{M_{h_2o}}{M_a} \\ w_{II} &= \tfrac{\phi_{II} p_s}{p_{ref}-\phi_{II} p_{s,II}}\tfrac{M_{h_2o}}{M_a} \end{aligned} \tag{4.4}$$

where ϕ_I and ϕ_{II} stand for relative humidity, $p_{s,I}$ and $p_{s,II}$ are saturation pressures of water at temperature at points (I) and (II), respectively, Pa, p_{ref} is reference pressure (here atmospheric pressure), Pa, M_{h_2o} is molar mass of water, kg/kmol and M_a is molar mass of dry air, kg/kmol.

The same equations apply to the outlet air (point (II)) as well.

Moisture balance

The principle of mass conservation applies to the moisture balance as well. Equation (4.5) concerns balance of the condensation hood, so it consists of the following elements

$$\dot{m}_{v,I} + \dot{m}_{steam,IV} = \dot{m}_{v,II} + \dot{m}_{cond,III} + \dot{m}_{cond,IV,ad} \tag{4.5}$$

where $\dot{m}_{v,I}$ is moisture flow rate at the inlet, kg/s, $\dot{m}_{steam,IV}$ is steam input, kg/s, $\dot{m}_{v,II}$ is moisture flow rate at the outlet, kg/s, $\dot{m}_{cond,III}$ is the condensate flow rate, kg/s and $\dot{m}_{cond,III,ad}$ stands for the additional condensate flow rate fulfilling the balance, kg/s.

Moisture flow rates at the inlet (I) and outlet (II) of the condensation-hood are defined as follows

$$\begin{aligned} \dot{m}_{v,I} &= \dot{m}_{da,I} w_I \\ \dot{m}_{v,II} &= \dot{m}_{da,II} w_{II} \end{aligned} \tag{4.6}$$

Energy balance

The energy balance, similarly to the mass balance, has been extended by the energy balance inconsistency $\Delta \dot{H}$. Eventually, the energy balance of the condensation hood takes the form

$$\dot{H}_I + \dot{H}_{IV} = \dot{H}_{II} + \dot{H}_{III} + \dot{Q}_V + \Delta \dot{H} \tag{4.7}$$

where $\dot{H}_I$ stands for rate of air enthalpy at the inlet, kW, $\dot{H}_{IV}$ is steam enthalpy rate, kW, $\dot{H}_{II}$ is air enthalpy rate at the outlet, kW, $\dot{H}_{III}$ is condensate enthalpy rate, kW, $\dot{Q}_V$ stands for heat losses rate, kW and $\Delta \dot{H}$ is energy balance inconsistency, kW. This last quantity is in some sense a measure of the measurement accuracy of all thermal quantities involved in the energy balance.

Air enthalpy rates [9] at points (I) and (II) are calculated as follows

$$\begin{aligned}\dot{H}_I &= \dot{m}_{da,I}\Big[c_{p,a}(T_{a,I} - T_{ref}) + w_I\Big(h_{fg} + c_{p,steam}(T_{a,I} - T_{ref})\Big)\Big] \\ \dot{H}_{II} &= \dot{m}_{da,II}\Big[c_{p,a}(T_{a,II} - T_{ref}) + w_{II}\Big(h_{fg} + c_{p,steam}(T_{a,II} - T_{ref})\Big)\Big]\end{aligned} \tag{4.8}$$

where $c_{p,a}$ stands for air specific heat, kJ/(kg K), $T_{a,I}$ and $T_{a,II}$ are temperatures of air at points (I) and (II), respectively, K, T_{ref} is reference temperature, K, h_{fg} stands for enthalpy of vaporization (latent heat), kJ/kg and $c_{p,steam}$ is specific heat of steam, kJ/(kg K).

Enthalpy rate of the steam is calculated as a product of steam mass flow rate and its specific enthalpy.

$$\dot{H}_{IV} = \dot{m}_{steam,IV} h_{steam} \tag{4.9}$$

where h_{steam} stands for the specific enthalpy of the steam, kJ/kg.

Enthalpy rate of the condensate is relatively low in comparison to other terms of the energy balance (4.7), but it has been taken into account and derived as follows

$$\dot{H}_{III} = \dot{m}_{cond,III} c_{p,water}\Big(100 - t_{cond,III}\Big) \tag{4.10}$$

where $c_{p,water}$ stands for specific heat of water, kJ/(kg K) and $t_{cond,III}$ is temperature of the condensate, °C.

Heat losses were the second element of the balance that could be neglected due to its insignificant value.

$$\dot{Q}_V = h_c A_{th}(\overline{T}_{th,V} - T_{amb}) \tag{4.11}$$

where h_c is average convective heat transfer coefficient, kW/(m^2 K), A_{th} is a heat transfer surface area, m^2 and $\overline{T}_{th,V}$ is an average temperature of the heat transfer surface, K.

Condensation efficiency

The main function of the condensation hood is steam condensation. Hence, the condensation efficiency becomes the most important parameter calculated as follows

$$\eta = \frac{\dot{m}_{cond,III}}{\dot{m}_{steam,IV}} 100\% \tag{4.12}$$

4.2.2 Measurement methodology

Experimental rig was prepared together with the measurement procedure. Inlet and outlet channels were identified (see figure 4.5) to mount the sensors and and form a plug flow where the sensors were located.

Good quality measurements are necessary to build a reliable mathematical model. Thus, it becomes crucial to prepare an appropriate experimental rig along with the measurement procedure including measured values and measurement devices (also taking into account their number, location, accuracy, range, and measurement conditions).

The following probes were used during the measurements:

P-a: Omniport30 Logprobe 16 – temperature (-20. . . 70°C ±0.5°C), pressure (900. . . 1100 hPa ±0.5hPa), realtive humidity (0. . . 100% ±2% for 0. . . 90% and ±3% for 90. . . 100%).

P-b: Omniport30 Logprobe 65 - velocity (0. . . 20 m/s ±0,2 m/s), temperature (0. . . 50°C ±1°C).

P-c: Delta Ohm HD29371TC. . . /HD29V371TC – velocity (0.05. . . 20 m/s ±0,7 m/s+3% of the value), temperature (-10. . . 60°C ±0.3°C), relative humidity (0. . . 100% ±1.5% for 10. . . 90% and ±2% for the remaining range).

P-d: Dwyer 167-12" Pitot tubes with Dwyer Magnesense II Differential Pressure Transmitter – velocity (0. . . 20 m/s ±1% up to 50Pa).

P-e: Dwyer 160-36" Pitot tubes with Dwyer Magnesense II Differential Pressure Transmitter – velocity (0. . . 20 m/s ±1% up to 50Pa).

P-f: Thermocouples type K – temperature (-60. . . 375°C ±0.1°C).

Readings from all sensors except for (P-a) and (P-b) were recorded by Brainchild PR20 Readings signal recorder. To properly measure the velocity of the air inlet and outlet, additional channels were introduced according to Figure 4.5. They also allowed for uniformization of the velocity profile at the velocity probes location. The measurement probes were precisely mounted in these channels. The inlet channel was a cuboid with a constant rectangular cross-section along its entire length. It was well-fitted within the condensation hood to eliminate air leakage.

Two Pitot tubes (P-e) were placed in the geometrical centers of both halves of the inlet channel cross-section 600 mm away from the inlet to the channel, as indicates Figure 4.5 at point (b). Additionally, ambient pressure, temperature, and relative humidity were measured and allowed for determining of the humidity ratio at point (I) with use of probe (P-a). The velocity profile at this point were verified with the use of the probe (P-b) by manual measurement.

As the velocity at the outlet was found to be low (less than 1 m/s) and highly nonuniform, it has been decided to prepare a channel with extension of a smaller cross-section. Hence, the outlet channel had a trapezoidal constriction and a straight rectangular part. The cross-sectional area of the extension is reduced four times compared to the outlet of the condensation hood itself. Despite this effort, the velocity profile at the air outlet (II) was still nonuniform. Therefore, velocity measurements have been conducted using Pitot tube (P-d) at 25 points throughout the cross-section according to log-Chebyshev method described in [3] (used during traversing a duct to determine the average air velocity) and the average value has been compared to the readings from the stationary sensors mounted in the channel. The average velocity from log-Chebyshev method was close to the one measured by probe (P-c), which proved the non-uniform velocity profile did not affect the results in this case. The length of this channel was limited by the available height of the laboratory room. Figure 4.5 presents the location of point (II) with sensors (P-c) and (P-d) while figure 4.6 shows their actual placement inside the channel's cross-section (see Figure 4.5 point (c)).

The ambient pressure, temperature, and relative humidity were measured at point (I).

The condensation hood has been examined in three cases of interaction with:

Case A: A low-powered steam generator (3.4 kW): laboratory conditions.

Case B: A high-powered steam generator (27 kW): semi-laboratory conditions.

Case C: A combi-steamer: real work conditions.

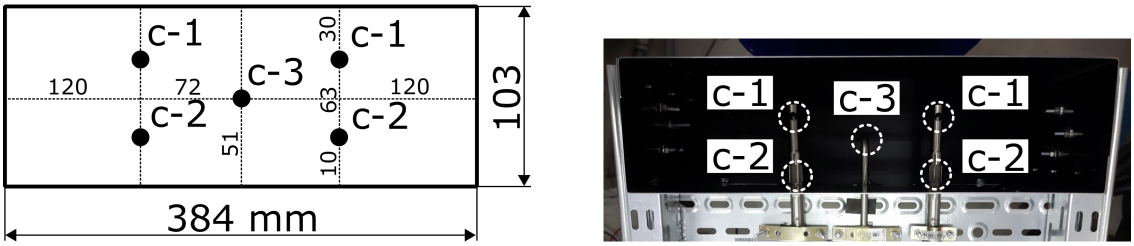

(a) (b)

Figure 4.6: Outlet channel's cross-section with location of measurement points. a) scheme; b) actual channel. c-1: t, v; c-2: ϕ; c-3: ΔP; t - temperature; v - velocity; ϕ - relative humidity; ΔP - velocity (photo: M. Tokarski).

Preliminary measurements showed that the flow rate of the condensate is not sufficient to satisfy the energy balance (eq.(4.7)). To facilitate condensate gathering and to prevent condensate accumulation inside the device, a dedicated scaffolding presented in Figure 4.7 was prepared. The CH was placed on the scaffolding, which was mounted on the CS. The scaffolding increased the existing slope (left-hand side view) and added an additional slope (right-hand side view) towards the condensate exit.

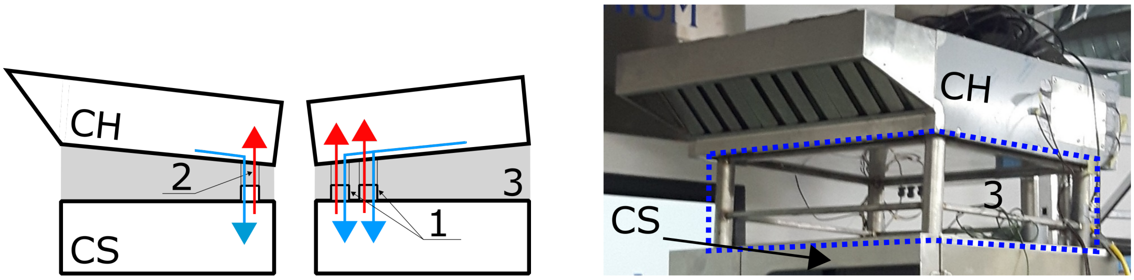

(a) (b)

Figure 4.7: Condensation hood's position relative to the combi-steamer with scaffolding: a) scheme; b) actual state. Left-hand side - side view, right-hand side - rear view; CH - condensation hood; CS - combi steamer; 1 - CS steam outlets; 2 - fittings; 3 - scaffolding. Red arrows - steam; blue arrows - condensate.

Due to the increased distance between the devices, the use of an additional duct (fitting) connecting CH and CS or steam generator became necessary. The duct branched into two transparent pipes (see figure 4.8, element 2) converging in the upper part. This enabled easy CH supply with steam and easy gravitational condensate gathering, as indicates Figure 4.8. Steam generators (*case A* and *case B*) are schematically presented in Figure 4.8. Both of them consist of a water tank a and an electric immersion heater c. The condensation hood CH is placed on the scaffolding (not shown in this figure) that provides global slope towards the bowl d where the condensate is gathered. The CH is connected with the water tank a by the fitting 2. Low-powered steam generator was additionally equipped with hot water supply valve b to extend the measurement time.

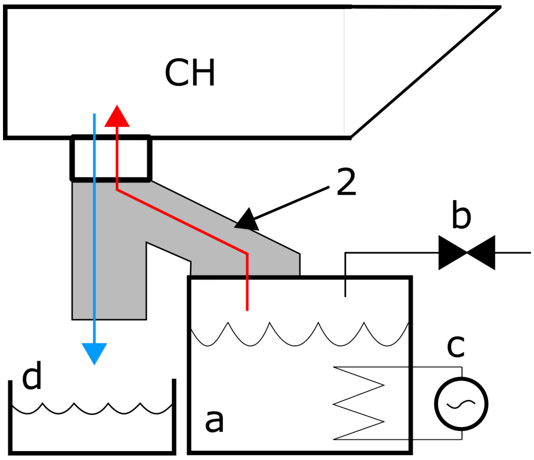

Figure 4.8: Scheme of the steam generators: CH - condensation-hood; a - water tank (or combi-steamer); b - water supply valve; c - electric immersion heater; d - the duct; e - condensate container; 2 - fittings; blue arrow - condensate; red arrow - steam.

Low-powered steam generator (case A) provided known and constant over time mass flow rate of the steam delivered to the condensation hood. Steam flow rate was determined twofold: based on the mass of the evaporated water in the specified period of time and from power of the heater. This allowed for determination of the expected condensate flow rate and for comparison with the actually measured one.

The steam generators were used to simulate known input into the condensation hood. The mass flow of steam was selected in a typical operating range of the CH in case A. It was used in mass and energy balance validation due to the small laboratory scale and controlled working conditions.

Second experiment (case B) was conducted to assess the maximum condensation capacity of the device. Here, the amount of generated steam greatly exceeded typical conditions. Due to technological and design limitations, the measurement time was also limited to about 20 minutes. This, however, allowed to achieve semi-steady state, that combined with known and precisely controlled steam input to the CH, was of great importance in defining the actual maximum condensation capabilities of the examined device.

The same scheme (Figure 4.8) also applies to the combi-steamer (case C). However, the heater power (c) along with the water supply (b) flow rate are unknown in this case, but in cases A and B is precisely measured.

The steam generators produced pure steam, so steam enthalpy could be calculated according to Eq.(4.9). Actual steam flow rate was determined based on the heater power (case A and B).

The combi-steamer supplies the condensation hood with a mixture of steam and air that makes any reliable and non-invasive measurement of the flow rate at point IV practically impossible. At the steam inlets, only temperature was measured with the use of thermocouples marked in Figure 4.5. Deriving the actual steam flow rate on the basis of evaporated water or heater power was also nearly impossible in this case, because the mass of evaporated water and the actual CS power output were unknown and difficult to assess. It has to do with CS transient and periodic work due to advanced automation, the details of which are also unknown. To better understand what kind of transient work is discussed here, in Figure 4.9 measured temperatures in both steam vents are presented. It should be noted that the temperature in both vents oscillated: in vent #1 mainly around 80-100°C with occasional drop downs to 65°C, while in vent #2 the oscillation was at 55-100°C during whole experiment. In Figure 4.9.b those oscillations are showed in detail and some consistent periodicity can be noticed. Each peak approaching 100°C means large portion of the steam produced periodically, probably as a result of the internal steam generator switching on and off.

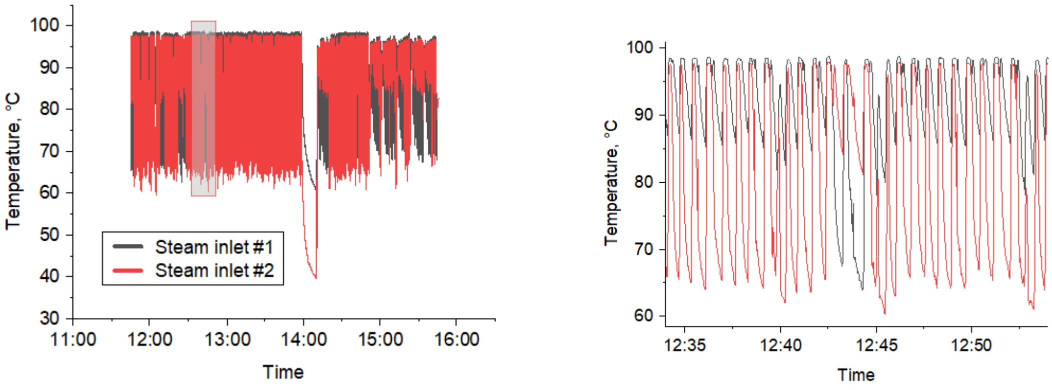

(a) (b)

Figure 4.9: Temperature in the CS steam vents: a) whole measurement; b) 20 minutes in detail. Case C2.

In Figure 4.9 temperatures in the steam inlets are presented. In other words: at the combi steamer outlet and condensation hood inlet. Temperatures inside the CH heat exchanger are also worth noting. For this reason, they are shown in Figure 4.10, that concerns the same measurement series. Black frame in Figure 4.10.a stands for a CS temporal shutdown and restart procedure - hence the global temperature rapid drop is clearly visible. Gray rectangle, however, denotes the time interval enlarged in Figure 4.10.b. Each temperature peak (five in total) stands for a 5 second CS door opening, during which a large portion of the steam escapes the working chamber and gets to the condensation hood, significantly impacting the heat transfer inside the HE.

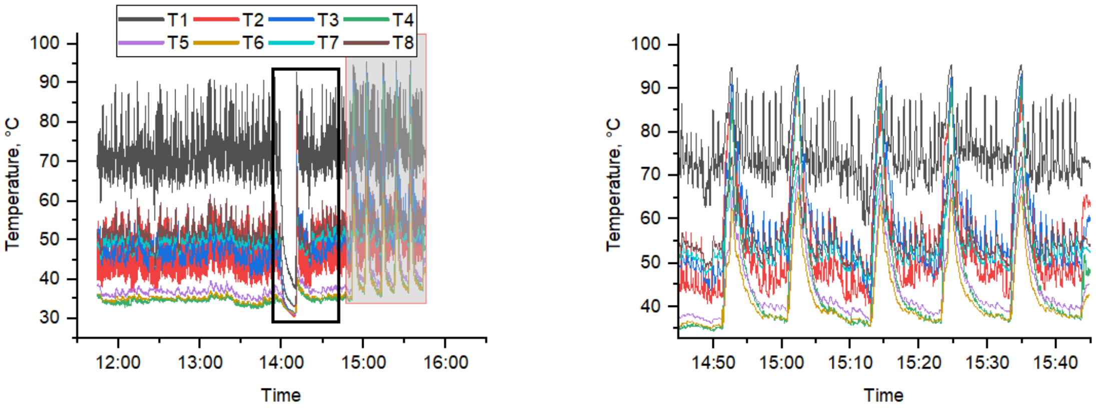

(a) (b)

Figure 4.10: Temperature in the CH's heat exchanger: T1-T4 - steam side thermocouples; T5-T8 - air side thermocouples. Black frame - CS shutdown; gray rectangle - five CS door openings.

Heat losses were the last element of the energy balance taken into account in the mathematical model - in figure 4.5 denoted as V. Only convection has been considered due to relatively low temperature of the condensation-hood's sheathing. As expected, obtained heat losses were negligible (less than 1% of the heater's power).

4.2.3 Measurement results

The measurements have been carried out in the three cases described in subsection 4.2.2. The are labeled with letters A, B and C. Numbers standing by the letters denotes for measurement series number (cases *A* and *B*) or operating mode (case *C*). Two additional cooking functions are connected with operating modes: *CT* - *Crisp&Tasty* - a parameter responsible for additional food drying; *HP* - *HumidityPro* - a parameter responsible for the additional humidity increase in the working chamber.

Full list of examined operating modes is as follows:

A1-2 - steam generator, *3.4* kW.

B1-2 - steam generator, *27* kW.

C1 - combi-steamer, convection mode, *150*°C, *CT1.*

C2 - combi-steamer, steam mode, *100*°C.

C3 - combi-steamer, convection mode, *250*°C, *CT1.*

C4 - combi-steamer, combi-steam mode, *250*°C, *HP3.*

C5 - combi-steamer, combi-steam mode, *250*°C, *HP5.*

Series C1 and C3 were investigated with *CT* parameter set to *1* out of *5* in order to minimize its impact on steam production. The higher *CT* is the less steam is produced. Whereas series *C4* and *C5* were examined with *HP* parameter set to *3* and *5* respectively in *5* grade scale. Medium and the highest available *HP* values have been used in experiments. All operating modes were set to their maximal temperature, so the condensation-hood could be examined in the most demanding conditions.

Selected measurement results for the steam generators are gathered in Table 4.1. Only the most important inlet and outlet parameters are included. Series A1** and A1 differs in steam mass flow rate. In the first case, $\dot{m}_{steam,IV}$ has been calculated on the basis of evaporated water mass. In the latter case steam flow rate results from the power of the heater. These two values are very similar, but the first one is burdened with higher uncertainty. Hence, in other series $\dot{m}_{steam,IV}$ is calculated using the heater power. The condensate flow rates were provided by energy and moisture balances.

Humidity at the outlet ϕ_{II} in all cases is low and varies from *21*% to *33*% despite the significant difference in obtained condensate. Such low values of relative humidity suggest that there is plenty of room for more moisture content before the air is saturated.

Table 4.2 contains some measurements of all three combi-steamer operating modes. The fan, in which the condensation hood is equipped, can operate on two gears: on the lower gear the measured mean air mass flow rate was at 0.19 kg/s, while on the higher gear 0.22 kg/s was achieved. Both values were very consistent throughout all measurements. Each of the CS operating modes has been examined on both fan gears.

Table 4.1: Steam generators - measurements.

Steam generator power:	3.4kW		27kW	
Symbol:	A1**	A1	B1	B2
t_I	24.9	24.9	32.8	26.0
ϕ_I	42	42	32	28
p_I*	98.71	98.71	100.23	100.23
t_{II}	38.3	38.3	65.3	63.0
ϕ_{II}	21	21	33	28
p_{II}	14	14	13	16
$\dot{m}_{steam,IV}$, g/s	1.38	1.36	11.49	11.50
$\dot{m}_{cond,III}$, g/s	1.25	1.25	2.91	4.15
Gear:	1	1	1	2

*ambient pressure, kPa

**steam mass flow rate $\dot{m}_{steam,IV}$ calculated from water gauge

Values of the condensate mass flow rate were measured and used in steam flow rate determination.

Table 4.2: Combi-steamer - measurements

Combi-steamer										
Symbol:	C1	C1	C2	C2	C3	C3	C4	C4	C5	C5
t_I, °C	25.4	26.5	26.1	27.2	26.4	25.5	26.4	27.0	27.0	25.5
ϕ_I, %	29	31	29	30	28	26	32	29	29	21
p_I*, kPa	100.23	100.77	99.94	99.84	100.72	100.23	100.23	100.23	100.07	100.08
t_{II}, °C	31.9	32.8	42.5	42.4	42.4	42.3	50.2	46.7	49.4	46.5
ϕ_{II}, %	21	22	14	14	14	13	12	14	10	9
$\dot{m}_{steam,IV}$**, g/s	0.23	0.19	0.73	0.71	0.83	1.06	1.27	1.56	0.96	1.11
$\dot{m}_{cond,III}$, g/s	0.18	0.15	0.53	0.54	0.60	0.74	0.73	0.97	0.81	0.73
Gear:	1	2	1	2	1	2	1	2	1	2

*reference pressure

**calculated on the basis of balances

4.2.4 Analysis outcome

Results of the measurements of the condensation hood in cooperation with steam generators are gathered in Table 4.3. Balances' inconsistency $\Delta\dot{H}$ were lower than 2.5%, so any further condensate compensation was not necessary. Additionally, the steam generator cases were used as a benchmark for further measurements and development of a mathematical model of the CH. The condensation efficiency (Eq.(4.12)) in cases A1 and A2 is about 90% whereas in cases B1 and B2 is significantly lower because of much higher steam flow rate (about 1.36 g/s in comparison to 11.50 g/s). It means the maximum power output of the heat exchanger was reached - approximately 6.5 kW for gear 1 and over 9 kW for gear 2. Additionally, especially in case B2, significant moisture increase ($\dot{m}_{v,I}$ in comparison to $\dot{m}_{v,II}$) in the air can be noticed. This means that the steam which was not condensed was diluted in the output air. However, the condensation hood during normal (casual) work will never have to cope with such heat loads as in case B2, which is confirmed in Table 4.5. Moisture balance inconsistency $\Delta\dot{m}_v$ in case A1 and A2 is below 2%, while in case B it is even smaller. Both cases indicated clearly that the balances are correct and can be used in further calculations.

Table 4.3: Steam generators - results.

Steam generators				
Symbol:	A1	A2	B1	B2
w_I*	0.0077	0.0084	0.0099	0.0059
$\dot{m}_{v,I}$, g/s	1.61	1.76	1.81	1.31
w_{II}*	0.0083	0.0091	0.0569	0.0475
$\dot{m}_{v,II}$, g/s	1.73	1.90	10.39	8.66
$\dot{m}_{steam,IV}$, g/s	1.36	1.36	11.49	11.50
$\dot{m}_{cond,III}$, g/s	1.21	1.25	2.91	4.15
$\dot{m}_{cond,III,ad}$, g/s	0.02	-0.02	0.00	0.00
$\Delta\dot{H}$, %	1.54	1.13	2.46	0.24
$\Delta\dot{m}_v$, %	1.75	-1.60	0.00	0.00
$\dot{Q}$, kW	2.8	2.8	6.5	9.3
η, %	89.3	91.6	25.3	36.1
Gear:	1	1	1	2

*mass of moisture per unit mass of dry air

The combi-steamer's output is not exactly known. Any measurements of mass flow rate are difficult and burdened with significant errors due to high temperature (at around 100°C) and high humidity. Pitot tubes were used, but any brief exposure to the combi-steamer's output resulted in the tube clogging with droplets which affected the measurement results. The situation with the humidity probe was similar. For this reason, any attempt to measure reliably the moisture content and total mass flow rate requires prior separation of moisture from the air. To do so, a dedicated device is necessary. Due to low gauge pressure (several Pa) the use of any additional device causes a relatively significant pressure drop. This is a serious problem when analyzing its work in an actual operating conditions (case C).

Mass and energy balances were positively validated with the use of the cases A and B (Table 4.3, where the balances were satisfactorily closed, the working conditions were under control, and the steam input to the CH was known. However, preliminary results from case C (Table 4.4) showed that only part of the energy balance is closed without any additional actions. The explanation was quite simple - part of the condensate from the CH dripped down the wall of the fittings back to the combi-steamer (CH-a route according to the Figure 4.8).

Those difficulties forced a specific approach used to compensate the balance equations. It required the reduction of the balance inconsistency by adjusting the mass flow rate of the condensate and of the steam. According to the Eq.(4.7), where enthalpies of air and heat losses ($\dot{H}_I$, $\dot{H}_{II}$ and $\dot{Q}_V$ respectively) are properly estimated and fixed by design considerations, the balance inconsistency depends on just two remaining elements - enthalpy of the steam and the condensate ($\dot{H}_{IV}$ and $\dot{H}_{III}$ respectively). Assuming that, both of them are correct except for the mass flow rates $\dot{m}_{condensate,III}$ (that is deficient) and resulting from that $\dot{m}_{steam,IV}$ (see Eq.(4.7)), it becomes justified to compensate the missing condensate by increase of $\dot{m}_{condensate,III}$ by $\dot{m}_{cond,III,ad}$.

To show the effect of the balance equations compensation approach, the final results for *case C* have been divided into two tables: Table 4.4 with selected results before and after balance compensation; Table 4.5 with the results after compensation only.

Table 4.4 contains two chosen measurement series before and after the balance equations compensation procedure described above. High energy balance inconsistency $\Delta\dot{H}$ (over ten percent) have been greatly reduced by simple condensate flow rate compensation (not captured condensate $\dot{m}_{cond,III,ad}$). Significant amount of the condensate was missing - approximately 70%. Moreover, missing condensate affects condensation efficiency (Eq.(4.12)) that increases from 83% in case C1 and from 76% in case C2 by over 10% to over 90% in both cases. While the missing condensate $\dot{m}_{cond,III,ad}$ is included in $\dot{m}_{cond,III}$, the steam flow $\dot{m}_{steam,IV}$ is affected as well. Because of that, the share of the condensed steam in the overall steam flow rate increases, which translates directly to the higher condensation efficiency.

Results after balance compensation (condensation hood in cooperation with the

Table 4.4: Chosen balances - compensation.

Combi-steamer				
Symbol:	C1*	C1**	C2*	C2**
w_I***	0.0067	0.0067	0.0068	0.0068
$\dot{m}_{v,I}$, g/s	1.49	1.49	1.49	1.49
w_{II}***	0.0068	0.0068	0.0075	0.0075
$\dot{m}_{v,II}$, g/s	1.52	1.52	1.66	1.66
$\dot{m}_{steam,IV}$, g/s	0.19	0.75	0.71	1.70
$\dot{m}_{cond,III}$, g/s	0.15	0.71	0.54	1.53
$\dot{m}_{cond,III,ad}$, g/s	0.00	0.56	0.00	0.99
$\Delta\dot{H}$, %	-11.33	0.03	-16.60	0.05
$\Delta\dot{m}_v$, %	0.00	0.00	0.00	0.00
$\dot{Q}$, kW	0.4	1.4	0.4	1.6
η, %	83.4	95.9	76.7	90.3
Gear:	2		2	

*results before balance compensation
**results after balance compensation
***mass of moisture per unit mass of dry air

Table 4.5: Combi-steamer - results.

Combi-steamer										
Symbol:	C1	C1	C2	C2	C3	C3	C4	C4	C5	C5
Gear:	1	2	1	2	1	2	1	2	1	2
w_I*	0.0059	0.0067	0.0062	0.0068	0.0059	0.0053	0.0068	0.0065	0.0065	0.0043
$\dot{m}_{v,I}$, g/s	1.12	1.49	1.17	1.49	1.11	1.17	1.28	1.43	1.22	0.97
w_{II}*	0.0061	0.0068	0.0073	0.0075	0.0071	0.0067	0.0097	0.0091	0.0074	0.0061
$\dot{m}_{v,II}$, g/s	1.16	1.52	1.37	1.66	1.34	1.49	1.82	2.02	1.37	1.35
$\dot{m}_{steam,IV}$, g/s	0.65	0.75	1.62	1.70	1.61	2.02	2.51	1.73	2.02	2.44
$\dot{m}_{cond,III}$, g/s	0.60	0.71	1.42	1.53	1.38	1.70	2.01	1.76	1.87	2.06
$\dot{m}_{cond,III,ad}$, g/s	0.42	0.56	0.89	0.99	0.78	0.96	1.28	0.96	1.06	1.33
$\Delta\dot{H}$, %	0.08	0.03	-0.05	0.05	-0.07	-0.01	-0.07	-0.11	0.02	0.01
$\Delta\dot{m}_v$, %	0.00	0.00	0.00	0.00	0.00	0.00	0.00	0.00	0.00	0.00
$\dot{Q}$, kW	1.4	1.6	3.2	3.5	3.1	3.8	4.5	4.0	4.2	4.6
η, %	93.2	95.3	87.7	90.3	86.0	84.2	78.9	75.0	92.4	84.4

*mass of moisture per unit mass of dry air combi-steamer) are shown in Table 4.5. All balances' inconsistencies are negligible - less than 1%. Steam flow rates differ from 0.65 g/s for case C1 to 2.51 g/s and 2.44 g/s for cases C4 and C5. Compensating condensate flow rates $\dot{m}_{cond,III,ad}$ vary depending on case: from barely 0.17 g/s in case C4 gear 2 to even 1.28 g/s in the same case but with gear 1. Case C5 gear 2 turned out to be the only one with higher additional condensate - 1.33 g/s. Compensating condensate (the missing condensate) constitutes a significant part of the overall condensate that allows for closing the energy balance and, approximately, equals to 59%. In other words - during measurements with the combi-steamer about 2/3 of the condensate was not captured. With use of the fittings we proved that some amount of the condensate dripped down back to the combi-steamer instead of the condensate container according to figure 4.8. This was a surprise, because the shape of the fittings should prevent this from happening. Condensation efficiency, again, is related to the steam and condensate flow rates. Cases C1 and C2 are characterized by the highest efficiency (for about 90%), whereas remaining cases have noticeably lower efficiency. Cases C4 and C5 are surprising due to obtained results. In both cases, condensation efficiencies are slightly lower for gear 2. Moreover, steam flows as well as condensation flows are not consistent. This is difficult to explain, especially since experiments with the steam generator carried out in similar manner produced more accurate results. However, it can be explained, at least in part, by the combi-steamer, its complexity, and difficult to determine way of work. In addition to that, measurement errors could contribute to this.

4.2.5 Measurements' summary

In this thesis, numerous measurements of the condensation hood have been carried out in different conditions. At first, the condensation hood operating with the steam generator (3.4 kW) was investigated in conditions similar to its normal working conditions (about 1.4 g/s of steam). Then, extreme case has been taken into account to achieve maximum heat power of the device - 27 kW steam generator - with the use of both fan gears. Obtained in this case steam flow rate supplying the condensation-hood amounts to 11.5 g/s. Steam flow rate was derived from the electric heater power and enthalpy of evaporation.

In the next step, cooperation with a dedicated combi-steamer was tested and all available oven's operating modes have been investigated with both available fan gears. However, the steam flow rate was not possible to be measured reliably due to the high moisture content affecting the available measurement instruments, high pressure drop sensitiveness of the oven, and semi-stationary work of the heater. The condensate flow rate turned out to be difficult to catch as well. Use of fittings did not meet the expectations and still a significant part of the condensate flowed back to the oven. To overcome this problem, the steam and condensate flow rates were identically modified - some steam/condensate was added to close the energy balance. This balance was included in the mathematical model of the condensation hood developed to assess the performed measurements and to carry out a preliminary diagnosis.

This model consists of three balances: air, moisture, and energy. Obtained energy balances' inconsistencies were high (over 10%) and needed to be compensated. Unfortunately, due to the lack of reliable information concerning steam and condensate flow rates (number of unknowns higher than the number of equations), the application of widely known standard data reconciliation methods was not possible. Thus, the mathematical model was used to determine the missing condensate and/or steam flow.

This approach affected the results of the steam and condensate flow rates, condensation efficiency, heat power of the heat exchanger, and balance inconsistencies. Obtained values of the steam flow vary depending on the oven's operating mode from 0.65 g/s for case C1 to 2.55 for case C4. Not much less demanding was case C5, which differs from C4 only in the operating parameter *HP* value.

Condensate flow rate differs in a similar way. In case C1 (where steam flow was the lowest) obtained condensate flow rate is the lowest as well and equals to 0.71 g/s. Whereas the highest condensate flow rate of 2.06 g/s was obtained in case C5.

Steam generators (case A and case B) were used as a benchmark in refining the measurement methodology and developing the mathematical model. Results were very satisfactory. Balances' inconsistencies did not exceed3% so any further condensate compensation was not necessary. In case of the combi-steamer (case C), however, all energy balance inconsistencies were much higher (from approximately 10% to over 25%). After the compensation, the differences decreased and eventually they do not exceed 1%.

Heat power of the heat exchanger (resulting directly from condensed steam) varies from 1.34 kW in case C1 gear 1 through 4.64 (case C5 gear 2) to 9.34 kW in case B2.

Calculations show that the highest condensation efficiency of almost 96% was reached in less heat-demanding case C2, while the lowest efficiency (75%) has been obtained in one of the most demanding cases - case C4. In separate case B1 efficiency decreased to 25%, but it was an extreme case just to investigate the condensation hood's performance under the most unfavorable conditions (maximum steam input, lowest fan gear 1).

The experiments proved that the steam channel 5 shown in Figure 4.2 and in Figure 3.2, is not sufficiently wide, therefore majority of the steam stays in bundle 4-left. This leads directly to the situation, where the pipes of bundle 4-left are heavily loaded while the pipes of bundle 4-right are hardly loaded. Hence, potential of the heat exchanger is not fully used.

The condensation efficiency of the condensation hood is very high and it can be concluded that the device performs well. However, the detailed analysis of this device is not possible through an analytical model only. Thus, the numerical model needs to be developed. The numerical study of the considered device is a subject of further study.

The results prove that the approach presented in this work was justified and gave reasonable values. It also allowed to assess quality of the measurements in terms of measured quantities. Thus, the obtained results can be used in the next step - validation of a numerical model described further.

4.3 Numerical model

The condensation hood is an asymmetric and complex construction. Both steam inlets are located on one side of the device (element II-6 in Figure 4.13). Hence, the whole geometry of the device needs to be simulated.

The computational domain has been divided into three main parts shown in Figure 4.11: inlet part (I) (orange), heat exchanger steam side (II) (blue) and heat exchanger air side (III) (green). Such approach allowed to build three independent sub-models with three independent meshes according to the different needs. All these three parts/sub-models were coupled by UDFs and appropriate boundary conditions. Part (I) consists of front baffles, grease filters, and fan boundary conditions. Part (II) is an inter-pipe space where steam condenses, while part (III) is just air outlet zone with outlet filter. There was an attempt to model only parts (II) and (III) but due to the connection between parts (I) and (III) (see I-L and I-P Figure 4.13) the model was unstable.

The front baffles and the grease filters in part (I) were modelled as a porous zone.

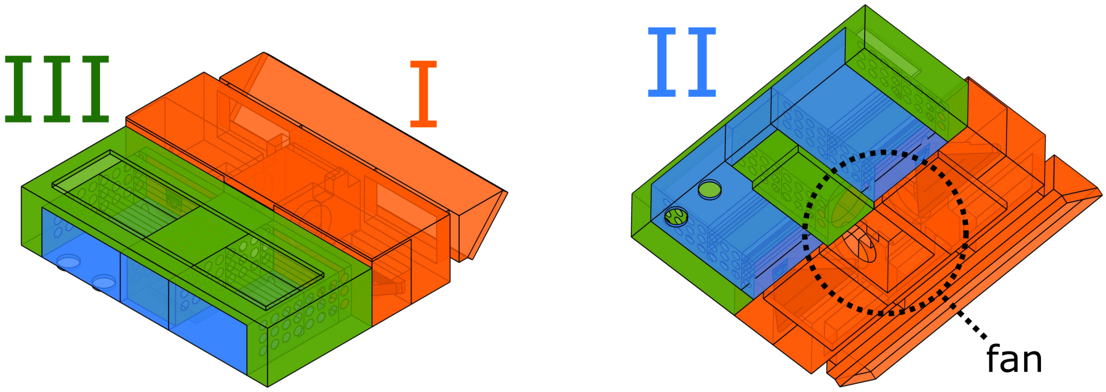

(a) (b)

Figure 4.11: Geometry: a) top view; b) - bottom view. I - inlet part; II - heat exchanger (steam side); III - heat exchanger (air side).

Actual pressure drops have been provided by additional measurements. Proportionality coefficient was evaluated at 0.31 while inertial resistance factor C_2 was 12.15 and has been calculated according to the Ansys Fluent User's Guide [4]. The fan is a complex device to be modelled and as it is not crucial part of the model, it was decided to investigate its performance in the controlled conditions and replace it by a boundary conditions BC in the model. Geometry of the fan location is shown in Figure 4.11.b, while the BCs in Figure 4.12.a-b and e-f (BCs I-2 and II-3). This means that the geometries of the fan and its rotor are not included in the computational model.

The heat exchanger of the condensation hood, presented in Figure 4.12.c-f, was split in two parts: part (II) (steam side) and part (III) (air side). The heat exchanger is equipped with several dozens of internally finned pipes. Exact meshing of such geometry would need an enormous number of finite elements and an extremely long computing time. Additional numerical studies showed that around a million elements are necessary for accurate prediction of a pressure loss and a velocity profile inside the single pipe. For this reason, the pipe was analysed separately. Results from this analysis were used to develop an appropriate UDF, so the pipe geometry could be replaced by an empty cylinder with a set of boundary conditions accounting for the outflow from the pipe and its cooling performance. The BCs utilised by the pipe UDF are presented in Figure 4.12.c-f: II-WP denotes the pipe walls, II-4 and II-5 pipe inlets and outlets, respectively.

The most important assumption of this model is that the condensed steam (condensate) is removed from the domain instead of being modelled. Such an approach allows

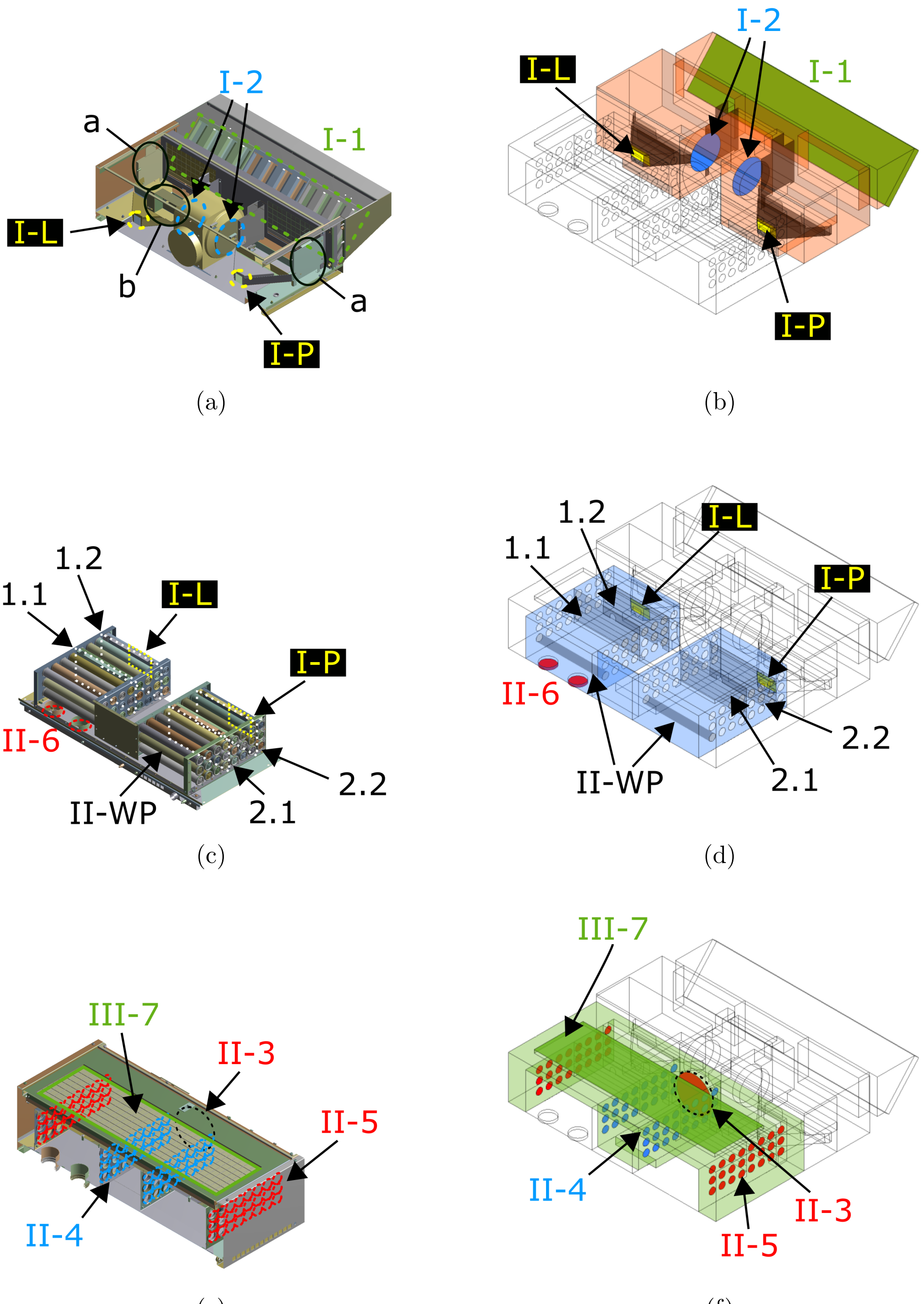

(a) (b)

(c) (d)

(e) (f)

Figure 4.12: Detailed division of the computational domain: a) original CH; b) model: part1; c) original CH; d) model: part 2; e) original CH; f) model: part 3. I-1 - air inlet; I-2 - fan inlets; II-3 - fan outlet; II-4 - pipe inlets; II-5 - pipe outlets; II-6 - steam inlets; III-7 - air outlet; II-WP - pipe walls; I-L & I-P - left hand side and right hand side aperture, respectively; a - peripheral handles; b - controller; 1.1 & 1.2 - left hand side baffles; 2.1 & 2.2 - right hand side baffles.

for use of a *species transport* model and greatly enhances calculation performance. The $k-\varepsilon$ model has been used for turbulence modelling, due to dominant air velocity at around 10 m/s in the inlet part (I) and outlet part (III). The steam flowing in the heat exchanger (II) slows down rapidly to less than 1 m/s which initially caused solution stability problems. However, once the *laminar zone* was set in the steam side of the heat exchanger (II), the stability problems have been resolved.

Outlet filter located in the part (III) has been also modelled as a porous zone. As in the case of front baffles and grease filters, additional measurements provided the actual pressure drop of this filter.

The above-mentioned sub-models together with the adapted boundary conditions are now described in the next subsections.

4.3.1 Boundary conditions

The boundary conditions used in the model are presented in Figure 4.13. They are numbered from (1) to (7). Roman numerals (I) to (III) denote the parts into which the computational domain has been divided, as shown in Figure 4.11. Number (I-1) stands for the air inlet with pressure inlet BC set, where no additional gauge pressure was set. Fan inlets (I-2) force the air flow by a negative pressure gauge of -48.7 Pa to satisfy the measured mass flow rate of air. UDF scaled velocity profile is used at fan outlet (II-3), then the air flows to pipe inlets (II-4), where the back pressure is set for each pipe individually with use of another UDF. This significantly affects air flow rates in the pipes. Next, air heated in the pipes leaves them through the pipe outlets (II-5), where mass flow rates from (II-4) and moisture content are transferred. Only temperature is applied different resulting from heat transfer realised via UDF at pipe's wall (II-WP). Steam is provided with steam inlets (II-6) (half of the steam mass flow rate per each inlet) as mass flow rate BC. The air is leaving the device through air outlet (III-7) (pressure outlet BC).

4.3.2 Model of the fan

The implemented model of the fan is based on fan inlets I-2.1 and I-2.2 and fan outlet II-3 previously shown in Figure 4.13 and presented again in Figure 4.14.a. Air mass flow rate $\dot{m}$ through the fan is constant, so the sum of flow rates of fan inlets has

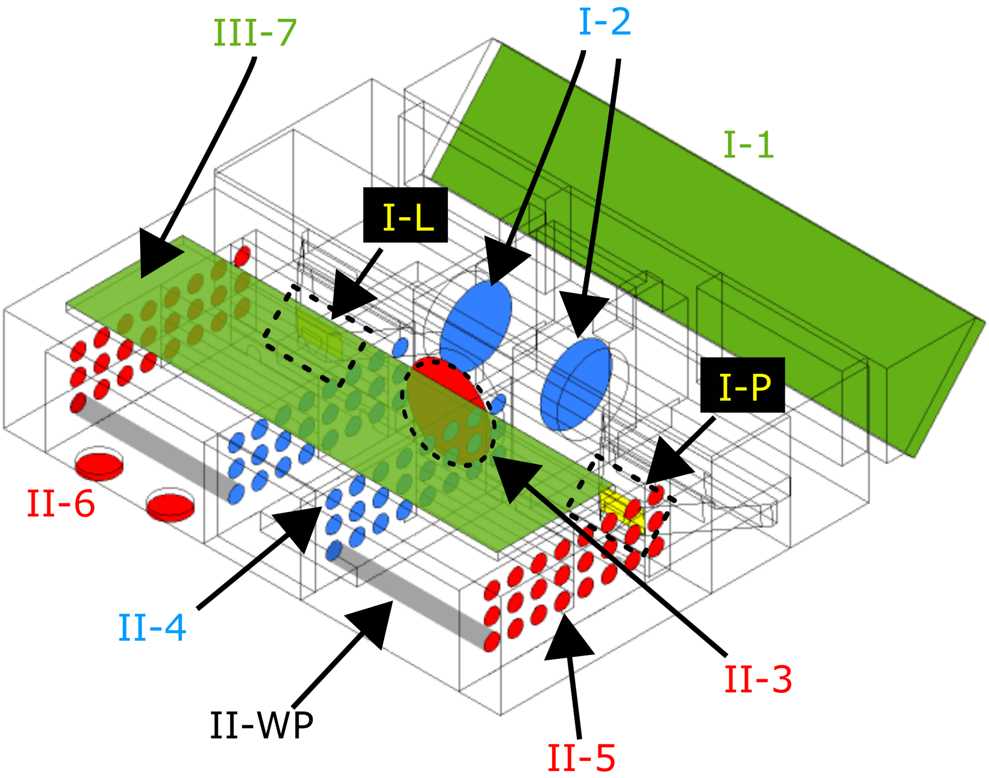

Figure 4.13: Boundary conditions. I-1 - air inlet; I-2 - fan inlets; II-3 - fan outlet; II-4 - pipe inlets; II-5 - pipe outlets; II-6 - steam inlets; III-7 - air outlet; II-WP - pipe walls; I-L & I-P - left hand side and right hand side aperture, respectively.

Table 4.6: OC numerical model - boundary conditions

	Function:	BC:
I-1	air inlet	pressure inlet
I-2	fan inlets	pressure outlets
II-3	fan outlet	velocity inlet
II-4	pipe inlets	pressure outlets
II-5	pipe outlets	mass flow rate inlets
II-6	steam inlets	mass flow rate inlets
III-7	air outlet	pressure outlets
II-WP	pipe wall	wall
I-L& I-P	apertures	interface

to be equal to the flow rate of the fan outlet

$$\dot{m}_{II-3} = \dot{m}_{I-2.1} + \dot{m}_{I-2.2} \tag{4.13}$$

where $\dot{m}_{II-3}$ stands for mass flow rate at fan outlet II-3, $\dot{m}_{I-2.1}$ and $\dot{m}_{I-2.2}$ are mass flow rates at fan inlets I-2.1 and I-2.2, respectively.

Temperature T and humidity w are also taken into account. Both of them result from balances written for the fan and then are applied to the fan outlet II-3. Fan energy balance takes the form

$$\dot{m}_{I-2.1}c_{I_{2}.1}T_{I-2.1} + \dot{m}_{I-2.2}c_{I-2.2}T_{I-2.2} = \dot{m}_{II-3}c_{II-3}T_{II-3} \tag{4.14}$$

where c denotes air specific heat, J/(kg K), T stands for air temperature, K. Air temperature increase due to fan's work is negligible, so temperature at the fan outlet is the same as at the fan inlet.

Fan moisture balance is as follows

$$\dot{m}_{I-2.1}w_{I-2.1} + \dot{m}_{I-2.2}w_{I-2.2} = \dot{m}_{II-3}w_{II-3} \tag{4.15}$$

where w stands for humidity ratio,(kg of moisture)/(kg of dry air).

Black box denotes the simplified fan shell which in the computational domain is an empty space. Blue thick lines at both sides stand for the fan inlets and the red one for the fan outlet - all presented as blue and red circles in Figure 4.13 respectively with numbers (I-2) and (II-3). Green arrows (Figure 4.14) indicate the air mass flow rate direction from the air inlet (I-1) shown in Figure 4.13 as green rectangle.

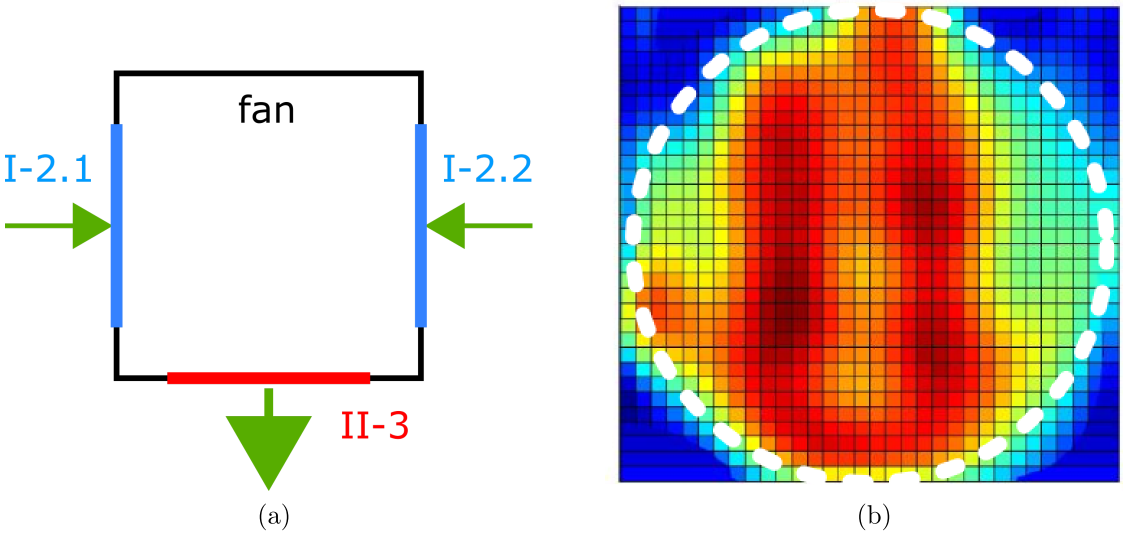

(a) (b)

Figure 4.14: Fan boundary conditions: a) general diagram; b) velocity profile at II-3 BC.

While the assumption of uniform profiles of temperature and humidity has no significant impact on the fan output, the velocity profile has. Hence, the fan UDF applies a proper velocity profile with the use of normal velocity vectors attached to the face (that belongs to the fan outlet (II-3)) of each cell adjacent to the fan outlet (II-3). Additional measurements of the installed fan in the condensation hood provided the necessary velocity values that were bilinearly interpolated with the use of a self-prepared algorithm in MATLAB to match the numerical mesh of the BC. Final velocity profile after interpolation is presented in Figure 4.14.b. White dashed circle stands for the fan outlet boundary edge. Complete fan UDF can be found in Appendix C.

4.3.3 Pipe and condensation model

Model of the pipes in the heat exchanger is schematically presented in Figure 4.15. Air flows from the air distribution chamber (III.A), through the pipe D (geometry of the pipe is reduced to the empty space accompanied by a set of BCs) to the air collector (III.B). The air flowing from the (III.A) flows into the pipe through the air inlet (II-4), where the pressure outlet BC is applied and the back pressure is set (as the pressure outlet, because the air leaves the computational domain via outlet of the pipe open to empty space). The back pressure is set in (II.4) BC is applied by the UDF individually for each pipe, and it results from the air mass flow rate of this pipe. The mass flow rate results also from the back pressure, so there are two quantities having impact on each other. Hence, the model at the very beginning of the simulation needs to stabilise the flow in the HE. Next, the air flow rate is translated to the air outlet (II-5) as the mass flow rate BC, as indicates the green arrow inside the pipe. According to the red arrows, the steam II-6 flows through the steam space (II) perpendicularly to the pipe.

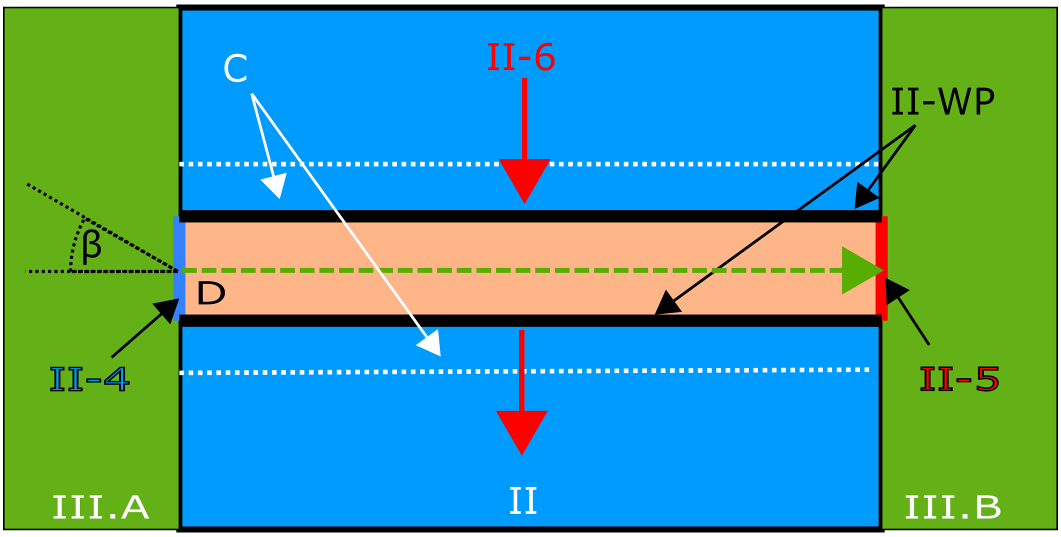

Figure 4.15: Pipe UDF - scheme. II-4 - air inlet; II-5 - air outlet; II-6 - steam; III.A - HE air distribution chamber; III.B - HE air outlet peripheral pocket; II - HE steam zone (part II); C - condensation cell layer; D - the pipe; II-WP - pipe wall.

Moisture content or humidity ratio (mass of moisture per unit mass of dry air) of the air flowing through the heat exchanger is constant. Hence, the moisture content at the pipe inlet (II-4) is transferred to the pipe outlet (II-5). Air mass flow rate through the pipe is also constant. Relative humidity, however, decreases because of the air temperature, which increases according to the heat received from the steam. This heat rate is calculated as follows

$$\dot{Q} = \dot{Q}_{max} w_{H_2O} \epsilon_t \epsilon_s \tag{4.16}$$

where $\dot{Q}$ stands for actual heat rate exchanged between the air and the steam, in W, $\dot{Q}_{max}$ is maximum possible heat rate to be exchanged by single pipe, in W, w_{H_2O} is steam mass fraction in the layer C (see Figure 4.15) next to pipe - which is able to condensate, ϵ_t and ϵ_s are the correction factors of the air and steam, respectively, regarding temperature. Both are provided by the external model of the single pipe. While the temperature of the air in the condensation hood is equal to the nominal air temperature in the external single-pipe model, the coefficient $\epsilon_t = 1$. If the temperature is higher, $\epsilon_t > 1$ and if lower then $\epsilon_t < 1$. The same applies to the ϵ_s.

The potential maximum heat rate of the pipe $\dot{Q}_{max}$ has been derived with the use of an external model of a single pipe. It takes the form of a polynomial in terms of air flow rate under the assumption that the pipe is entirely surrounded by pure steam. The model has been solved in a number of cases at different air flow rates, air inlet angles β, air and steam temperatures.

The pipe's adjacent layer C consists of a single layer of cells located at the pipe's wall II-WP with wall BC applied. Those cells contain some amount of steam that is less than or equal to their volume. Such approach limits the steam condensation potential and as a result the pipe's heat power. Condensation in this case occurs in layer C using two types of source terms. The first one is the mass source term, that is, in fact, the mass flow of the condensing steam (condensate) defined as follows

$$\dot{m}_{condensate} = -\frac{\dot{Q}}{h^*_{fg} V} \tag{4.17}$$

where $\dot{m}_{condensate}$ stands for volumetric condensate mass flow rate, kg/(s m^3), h^*_{fg} is a modified latent heat of vaporization of water, J/kg, and V is a volume (volume of the layer C showed in Figure 4.14) to which the source is applied, m^3. MOdified latent heat h^*_{fg} takes into account the condensate subcooling (i.e., an additional term consisting of the condensate enthalpy and temperature decrease beneath the saturation temperature).

The latter source term is an energy source term related to the removed condensate (see Eq. 4.17). Fluent solves several equations including mass and energy. Applied source term to the mass equation forces the same term in the species mass fraction equation (depending on the species sequence in the mixture definition) and requires the introduction of a proper term to the energy equation expressed by

$$\dot{H}_{steam} = \dot{m}_{condensate} c_{steam} (T - T_{ref}) \tag{4.18}$$

where $\dot{H}_{steam}$ denotes steam enthalpy rate, kW, c_{steam} is a specific heat of the steam, J/(kg K), T and T_{ref} stand for steam temperature and reference temperature, respectively, K.

The energy removed from the condensing steam has to be transferred to air at the outlet of the pipe (II-5) and entering zone (III.B) (see Figure 4.15). Two source terms were introduced: an energy source term transferring the energy from the steam to the air (in air peripheral collector); a mass source term responsible for condensation near the pipe wall (II-WP) on the steam side (II).

The near-wall energy source term is defined as in the equation (4.19)

$$\dot{Q}_{wall} = \frac{\frac{A}{R}(T - T_{air})w_{H_2O}}{V} \tag{4.19}$$

where $\dot{Q}_{wall}$ denotes heat flow rate transferred from the steam to the air on the air-side (zones (III.A) and (III.B)) by shared walls of the HE shell, W/m^3, A is surface area of a wall, m^2, R stands for thermal resistance, $(m^2K)/W$, and T_{air} is air temperature, K. Air in zone (II) also transfers its energy to the air in zones (III.A) and (III.B). This heat rate has been estimated and added to $\dot{Q}_{wall}$.

Near-wall mass source term is related with $\dot{Q}_{wall}$ and is defined in the same way as in Eq.(4.17) and takes the form

$$\dot{m}_{condensate,wall} = \frac{\dot{Q}_{wall}}{h_{fg}} \tag{4.20}$$

where $\dot{m}_{condensate,wall}$ denotes near-wall condensate mass flow rate, kg/(s m^3).

Exemplary UDF of a single pipe can be found in Appendix B, while heat transfer functions and source terms are in Appendix A.

4.3.4 Mesh

Convergence and solution quality remain the most important factors that had to be satisfied by the mesh. Figure 4.16 shows the mesh in several cross-sections throughout the domain. In inlet part I (see Figure 4.11 no vital phenomena occur, so there are no need for fine mesh. However, for convergence purposes, this part was meshed with orthogonal elements using the sweep method to the maximum extent possible.

The finest mesh was used in the heat exchanger steam side II, where condensation occurs and source terms are applied. This part almost entirely was meshed with the

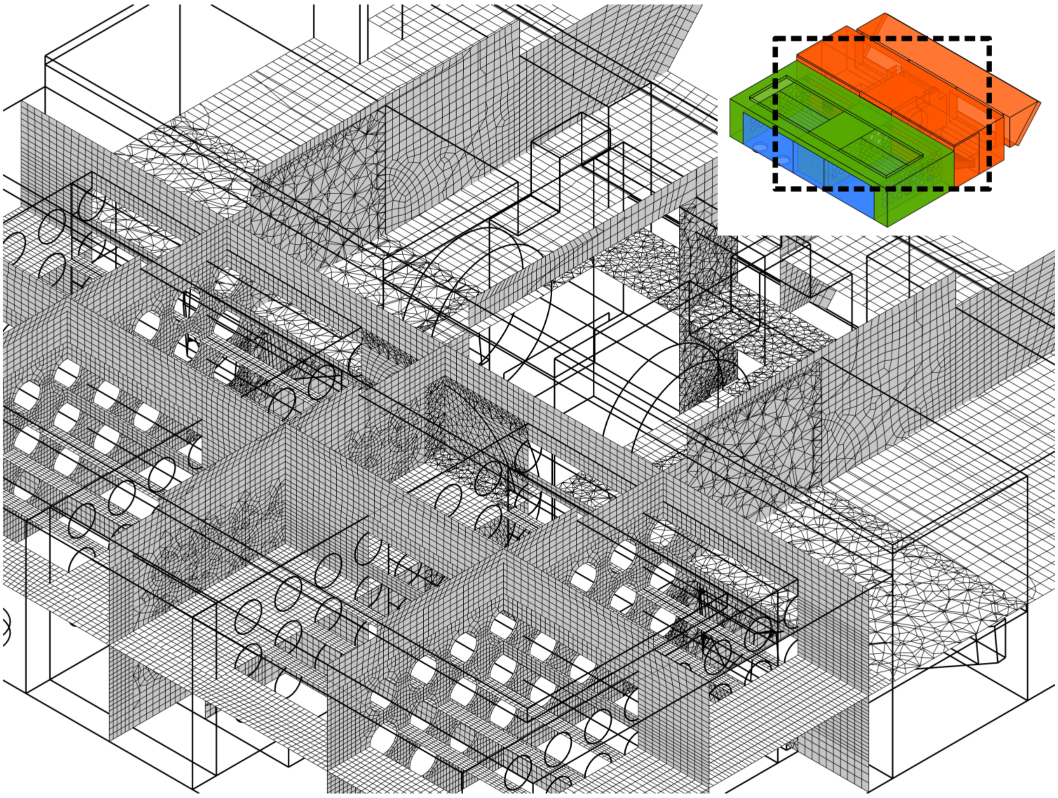

Figure 4.16: Mesh in cross-sections. Isometric view.

use of a sweep method with orthogonal elements of size up to 5 milimeters.

Heat exchanger air side (III) entirely consists of orthogonal elements (sweep method), that are slightly larger than in inter-pipe space of part (II).

In the case of unsweepable bodies, a tetrahedral mesh has been used.

The most important parameter for the condensation hood's evaluation is its capability for steam condensation, thus the condensate flow rate was taken into account and compared during mesh independence tests. The tests were carried out on the benchmark geometry to find the minimal necessary element size for a relatively stable condensate flow rate resulting from the pipe UDF. In Figure 4.17 results of the independence study are presented. In the figure, a plateau can be noticed, which starts from about 0.2 mln element mesh resulting in approximately 1E-7 m element size. Benchmark's geometry was limited, hence the minimal element size was taken into account during the final mesh preparation in the condensation zone. The final mesh consists of over 1.1 million elements and over 830 thousands nodes. As it was said, the maximum element size in part (II), where the condensation process occurs, was up to 5E-6 m, but elements in the inter-pipe space were kept below 1E-7 m just to stay at the plateau mentioned earlier.

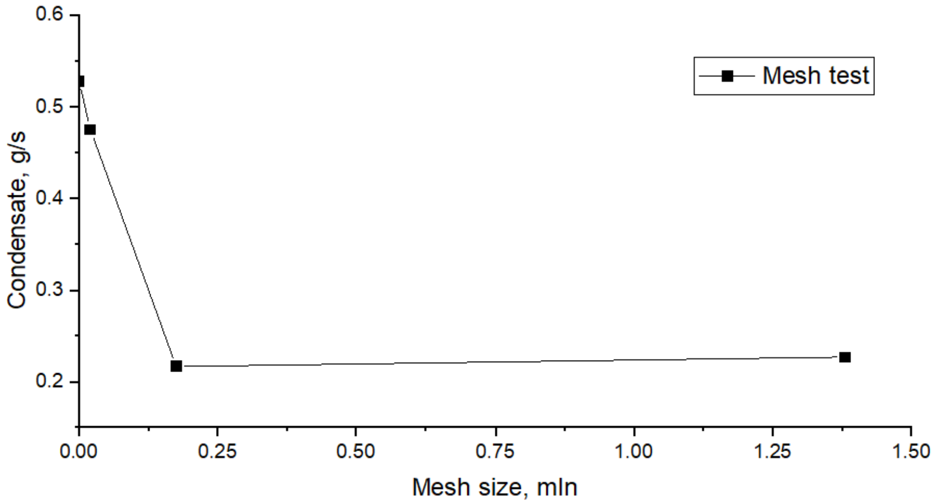

Figure 4.17: Mesh independence test.

4.4 Results and discussion

To present the numerical results, five cross sections throughout the computational domain were prepared, as shown in Figure 4.18. Plane H1 is the only horizontal one (at the height of the middle tube row). Planes V1-V3 vertically slice the middle of the fan inlet, left, and right hand side bundles, respectively. The last plane, V4, slices both bundles between the 4th and 5th pipe columns, perpendicularly to the planes V1-V3. The model was validated in all three cases described earlier (cases A, B, and C). For better clarity, results will be presented for all cases grouped by cross-sectional planes.

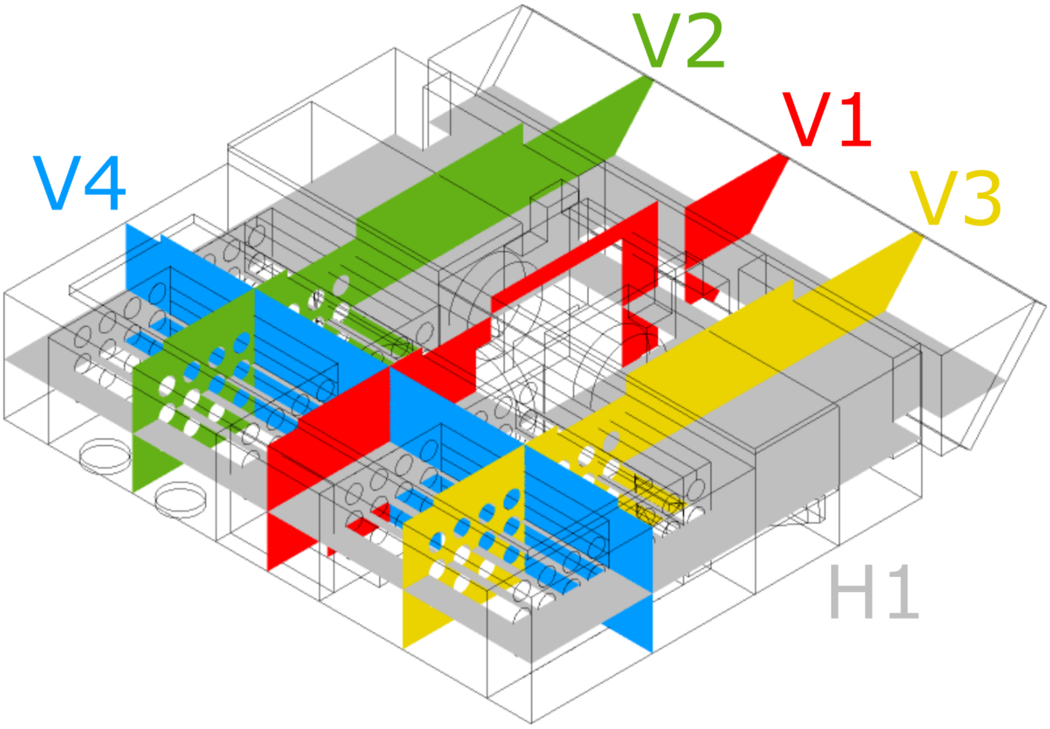

Figure 4.18: OC numerical model - cross sections: H1 - horizontal plane throughout middle pipe row; V1 - vertical plane at symmetry axis of fan inlet; V2 - vertical plane at the middle of left hand side bundle; V3 - vertical plane at the middle of right hand side bundle; V4 - vertical plane between 4th and 5th tube column.

General velocity field of the original CH model is presented in Figure 4.19. Figure 4.19.a shows velocity in case A, 4.19.b in case B, and 4.19.c in case C. The highest velocity is located in the air distribution chamber in the central part of the heat exchanger. Then, the medium velocity zone is located in the outlet part (III) (see Figure 4.11). In peripheral air pockets (III.B) air streams leaving the pipes can be distinguished. In the inlet part (I) velocity field is relatively uniform and symmetrical apart from the fan inlet surroundings. Velocity magnitude in the heat exchanger on the steam side II is unnoticeable except for the case B, where steam flow rate is almost 10 times greater than in the remaining cases.

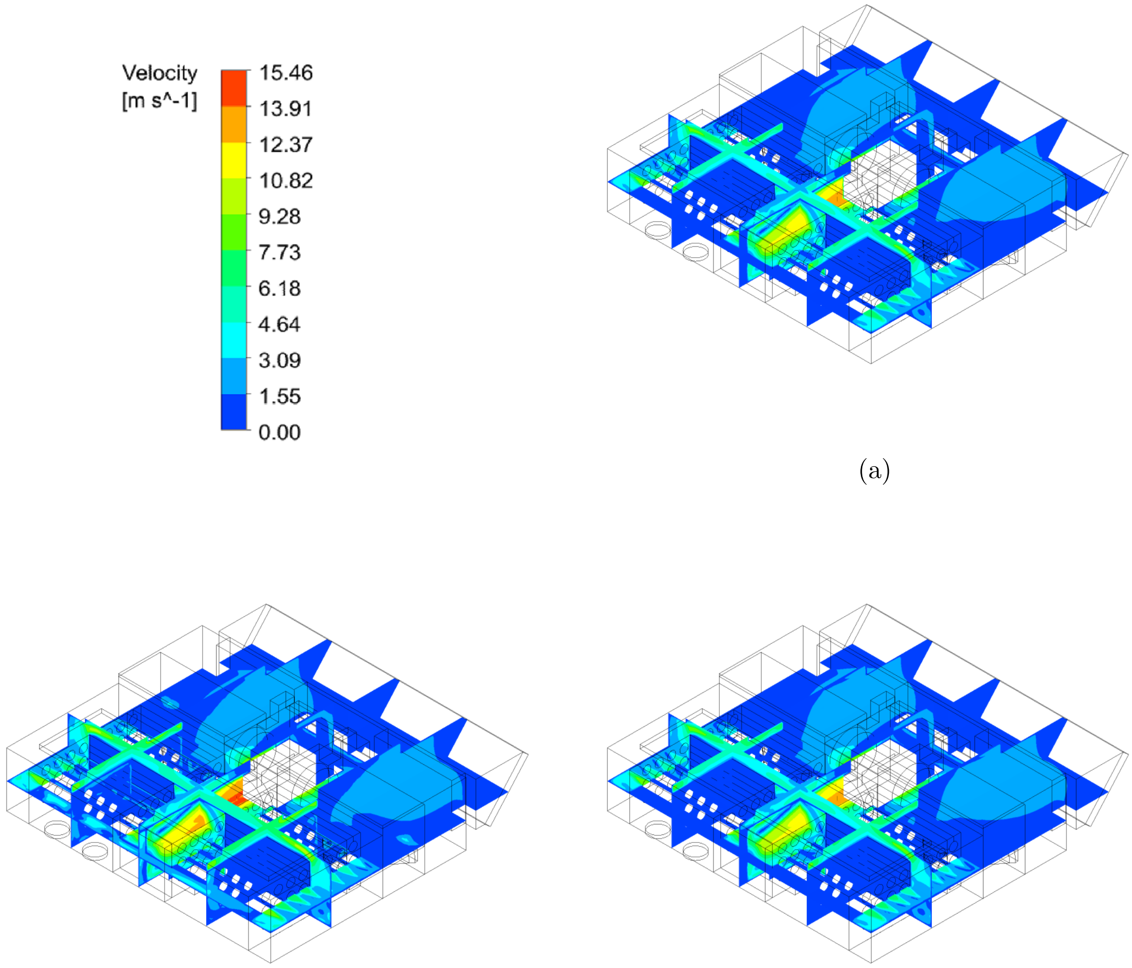

(a)

(b)

(c)

Figure 4.19: Velocity field: a) case A; b) case B; c) case C.

In Figure 4.20 velocity profile in V1 plane is presented. Figure 4.20.a additionally indicates the relevant boundary conditions consistent with Figure 4.13. Slightly higher velocity can be noticed in Figure 4.20.b referring to case B, where a higher air flow rate has been measured, thereby a higher flow rate was simulated. Besides, all three profiles look the same - low velocity on the fan side and high conical-like profile in the air distribution chamber with two near-wall recirculation streams at the top and the bottom of the chamber. Additionally, in Figure 4.20.b noticeably higher velocity is in the narrow channel that connects both bundles. The reason for that is the much higher steam flow rate.

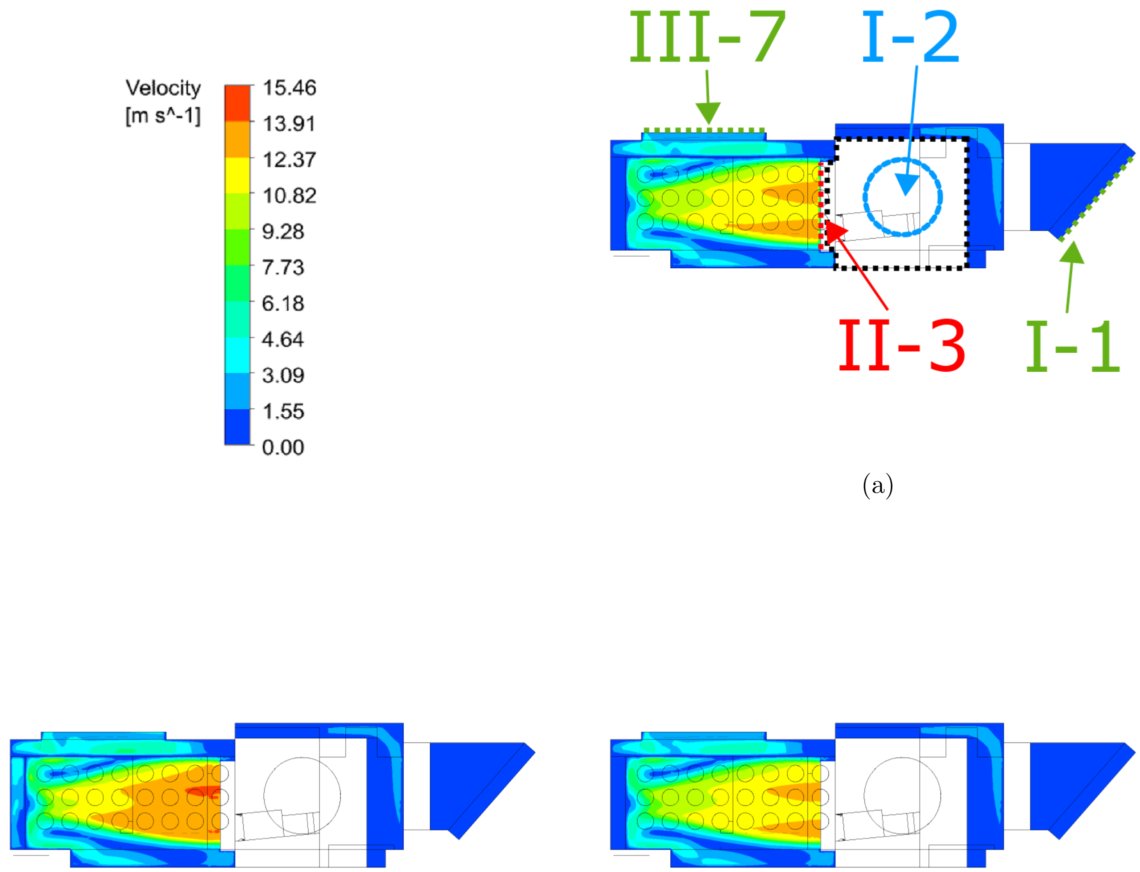

(a)

(b)

(c)

Figure 4.20: Velocity field in V1 plane: a) case A; b) case B; c) case C. I-1 - air inlet; I-2 - fan inlet; II-3 - fan outlet; III-7 - air outlet.

In Figure 4.21 velocity profiles in plane V2 are presented. In all three cases, velocity in the inter-pipe space is lower than 1.55 m/s. Small velocity increase can be noticed again, in case B (Figure 4.21.b) near the upper wall, middle baffle, and in labyrinth baffle in the fan chamber. This is consistent with the main steam streamline marked out in Figure 4.3.c. Velocity field in the fan chamber is similar and relatively uniform in all three cases. The highest velocity occurs in the HE outlet zone (part (III)) above the steam zone.

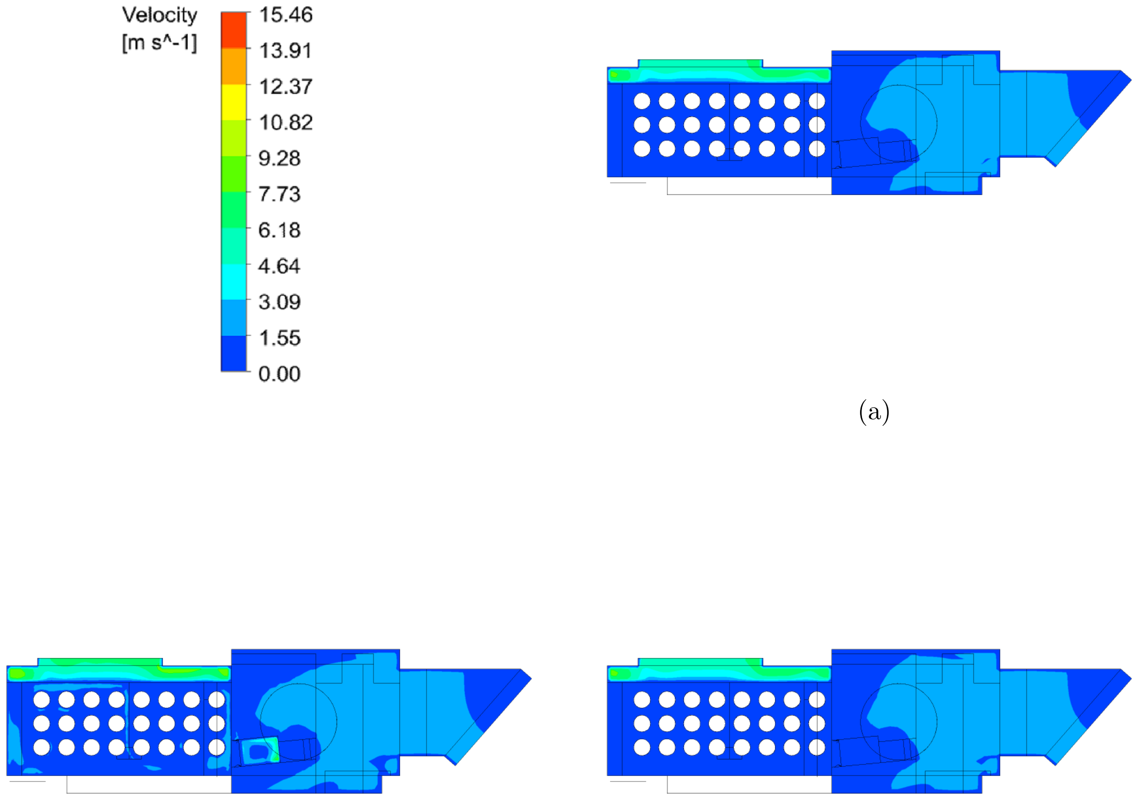

(a)

(b) (c)

Figure 4.21: Velocity field in V2 plane: a) case A; b) case B; c) case C.

Velocity field in plane V3 is shown in Figure 4.22. In all cases it looks like in plane V2, however, some minor differences can be observed in Figure 4.22.b addressing case B, as this plane crosses the tube bundle located further from the steam inlet. Hence, velocity in the inter-pipe space seems to be slightly lower, yet noticeably different from cases A and C.

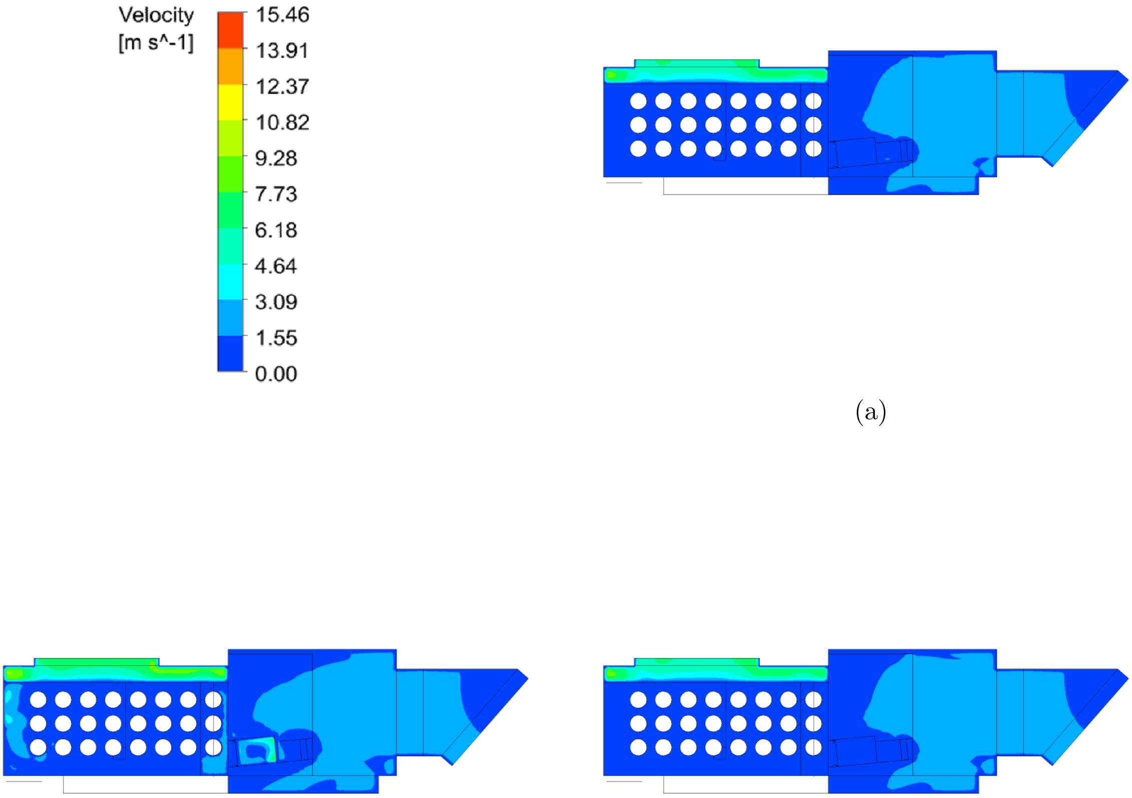

(a)

(b)

(c)

Figure 4.22: Velocity field in V3 plane: a) case A; b) case B; c) case C.

Plane V4 is located between 4th and 5th pipe column, which means it lies in the middle of the HE at the same location as baffles 1.1 and 2.1 (indicated in Figure 4.12.c and 4.12.d). In Figure 4.23 velocity field is presented in this plane. The highest velocity comes from the fan and can be observed in the central part of the cross section - in the air distribution chamber. Slightly lower velocities are in the peripheral air pockets where the air is leaving the tubes and above the heat exchanger in the region of air outlet. In all three cases the velocity profiles are similar, yet in case B (Figure 4.23.b) below the baffle 1.1 in the inter-pipe space velocity exceeding 1.55 m/s can be noticed due to the high steam flow rate.

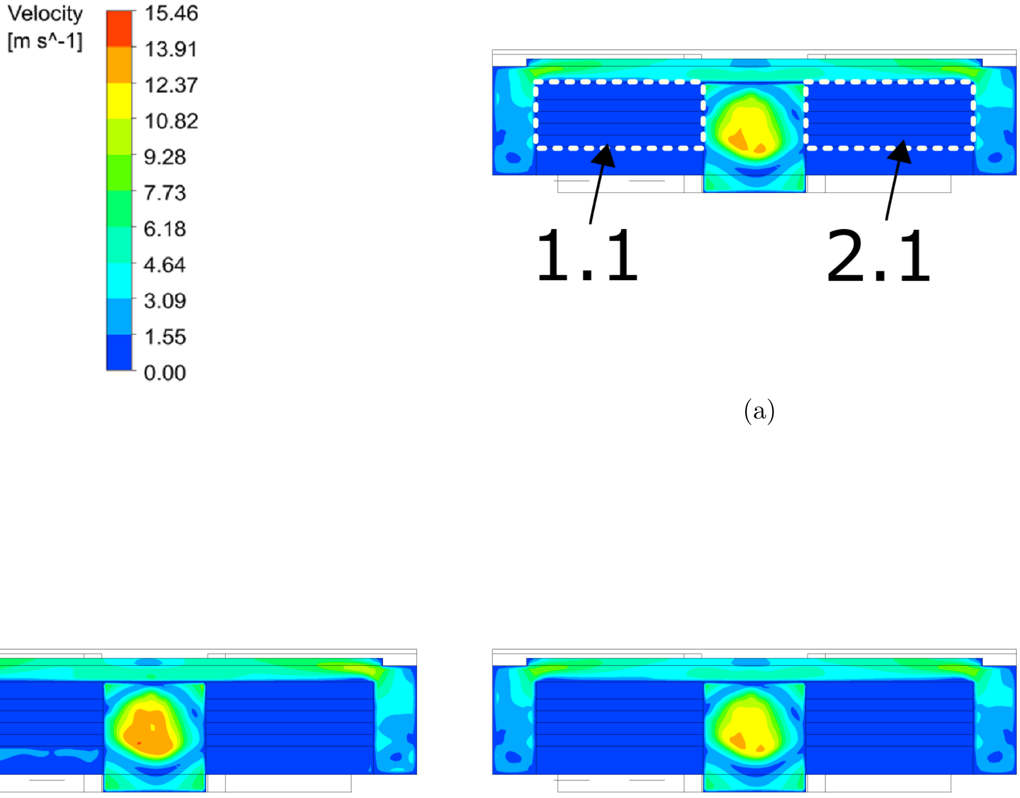

(a)

(b)

(c)

Figure 4.23: Velocity field in V4 plane: a) case A; b) case B; c) case C. 1.1 - left hand side baffle; 2.1 - right hand side baffle.

Velocity profiles of all numerically investigated cases are presented in the horizontal cross section H1 in Figure 4.24. This view provides some important information regarding the heat exchanger. Velocity profile of the fan is not symmetrical, hence significant velocity asymmetry in the air distribution chamber (2). This impacts the air distribution to the pipes - comparing left hand side peripheral pockets with right-hand side ones, it can be noticed that in the latter <1.55 m/s velocity regions (similar to dark blue stains) are slightly larger and more numerous which indicates that, the right hand side bundle is better supplied with air despite the fact it is worse supplied with the steam. Additionally, inside any single pocket (3), it is clear that the air flow rates in the pipes are larger in further pipes than in the pipes located closer to the fan.

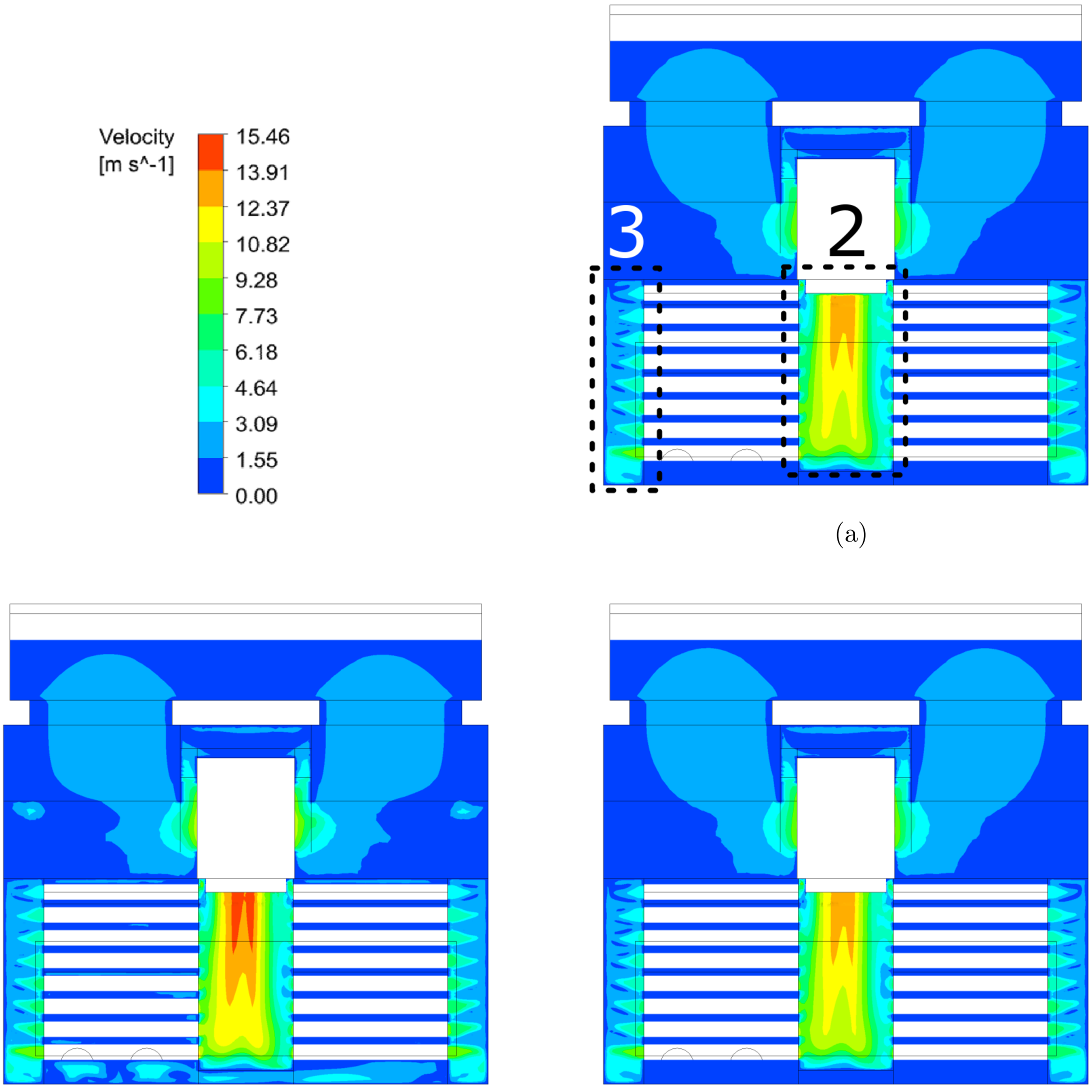

(a)

(b)

(c)

Figure 4.24: Velocity field in H1 plane: a) case A; b) case B; c) case C. 2 - air distribution chamber; 3 - peripheral air pocket.

In Figure 4.25 temperature distributions of the original CH are presented for all three cases used in validation. In all cases, the inlet zone (part (I)) practically does not participate in heat transfer. In the air distribution chamber, air is pulled by the fan from the inlet zone and has the lowest temperature in the HE. As the air leaves the pipes, it has significantly higher temperature due to heat transfer with the steam. The highest temperatures are located near the steam inlets in the left hand side bundle. In cases A and C the temperature gradually decreases as the steam flows through the bundles. Steam channel (5) (see Figure 3.2 and 4.2) has significant impact on the steam distribution in both bundles. In the Figure 4.25.a and 4.25.c left hand side bundle is noticeably hotter than the right hand side bundle. The situation is different in Figure 4.25.b, where case B is presented and a much higher steam flow rate is applied. In this case, both bundles are equally filled with steam, which confirms the temperature distribution. Additionally, in part (I) (inlet zone), a higher temperature near the apertures and labyrinth baffles can be observed, which implicates that not condensed steam got through the whole heat exchanger and mixed with the coolant air to be sucked by the fan a moment later.

Numerically obtained temperature distribution is presented in Figure 4.26. Uniform temperature close to the environment temperature (¡306 K) can be observed in the inlet zone and in the air distribution chamber in all cases. Temperature fields of cases A (Figure 4.26.a) and C (Figure 4.26.c) are almost identical. Slightly different is the temperature gradient in the channel that connects bundles - in Figure 4.26.b, where the channel is filled with steam uniformly. This is expected, as this case was the one at 27 kW. Air temperature at the outlet is also noticeably higher by ≈ 30 K.

Temperature fields are much more interesting in the V2 plane that crosses the left hand side bundle. Again, the temperature field of cases A (Figure 4.26.a) and C (Figure 4.26.c) will be discussed here together, because case C is based on the combi steamer measurements, while case A meant to recreate CH working conditions in cooperation with the CS but in controlled laboratory conditions. As both cases are characterised by similar set-up and, first of all, similar steam flow rates: 1.18 g/s in case A and 1.62 g/s in case C, temperature fields are similar with a slightly higher temperature in Figure 4.26.c. In both Figures (4.26.a and 4.26.c) a temperature stratification can be observed - the steam, as a lighter gas than air, tends to fill the upper part of the inter-pipe space while the air is sucked in to fill the lower part. First, baffle 1.1 constitutes a serious obstacle for the steam, which is forced to stay around tube columns 1-4 and to squeeze around the baffle in the direction of further pipes.

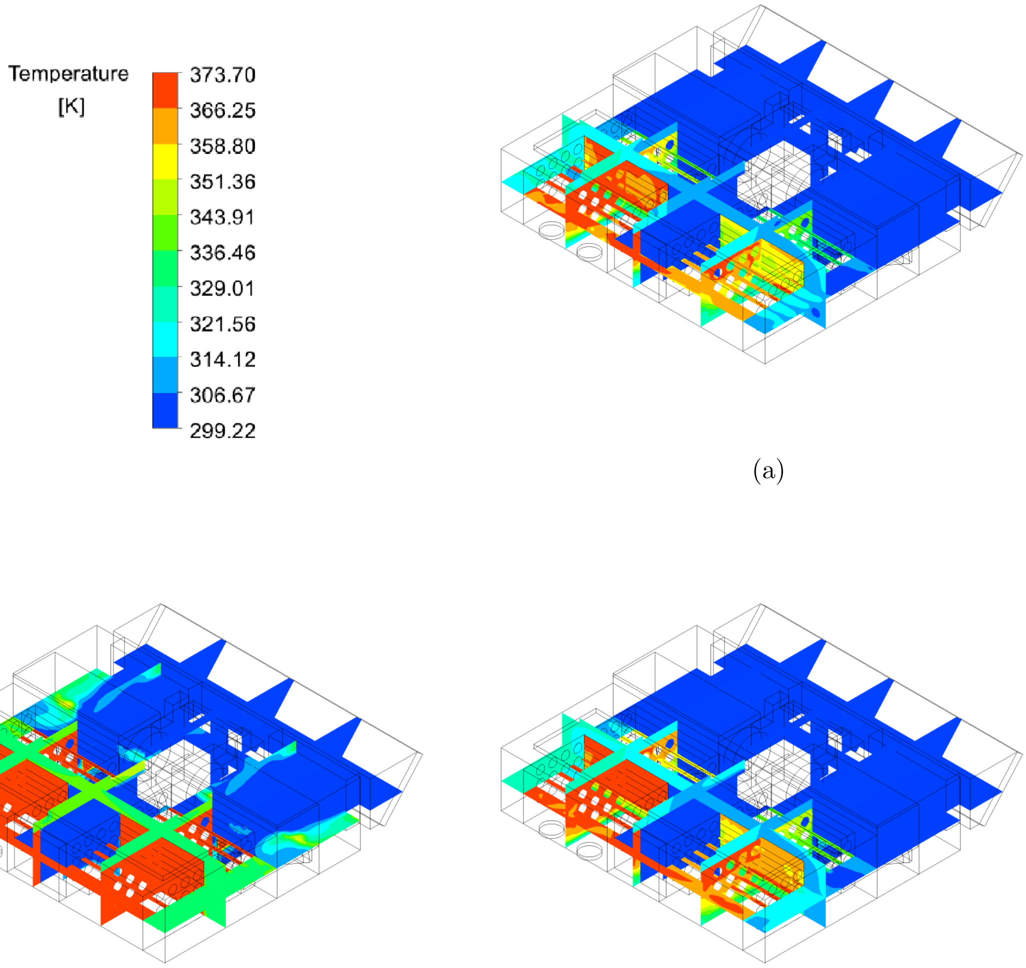

(a)

(b)

(c)

Figure 4.25: Temperature field: a) case A; b) case B; c) case C.

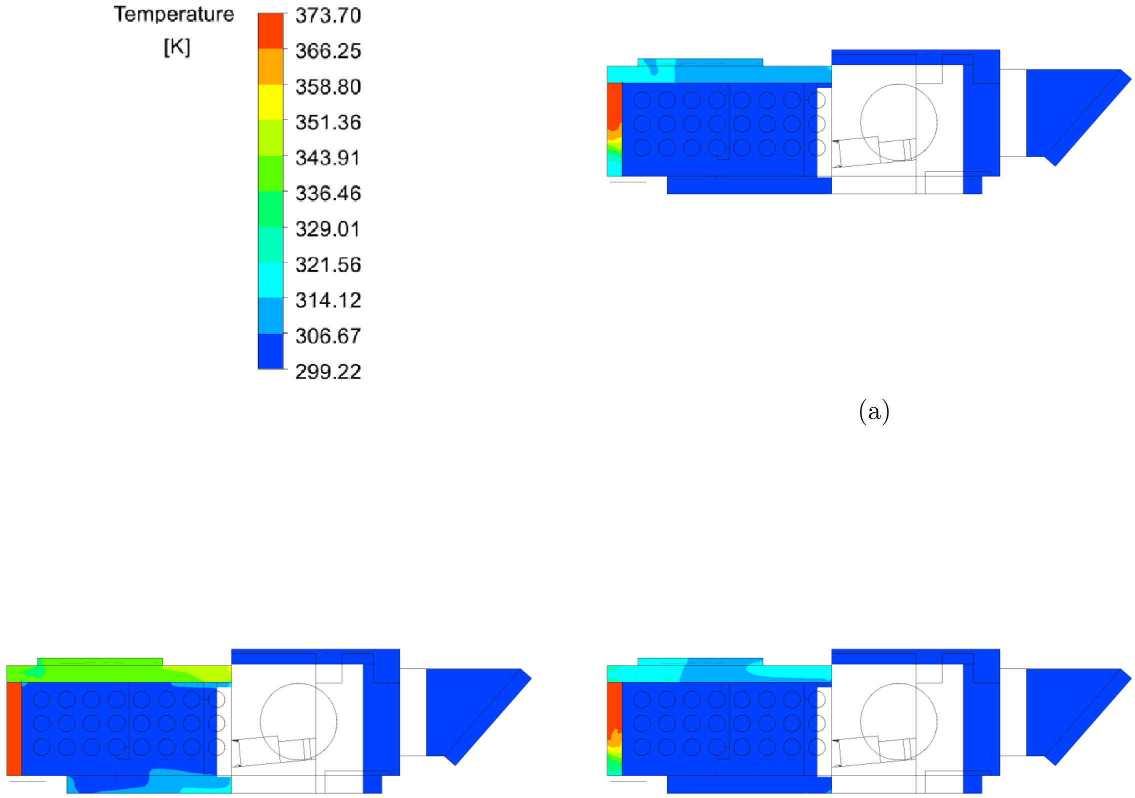

(a)

(b)

(c)

Figure 4.26: Temperature field at V1 plane: a) case A; b) case B; c) case C.

The situation is different in Figure 4.26.b, where the whole available inter-pipe space is filled with steam together with the labyrinth baffle on the fan side in part (I) (characteristic red rectangle), which means that, a large quantity of uncondensed steam got into the inlet zone.

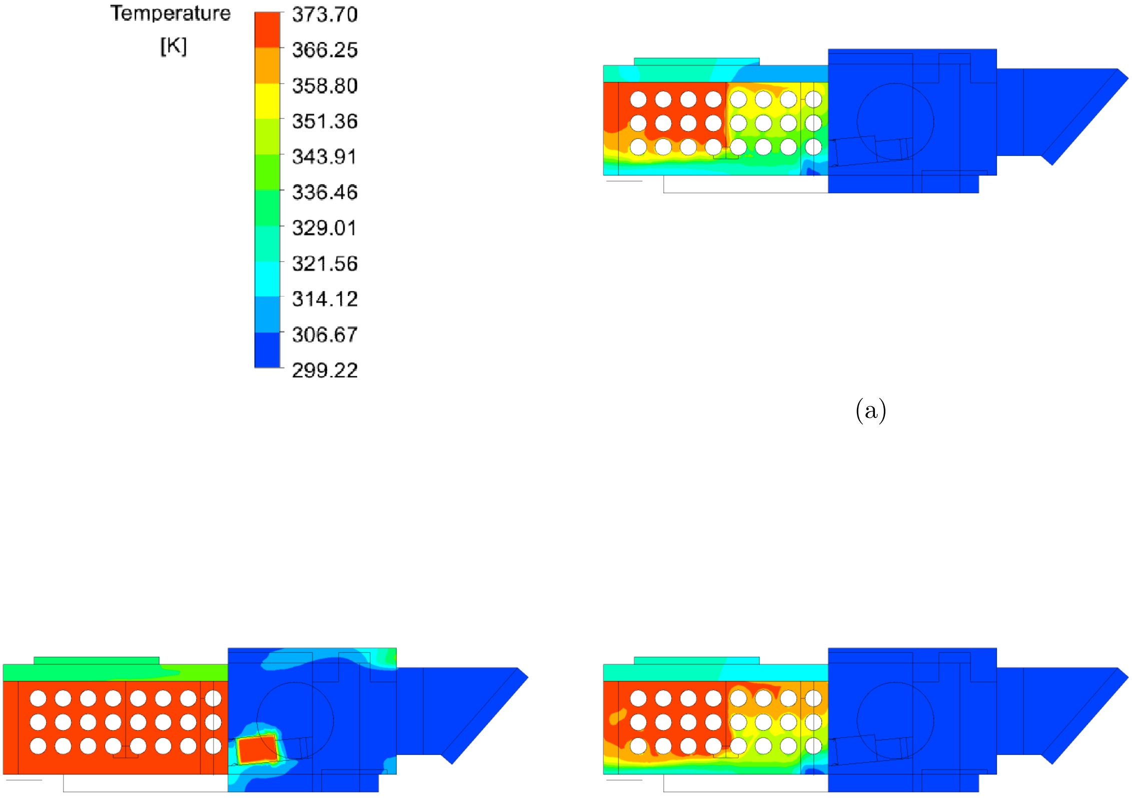

(a)

(b)

(c)

Figure 4.27: Temperature field at V2 plane: a) case A; b) case B; c) case C.

In Figure 4.28 temperature fields at V3 cross section are presented for the investigated cases. V3 plane crosses the right hand side bundle, which is located on the opposite side than the steam inlets. Figures 4.28.a and 4.28.c concern cases A and C, respectively. Both figures show temperature stratification - similarly to Figures 4.27.a and 4.27.c. However, temperatures in the bundle are significantly lower, especially after baffle 1.1 (in the middle of the bundle), which divides the profile into two zones - of temperature 336-373 K (before the baffle) and 329-358 K (after the baffle). Lower temperature regions are coincide with the lower steam fraction.

Contrary to Figures 4.27.a and 4.27.c where whole inlet zone has uniform temperature, on this side, the labyrinth baffles are warmer (about 321 K). There is one explanation for this situation - fluid circulation through the apertures is asymmetrical: apparently the air flows into the left hand side bundle while in the right hand side bundle flow occurs in the opposite direction. Unfortunately, any reliable flow measurements through the apertures were not successful, hence it cannot be confirmed.

In case B presented in Figure 4.28.b, temperature field looks almost identical as in the left hand side bundle (Figure 4.27.b). Here, the right hand side bundle is also filled with steam, which is strongly visible in the labyrinth baffle on the other side of aperture.

At the V4 plane, the temperature difference between the bundles is clear as shown in Figure 4.29.a and 4.29.c. In these cases, a temperature gradient on the air side also can be noticed, while case B presented in Figure 4.29.b seems to be uniform, both on the steam and on the air side.

Figure 4.30 provides the best view on the temperature distribution in the CH. In Figure 4.30.b, where case B is presented, HE completely filled with steam stands out with air temperature in the peripheral pockets increased from 299 to $\approx$ 344 K. In the inlet zone even higher temperatures are noted, but it results from the excess steam mixing and diluting with the air. The remaining two cases are shown in Figure 4.30.a and 4.30.c, where HE temperature stratification took the form of four zones separated by baffles 1.1 and 2.1. Numerical solution indicates that not only the right hand side bundle but also the pipe downstream baffle 1.1 in the left hand side bundle are not utilised as efficient as it could be.

Both designs have been examined in the three working conditions listed below:

- A - laboratory conditions, steam from generator of power 3.4 kW,
- B - laboratory conditions, steam from generator of power 27 kW,
- C - operating conditions, cooperation with combi-steamer 100°C steam mode.

Numerical models were validated for the same cases. Case A in regard to heat load

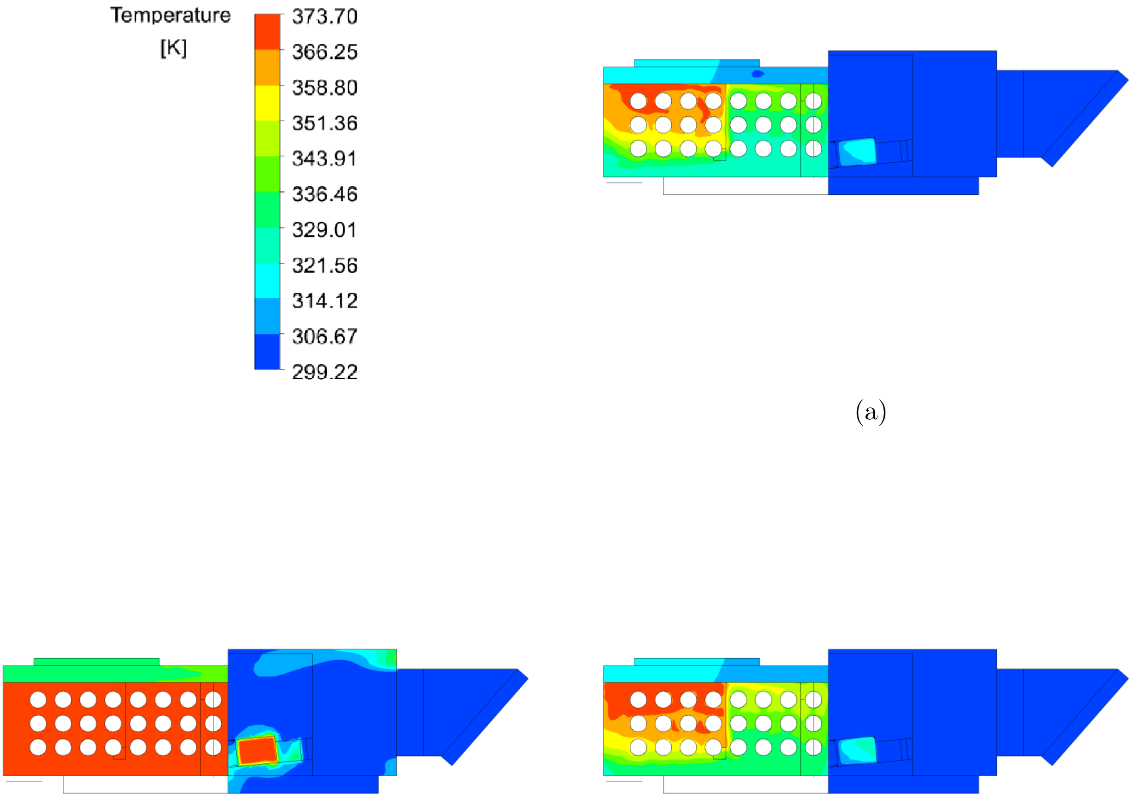

(a)

(b)

(c)

Figure 4.28: Temperature field at V3 plane: a) case A; b) case B; c) case C.

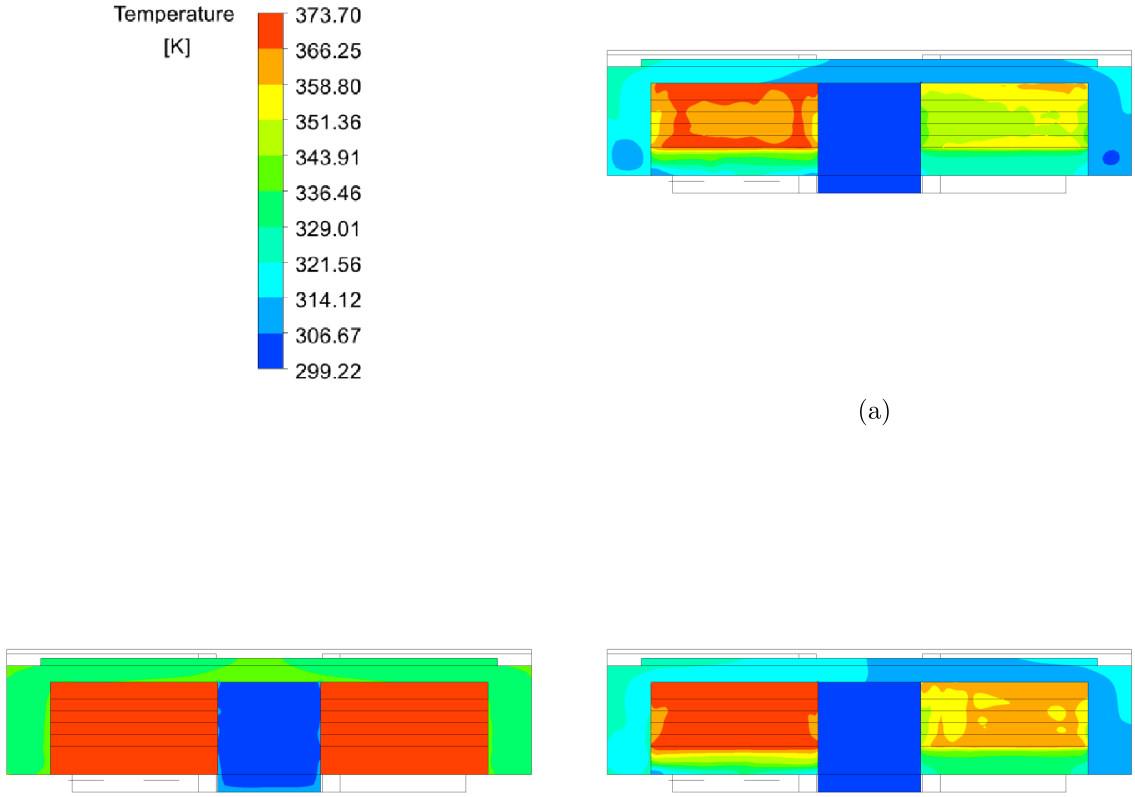

(a)

(b)

(c)

Figure 4.29: Temperature field at V4 plane: a) case A; b) case B; c) case C.

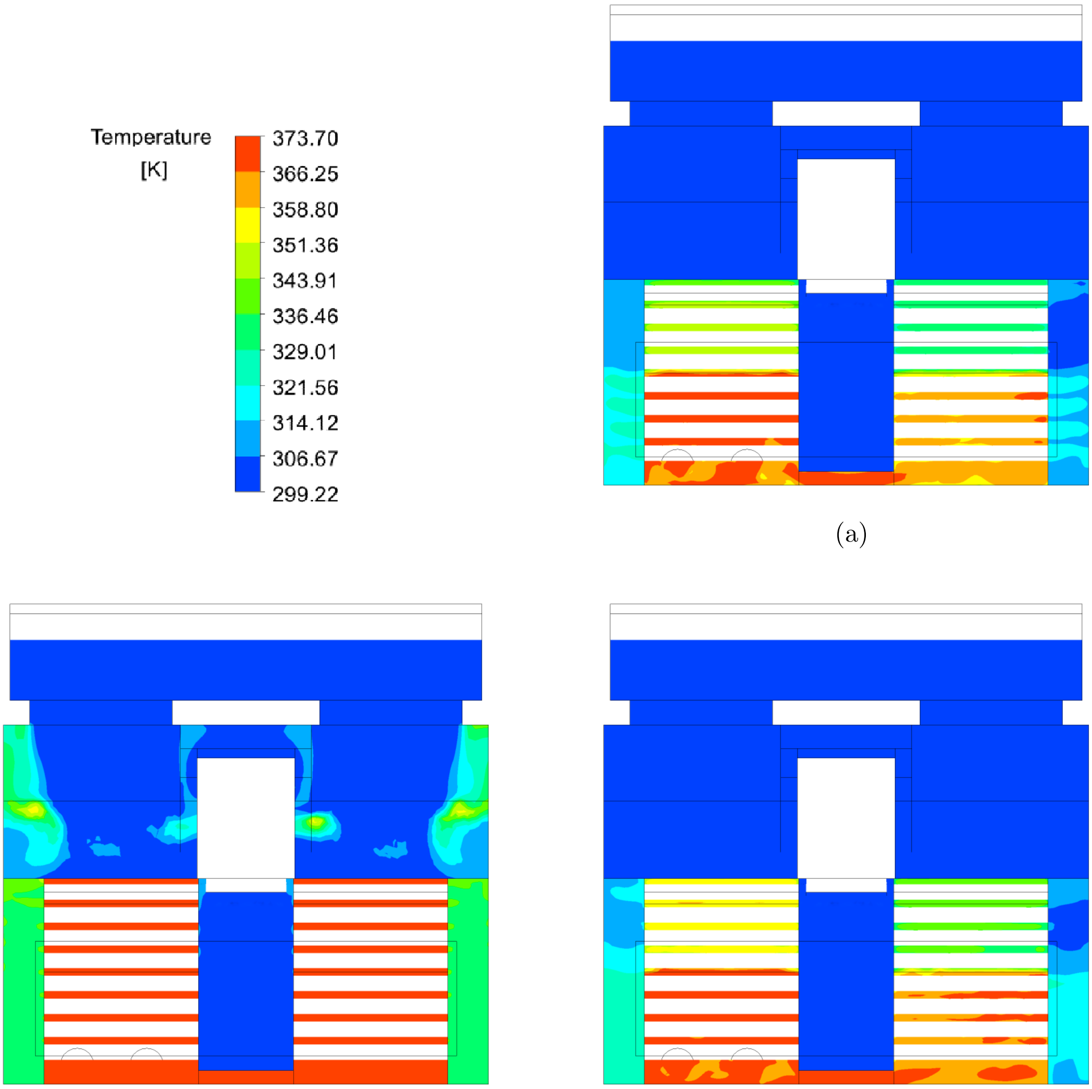

(a)

(b)

(c)

Figure 4.30: Temperature field at V4 plane: a) case A; b) case B; c) case C.

is similar to the casual cooperation with the combi-steamer (case C). However, it is more reliable than C due to precisely controlled test conditions. Case B constitutes an extremely high heat load, such as the condensation hood will never has to cope with. Nevertheless, it has been included in the research to test the maximum condensation potential of the device.

Table 4.7 contains the measured and numerically investigated parameters at the inlet and outlet of the condensation hood. Inlet parameters have *in* subscript and outlet *out*. Steam flow rate $\dot{m}_{steam}$ is inlet quantity, while the condensate flow rate $\dot{m}_{cond}$ is outlet. Ambient pressure is denoted by p_{amb}.

Numerical results of the original device in comparison with the measurements are gathered in table 4.7. Measured inlet parameters, naturally, are the same as the ones applied in the model. Case B is characterized by the highest steam flow rate (about ten times the nominal one). The most important parameter is the condensation efficiency η_{cond} defined as steam to condensate mass flow rates ratio. In cases A and C (normal working conditions) both experimental and CFD provided η_{cond} are at over 90% (except for case C Exp. value). In in case B, condensation efficiency decreased to around 25%, however the steam flow rate is in this case about 10 times greater than the nominal one.

Table 4.7: Model of the original condensation-hood: inlet and outlet parameters. Exp - experiment; CFD - CFD model.

Case:		A		B		C	
	Unit:	Exp:	CFD:	Exp:	CFD:	Exp:	CFD:
p_{amb}	Pa	98700		99770		99770	
phi_{in}	%	57.6	59.1	29.5	30.2	29.3	29.4
t_{in}	°C	27.5	27.5	26.1	26.1	26.1	26.1
$\dot{m}_{air,in}$	kg/s	0.184	0.184	0.185	0.185	0.185	0.185
$\dot{m}_{steam}$	g/s	1.18	1.18	11.49	11.49	1.62	1.62
$\dot{m}_{cond}$	g/s	1.16	1.13	3.08	2.69	1.42	1.54
t_{out}	°C	41.7	41.6	64.4	62.4	42.5	45.4
ϕ_{out}	%	26.5	28.7	31.4	37.1	13.7	11.3
η_{cond}	%	98. 1	95.7	26.8	23.4	87.7	95.1

Condensation efficiency η_{cond} is the most important parameter indicating the quality of this kind of device. Original condensation hood already has high η_{cond} - about 90% in cases A and C. In case B (extremal heat load) this parameter drops to about 27%.

CFD-provided condensation efficiencies in cases A and C are higher by approximately 7% while in case B is lower by about 3%.

Figure 4.31 shows also the locations of thermocouples denoted by T1-T8. Thermocouples T1-T4 were mounted in the heat exchanger on the steam side - in the middle of the bundle. T1 and T3 behind the second column of the pipe, between the upper pipe and the middle one. T2 and T4 were behind the fifth column, between the upper and the middle one as well. Thermocouples T5-T8 were mounted at the air side located at the fourth pipe column. Thermocouples T6 and T8 were near outlet of the middle pipe, while T5 and T7 were slightly above the upper pipe.

Measured temperatures at the points indicated in Figure 4.31 compared to CFD simulation are shown in Table 4.8. The temperatures relatively correspond to each other only in case B excluding point Exp. T4, where the thermocouple failed. In other cases, the highest discrepancies occurred at points T1-T4 located on the steam side of the heat exchanger. For such a situation, two factors can be responsible. At first, in experiments, each of these points stands for a thermocouple placed inside the condensation hood. In the CFD model, temperatures are average of the closest surroundings of the potential thermocouple location, because it is difficult to unambiguously define actual location of the thermocouple. Temperature gradients, transient character of the flow, and location uncertainty - all of these could contribute to the discrepancies. Secondly, condensation could occur on the thermocouples (especially T1-T4) having effect on the measured values.

Table 4.8: Model of the original condensation-hood: comparison of temperatures inside the heat exchanger. Exp - experiment; CFD - model.

Case:		A		B		C	
Point:	Unit:	Exp:	CFD:	Exp:	CFD:	Exp:	CFD:
T1	°C	69.1	96.1	98.8	100.0	71.0	98.8
T2		53.9	77.3	98.3	100.0	42.3	89.6
T3		48.4	91.2	98.5	100.0	50.1	94.0
T4		38.0	60.3	–*	100.0	34.5	71.5
T5		59.4	44.0	78.2	60.2	37.6	46.4
T6		49.4	45.5	72.2	59.7	35.3	48.2
T7		55.9	52.2	78.9	60.0	49.6	54.0
T8		34.4	49.8	79.7	60.1	51.8	52.2

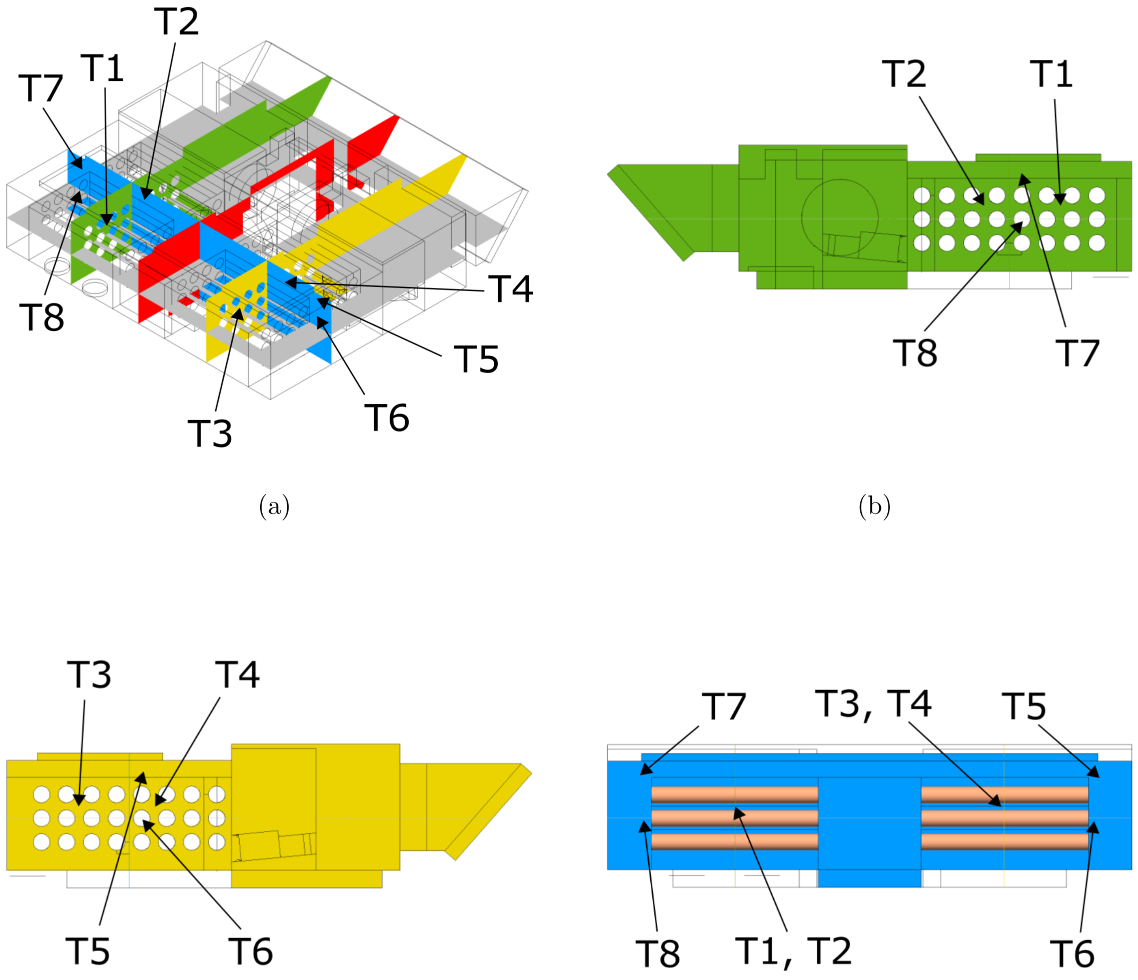

(a) (b)

(c) (d)

Figure 4.31: Thermocouples' location across the heat exchanger: a) global view; b) V2 plane; c) V3 plane; d) V4 plane.

4.5 Summary

The development of the numerical model of the condensation hood requires introducing several geometrical simplifications of the fan and the pipes in the heat exchanger. Thus, two sets of UDFs (two models) have been prepared and introduced.

Model of the fan included the transportation of the air and water content from the fan inlet to the outlet. Additionally, a velocity profile provided by the measurements has been applied.

Second introduced model is the model of the condensation. It included the pipes and a set of energy and mass source terms. The pipes have been removed from the geometry and replaced by a set of boundary conditions and UDFs. Such an approach forced the introduction of the condensation model (because the pipes geometrically no longer existed), that transport the air (with water content) from the pipe inlet to the outlet, transfer energy from the condensing steam to the air in the pipe, calculate the air temperature at the outlet and removes condensed steam from the domain. This allowed to avoid the simulating of a complex two-phase flow with phase change and, as a result, enabled significant numerical mesh and computational effort reduction.

The developed numerical model of the original condensation hood provided results that have a good agreement with the measurements. Introduced geometrical and process simplifications allowed for relatively fast obtainment of numerical results. It also allows for the identification and development of potential modifications of the heat exchanger that are described in detail in the following chapter.

Chapter 5

Modified construction

5.1 Introduced modifications

Once the original device has been simulated and successfully validated, some modifications to the heat exchanger were proposed and implemented in the numerical model. The experimental and numerical results indicated that the original condensation hood is overestimated, which is manifested by a very high condensation efficiency, amounting to approx. 90%. For this reason, it was decided to maintain such high efficiency (with an acceptable non-significant loss), and instead the focus was laid on simplifying the construction to make it cheaper to produce in terms of labour and materials.

The new model shares majority of the geometry as well as the whole set-up (maintaining intact UDFs) with the previous original construction model. The modifications' were developed based on the numerical and experimental results from the original construction and are focused on the improvement of steam distribution in the pipe bundles, as the temperature field (Figure 4.29) clearly indicates that, the right hand side bundle is far less covered by the steam.

The heat exchangers of both models have been presented in Figure 5.1. In Figure 5.1.a an original one is showed. It consists of two bundles of pipes (1.a) denoted by horizontal orange rectangles. Between the bundles, there is an air distribution chamber (DC) (green), that is supplied with air by the fan. Next, the air flows through the pipes (green arrows) and leaves the main part of the exchanger. Steam inlets (IV) introduces steam into the exchanger (blue zone) according to red arrows. Both bundles are inter-connected by means of the channel (2.a). The exchanger is equipped with baffles that increase the steam residence time between the pipes. There are four baffles per exchanger: two in the right hand side bundle ((L1.1) and (L1.2)) and two in the right hand side ((R2.1) and (R2.2)) as indicates Figure 5.1.a.

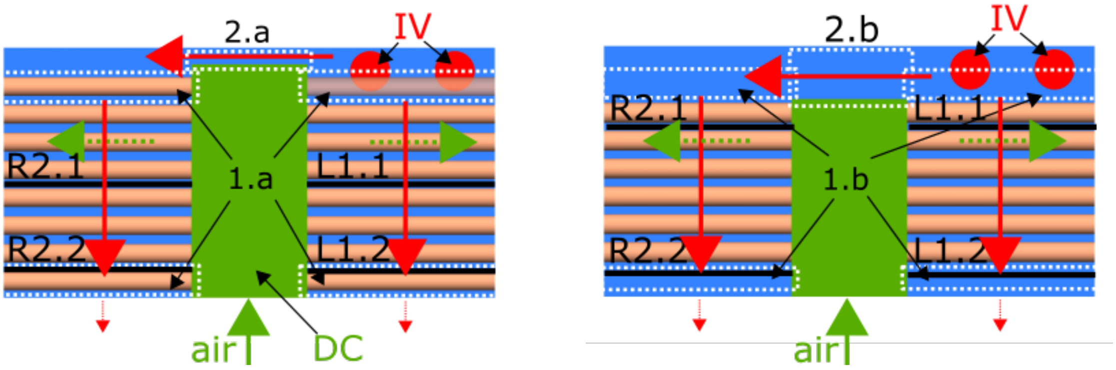

(a) (b)

Figure 5.1: Heat exchangers' overhead view: a) original construction; b) modified construction. 1.a - pipes in original HE; 1.b - pipes removed; 2.a - original steam channel; 2.b - expanded steam channel; IV - steam inlets; air - air inlet; DC - air distribution chamber; L1.1 - frontal left baffle; L1.2 - rear left baffle; R2.1 - frontal right baffle; R2.2 - rear right baffle.

On the right hand side (Figure 5.1.b) a modified heat exchanger is presented. Two rows of the pipes (1.b) have been entirely removed. The first row (the nearest one to the steam inlets (IV)) was removed to expand cross-sectional area of the channel (2.b), while the last row was due to the smallest air flow through the pipes and the lowest steam content in this part of the HE. Baffles (L1.1), (L1.2) and (R2.1), (R2.2) have been modified as well. Frontal baffles (from the steam flow rate perspective) (L1.1) and (R2.1) have been moved between the two first columns of the pipes, while (L1.2) and (R2.2) remained at their original column-wise positions.

Figure 5.2 presents a side view of both heat exchangers (original and modified one). Figure 5.2.a and Figure 5.2.c shows original exchanger - left hand side and right hand side bundles, respectively. Red arrow denotes schematically steam propagation into the bundles. Baffles (L1.1)-(R2.1) and (L1.2)-(R2.2) are identical and are located as the figure indicates. Numerical simulations showed that the rear baffles (L1.2) and (R2.2) have no significant impact on the steam trajectory. Additionally, the lower pipes before the frontal baffles (L1.1) and (R2.1) were poorly covered by steam. Hence, the introduced changes to the second model are applied also to the baffles.

Figures 5.2.b and 5.2.d show left hand side and right-hand side bundles of the mod-

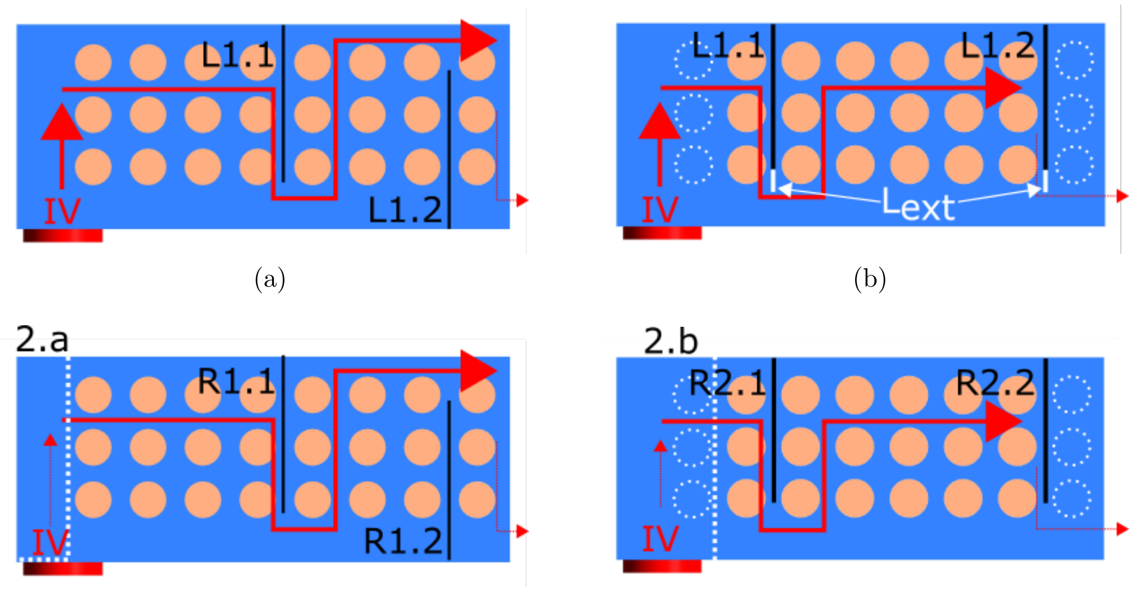

(a) (b)

(c) (d)

Figure 5.2: Heat exchangers' side view: a) original construction left hand side bundle; b) modified construction left hand side bundle; c) original construction right hand side bundle; d) modified construction right hand side bundle. 2.a - original steam channel; 2.b - expanded steam channel; 3 - steam inlets; L1 - frontal left baffle; L2 - rear left baffle; R1 - frontal right baffle; R2 - rear right baffle; L_{ext} - left baffles' extension.

ified heat exchanger, respectively. Frontal baffles (L1.1) and (R2.1) have been moved closer to the steam inlets (IV) and located between the first two pipe columns. Rear baffles (L1.2) and (R2.2) were mounted in the same manner as the frontal ones - at the top, to increase their impact on steam propagation. As a lighter gas than air, the steam rises quickly towards the upper part of the exchanger. Hence, mounting both pairs of baffles at the top enabled the steam to be locked between them and among majority of the pipes. Additionally, left-hand side baffles (L1.1) and (L1.2) are longer than their right-hand side counterparts by the length L_{ext} shown in Figure 5.2.b. Such a solution reduces cross-sectional area available for the steam flow and additionally forces the steam into the right hand side bundle.

5.2 Numerical model

As it was already mentioned, the numerical model of the modified construction shares with the original model geometry, general set-up, boundary conditions, and UDFs. Calculations were ran at $k-\varepsilon$ and species transport models.

The geometry was slightly modified and hence the mesh is adjusted also as shown in Figure 5.3, where in Figure 5.3.a is original mesh, while in Figure 5.3.b modified mesh. Removed pipes were unsuppressed and merged with the geometry to enhance the mesh on the steam side ((1) and (2) in Figure 5.3). Extension of the channel connecting the tube bundles was brought down to the wall BC displacement keeping the mesh intact. Additionally, the labyrinth baffles in the inlet zone (3) were omitted as they have no important impact on the steam/air flow in the HE as well as on the condensation process. This allowed for a significant mesh improvement in the area, practically eliminating tetrahedral elements, which had a positive impact on the model's convergence and stability. Labyrinth baffles, however, were present in the real construction. The final mesh consists of 1.2 M elements, mainly hexahedral. The removed pipes have been disabled in the UDF as well, maintaining the rest of the UDF unchanged.

5.3 Results

Modified construction's model was validated in the same three cases as the original construction, namely: case A where real working conditions were maintained in

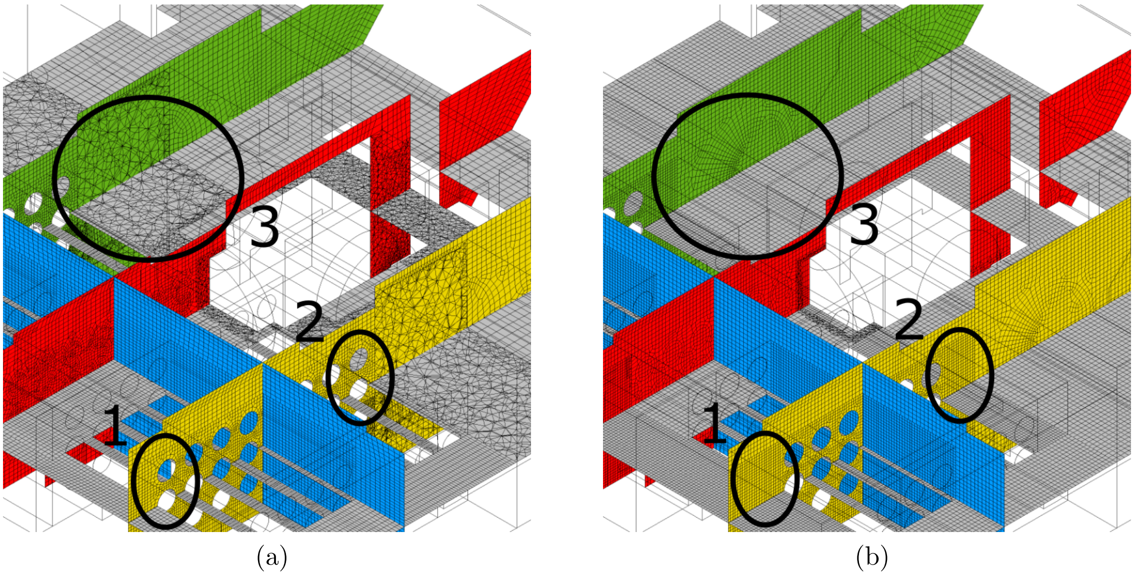

Figure 5.3: Mesh comparison: a) original construction; b) modified construction. 1 - removed first column of pipes and extended channel; 2 - removed the last column of pipes; 3 - area of the labirynth baffles.

laboratory conditions, case B standing for an extremely high steam load (about 10 times greater than the nominal one), and case C being a test with the dedicated combi steamer. Data for validation was provided by the original construction measurements, and once the validation of the modified model was successful, a prototype has been built and tested in the mentioned above cases. Then the numerical model was computed again, but this time modified construction measurements were used and these results, both numerical and experimental, are hereby presented in the following section.

For better clarity, all figures presented in this section are grouped in pairs OC-MC according to the validation cases (A, B, and C). Both models are comparable, so the velocity and temperature profiles of the modified model are shown in the same planes as the original model (see Figure 4.18).

Geometrical changes done to the HE (removal of the first and last tube columns, inter-bundle channel extension) and labyrinth baffles removal in the inlet zone could affect the velocity profile and could impact the entire device. However, simulation has shown that (cf. Figures 5.4-5.6) that impact of those modifications on the overall velocity profile is negligible.

In Figure 5.4 velocity profile in case A of the original construction (Figure 5.4.a) and modified construction (Figure 5.4.b) is presented. No major differences can be noticed. Lack of labyrinth baffles in the inlet zone hardly affected the velocity profile in this part.

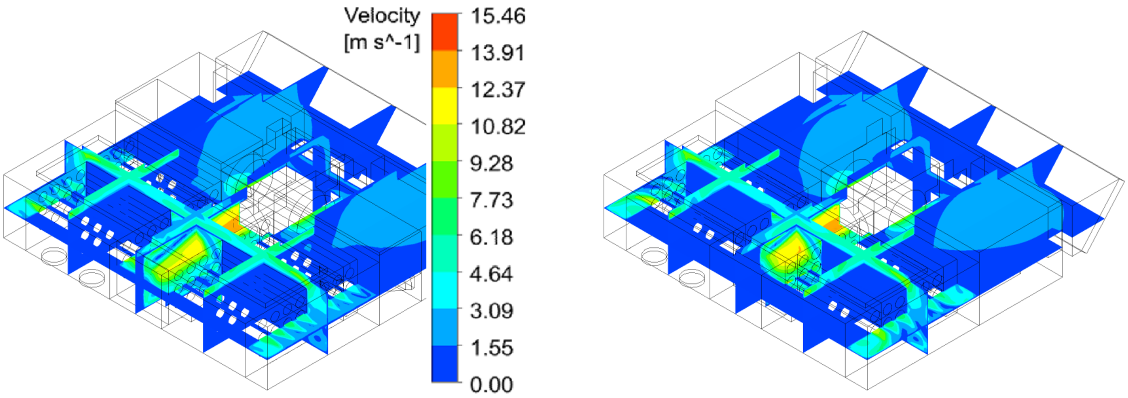

(a) (b)

Figure 5.4: Velocity field comparison of case A: a) OC; b) MC.

Similar situation can be noticed in Figure 5.5, which presents the results comparison of both models in case B. The figure shares the velocity color bar with Figure 5.4. The biggest difference between OC and MC (again, presented in Figure 5.5.a and Figure 5.5.b, respectively) is visible in the HE on the steam side, where in the Figure 5.5.a velocity over 3 m/s can be observed in the left hand side bundle near the steam inlets, the inter bundle channel, and further downstream in the beginning of the right hand side bundle. In Figure 5.5.b however, the velocity over 3 m/s can be observed near the steam inlets only, while the rest of the steam side is uniformly dark blue (velocity less than 1.55). This can indicate that the steam freely can propagate to the right hand side bundle without squeezing through the bottleneck in the form of a narrow inter-bundle channel.

Velocity fields of the OC and MC in case C are presented in Figure 5.6.a and 5.6.b, respectively. Both profiles are similar to the ones shown in Figure 5.4 with no major differences nor anomalies visible.

As the velocity profiles are very similar for both constructions and significant flows occur in the unmodified parts (inlet zone, HE air side), they will not be discussed further and the focus will be on the temperature distributions to evaluate impact of the introduced changes to the steam side of the HE.

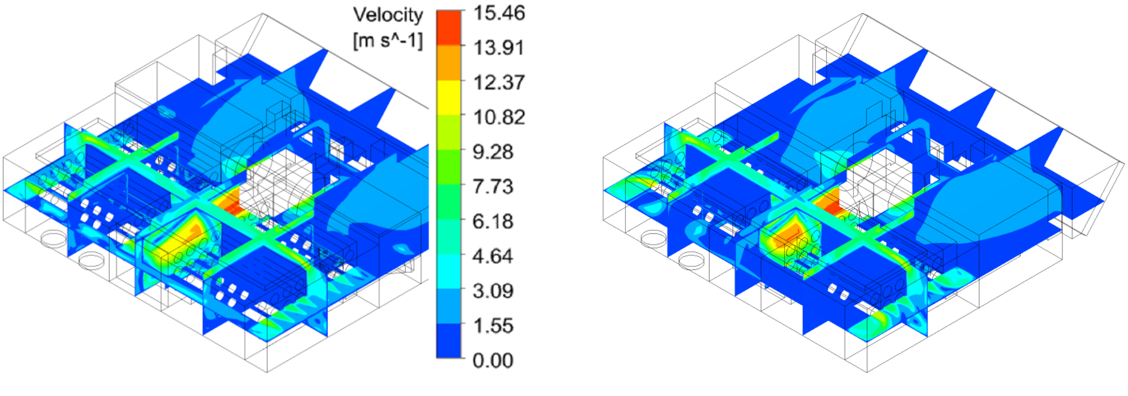

(a) (b)

Figure 5.5: Velocity field comparison of case B: a) OC; b) MC. Colorbar as in Figure 5.4

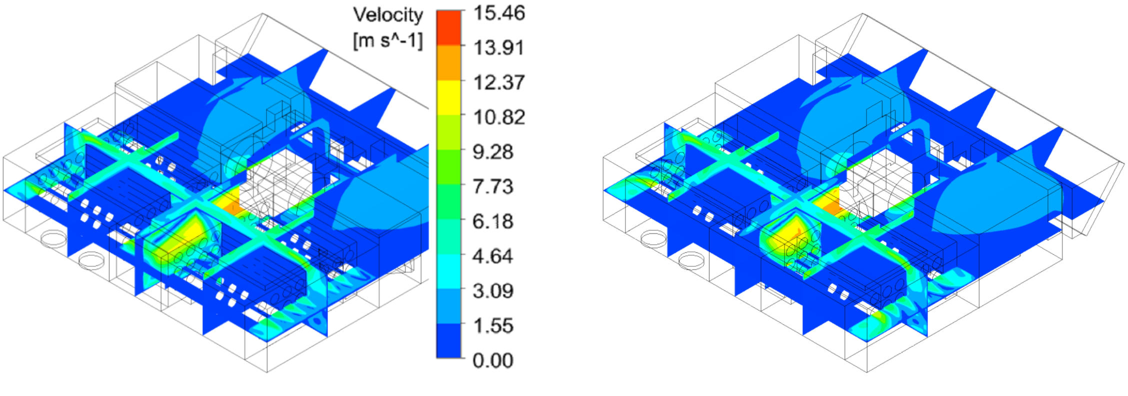

(a) (b)

Figure 5.6: Velocity field comparison of case C: a) OC; b) MC. Colorbar as in Figure 5.4

Similarly to the Figure 5.4.a, Figure 5.7.a is also equipped with a color bar, but this time scaled in Kelvins. Figures 5.7-5.9 present overall temperature distributions in the OC and MC in all the examined cases A, B, and C. All those figures are scaled according to the color bar from Figure 5.7.a.

Temperature distribution of case A is presented in Figure 5.7, where original construction is shown on the left hand side (Figure 5.7.a) and the modified construction on the right hand side (Figure 5.7.b). Steam side of the HE in both constructions differs significantly: in the OC the left hand side bundle is noticeably hotter than the right hand side (358-373 K compared to 343-373 K, respectively), while in the MC both bundles are supplied with steam in a uniform manner. The entry regions of both bundles and the inter-bundle channel are almost uniformly filled with steam, as indicated by a red colour in Figure 5.7.b.

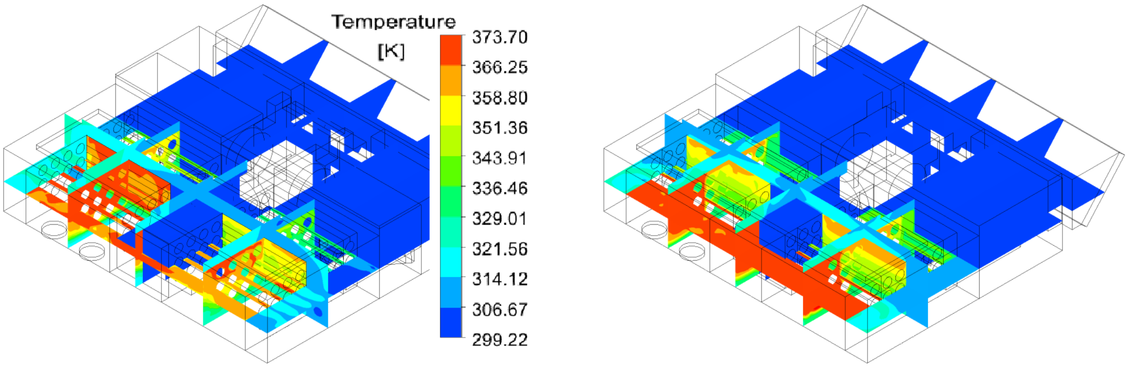

(a) (b)

Figure 5.7: Temperature field comparison of case A: a) OC; b) MC.

In Figure 5.8, where temperature distributions of case B are compared, both constructions are characterized by a HE (steam side) completely covered by steam. The differences can be noticed in the inlet zone, where impact of the labyrinth baffles is visible: in Figure 5.8.a (with the baffles) the steam flow is divided so part of it is pulled towards the fan, while the rest flows near the opposite wall (green-yellow field). In Figure 5.8.b (no baffles) the temperature distribution in the inlet zone looks opposite - the only location where the temperature increase is visible is located near the fan inlets. The labyrinth baffles, as it was mentioned earlier, were not present in the numerical model for mesh refinement purposes, but were present in the actual prototype, the same as in the original construction.

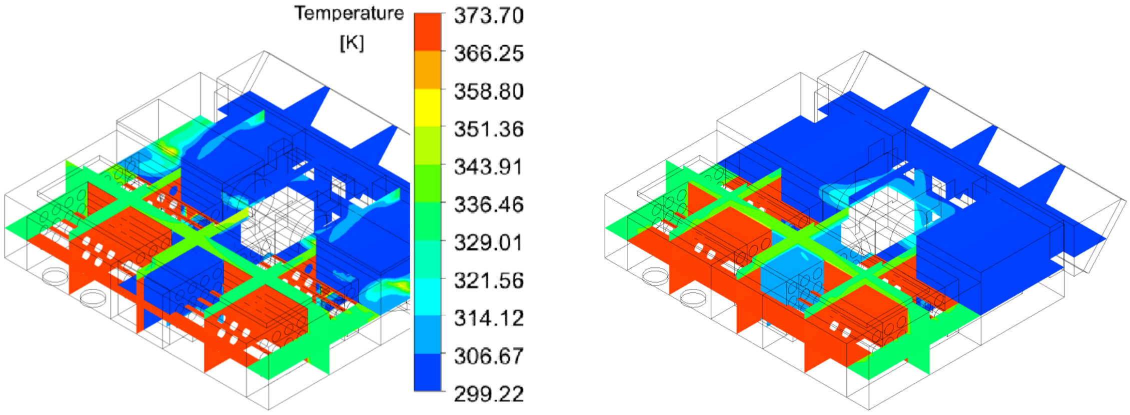

(a) (b)

Figure 5.8: Temperature field comparison of case B: a) OC; b) MC.

In the actual working conditions of case C, showed in Figure 5.9, both temperature profiles look similarly as in Figure 5.7, where temperature in MC seems to be almost symmetrical (Figure 5.9.b) contrary to OC presented in Figure 5.9.a.

Figures 5.7 and 5.9 clearly indicate that the proposed modification to the condensation hood's HE works as intended. However, in the following figures a more detailed view on both HEs will be provided.

Temperature distributions inside both bundles are presented in Figure 5.10, where in the left hand side (Figure 5.10.a and 5.10.c) original construction is shown and in the right hand side (Figure 5.10.b and 5.10.d) modified construction. As in the case of the OC, the temperature profiles in both bundles are different - righ hand side bundle (Figure 5.10.c) is 30°C colder than the left hand side bundle (Figure 5.10.a), a situation in the MC case is opposite: the temperature profiles in both bundles are almost identical as indicated in Figure 5.10.b and 5.10.d. The steam is locked between the baffles in the inter-pipe space.

In the left hand side of Figure 5.11, the OC temperature profiles are presented, while in the right hand side of the figure the MC temperature is shown. In both cases both bundles are visible and both are entirely covered by steam. The only difference is

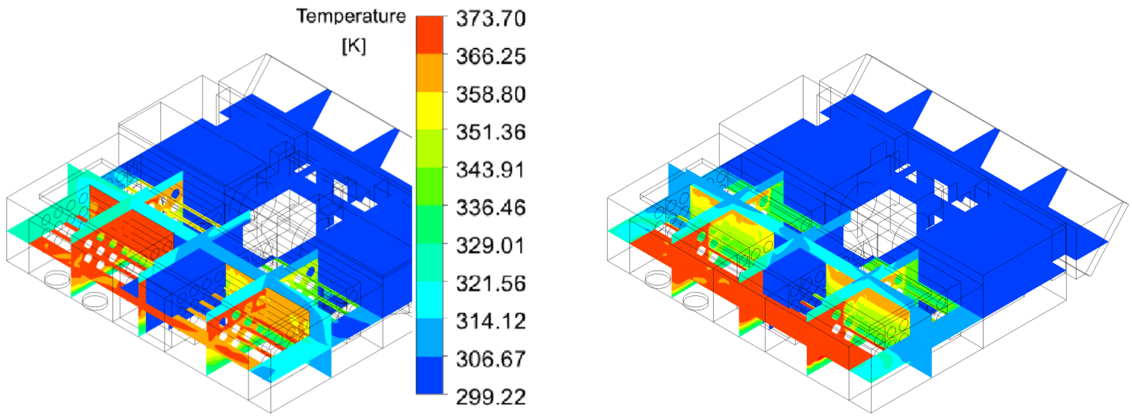

(a) (b)

Figure 5.9: Temperature field comparison of case C: a) OC; b) MC.

the inlet zone, where in the MC model labyrinth baffles are omitted. Due to the high steam load (over 10 times the nominal one), both constructions work in the same way.

Real working conditions that are the very essence of case C, are slightly more demanding (but still comparable) than the laboratory conditions of the case A and are presented in Figure 5.12 in the same manner, as in Figures 5.10 and 5.11. In this case, the temperature distribution in the left hand side bundles of both constructions (Figure 5.12.a and 5.12.b) are almost identical as in Figure 5.10.a and 5.10.b. However, due to the higher steam mass flow rate in case C by about 16%, difference can be noticed in the right hand side bundle, especially in the OC (Figure 5.12.c), where the temperature is clearly higher. This implies that a larger portion of the steam got into this bundle. In the MC case (Figure 5.12.d), in the same bundle, the difference compared to case A (Figure 5.10.d) is hardly visible.

Figures 5.13 to 5.12 provide temperature distribution in the HE of OC and MC from the H1 plane perspective. Similarly to Figures 5.4-5.4, they are split according to the cases A, B, and C, where only the first figure (Figure 5.13) has a color bar, that applies to all three figures. Horizontal plane H1 gives a good view on the temperature profile in both bundles. In case C, presented in Figure 5.13 temperature profiles of the OC (Figure 5.13.a) and the MC (Figure 5.13.b) are quite different. In the OC, the high temperature zone (over 366K) spreads in the left hand side bundle up until baffle L1.1 and to the inter-bundle channel. Downstream, the temperature decreases

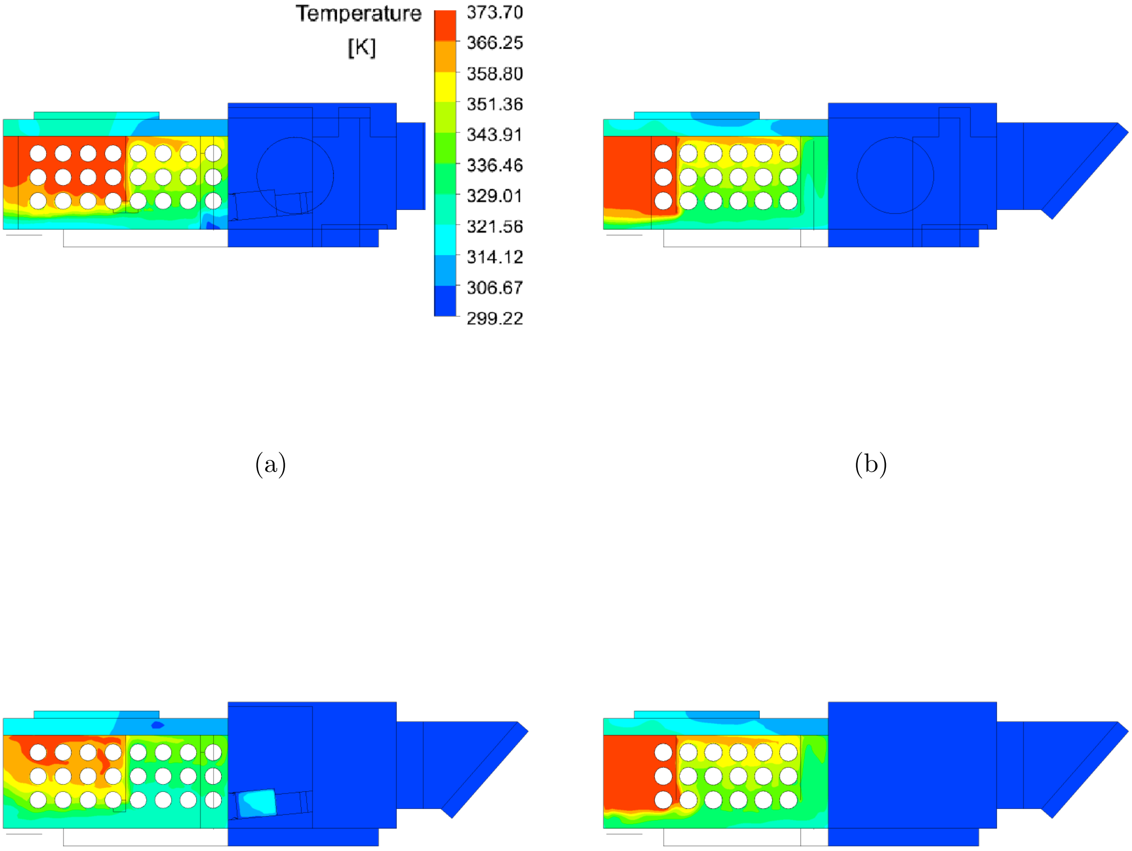

(a) (b)

(c) (d)

Figure 5.10: Temperature field comparison of case A: a) OC - V2 plane; b) MC - V2 plane; c) OC - V3 plane; d) MC - V3 plane.

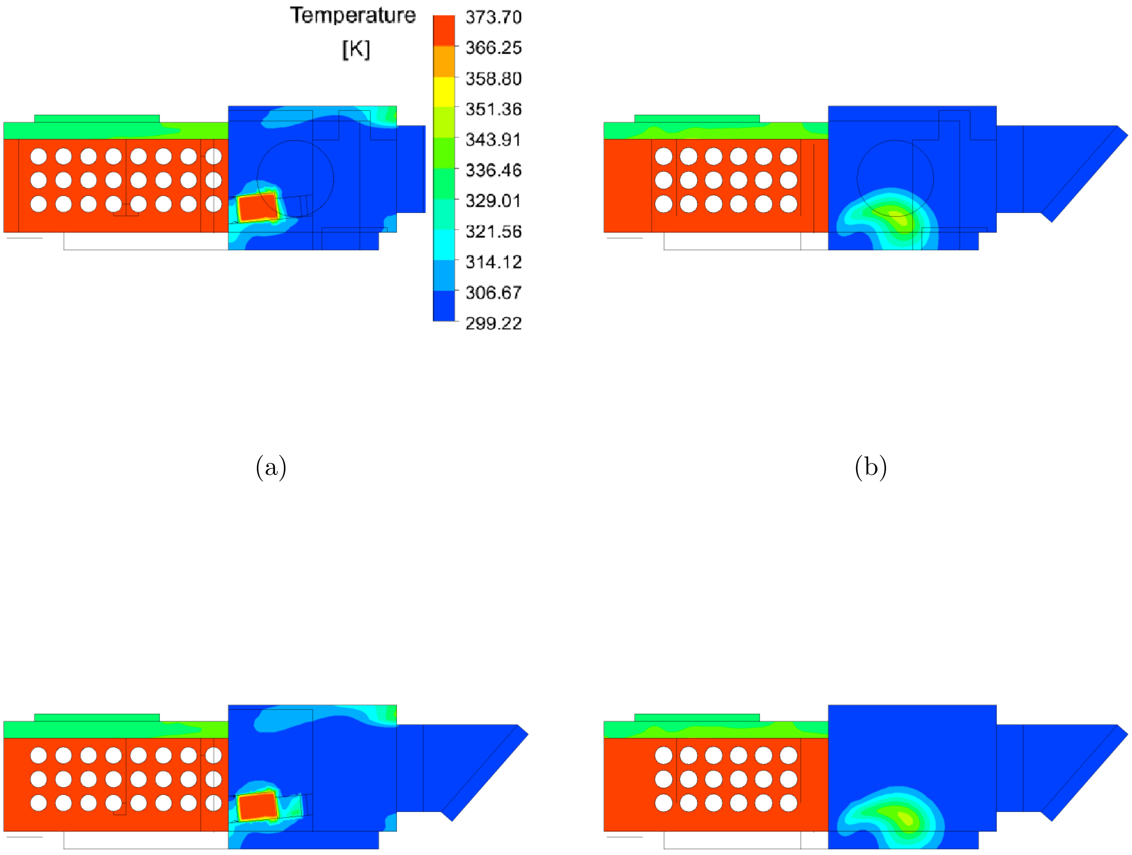

(a) (b)

(c) (d)

Figure 5.11: Temperature field comparison of case B: a) OC - V2 plane; b) MC - V2 plane; c) OC - V3 plane; d) MC - V3 plane.

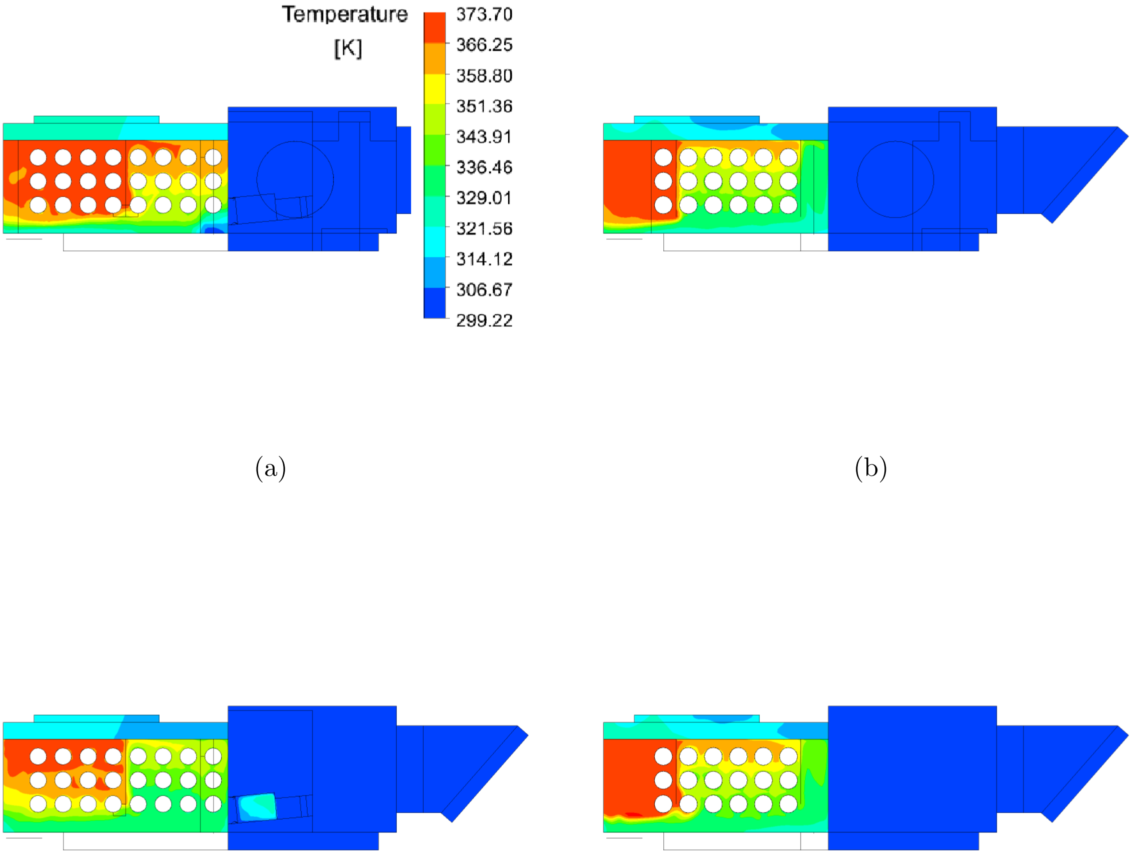

(a) (b)

(c) (d)

Figure 5.12: Temperature field comparison of case C: a) OC - V2 plane; b) MC - V2 plane; c) OC - V3 plane; d) MC - V3 plane.

to about 343-351K, while in the right hand side bundle the temperature amounts to 358-366K before the R2.1 baffle and drops to 239-336K behind the R2.1 baffle. As a result, four temperature zones can be distinguished - two per bundle. The situation in the MC (Figure 5.13.b) is different - there is one high temperature zone (over 366K) spreading upon both bundles symmetrically up until baffles L1.1 and R2.1 and after them the temperature decreases to about 329-336K uniformly and symmetrically. This picture is a clear indicator of the introduced modifications' positive effect on the steam distribution.

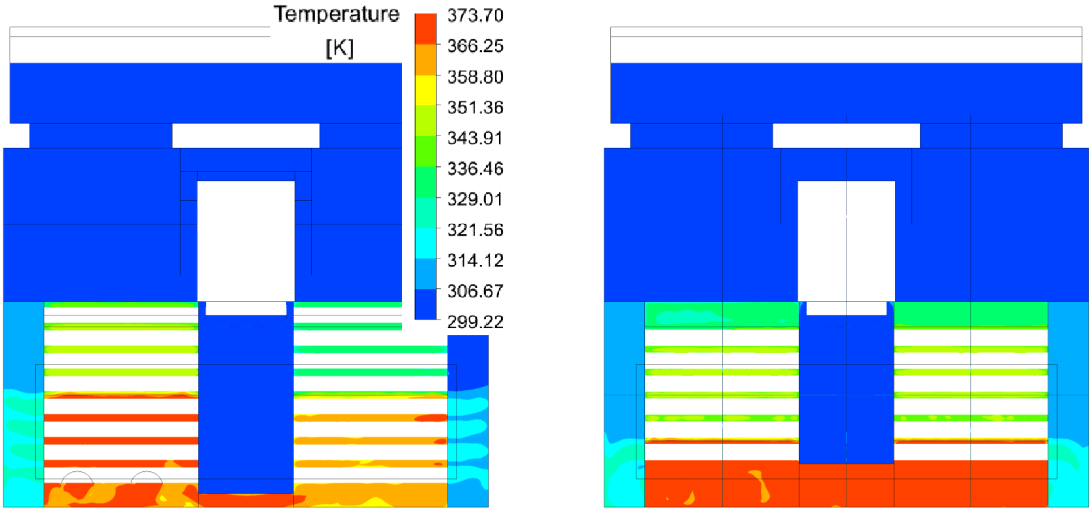

(a) (b)

Figure 5.13: Temperature field comparison of case A: a) OC - H1 plane; b) MC - H1 plane.

As in Figure 5.11, in Figure 5.14 the temperature profile in case B in both HEs is uniform - in both cases both bundles are entirely covered by steam. Differences are in the inlet zone, but as it was mentioned earlier, it results from the lack of labyrinth baffles in the MC model (but only in the model, because the prototype had these baffles mounted).

Temperature distribution in case C for both constructions is presented in Figure 5.15. As it is a real work case similar to the laboratory conditions of case A, the temperature profiles look also similar. Namely, in Figure 5.15.a, where OC is presented, again, four temperature zones can be distinguished - over 366k and 351-358K in the left hand side bundle while 358-366K and 329-336K in the right hand side bundle. Yet, in this case the right hand side bundle seems to be slightly warmer, especially up to the

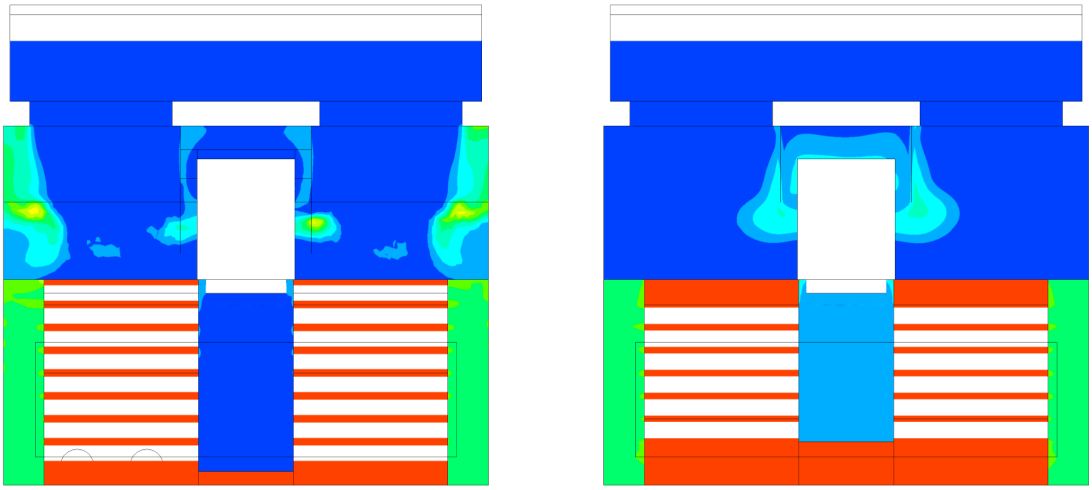
(a) (b)

Figure 5.14: Temperature field comparison of case B: a) OC - H1 plane; b) MC - H1 plane.

baffle R2.1. On the other figure, the MC temperature profile is visible, which also this time is symmetrical and divided into two temperature zones - over 366K upstream the baffles L1.1 and R2.1, and 329-336K in the rest of the steam side. Air temperature in the peripheral air pockets also indicates different steam distribution between the two constructions.

The modified condensation hood model was validated in the same three cases as the original construction: in fully controlled laboratory conditions similar to actual working conditions (case A), extremely high steam load to examine the maximum condensation capacity of the prototype (case B), and actual working conditions with a combi steamer (case C). Inlet and outlet quantities of the modified condensation hood and its numerical model are presented in Table 5.1. In case A condensate flow rate $\dot{m}_{cond}$ provided by the experiment was slightly lower than the simulation indicated, but still, condensation efficiency η_{cond} remained at around 90%. Case B showed that, maximum heat power of the condensation-hood has been reduced due to introduced modifications. Steam flow rate $\dot{m}_{cond}$ decreased for about 20% in comparison to the original construction (Table 4.7). However, experimental and numerical values of $\dot{m}_{cond}$ are very close. Outlet temperature t_{out} is lower in CFD case and as a result, outlet humidity ϕ_{out} is higher. Significant discrepancies appeared in case C in experimental outlet values. Measurements with the combi-steamer were hard to perform, hence

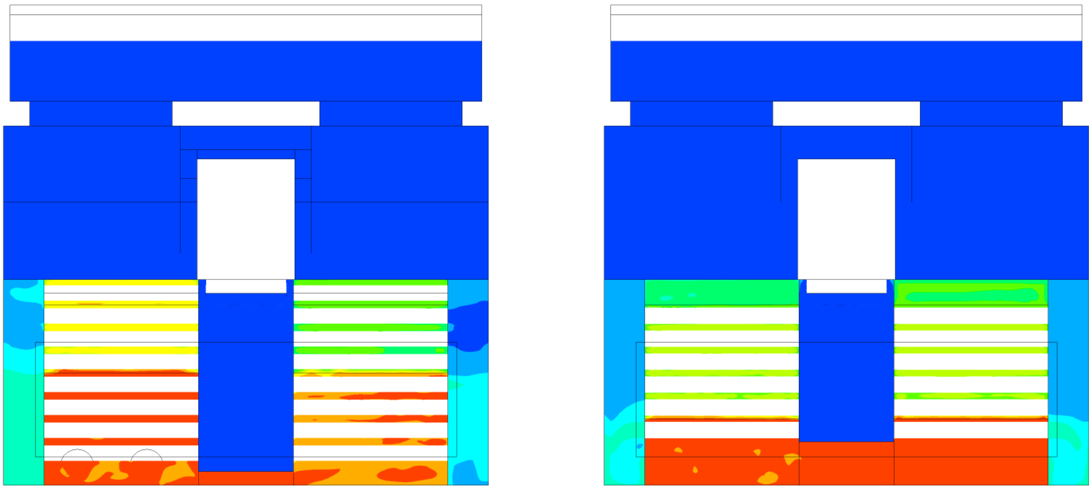

Figure 5.15: Temperature field comparison of case C: a) OC - H1 plane; b) MC - H1 plane.

similar conditions have been recreated in case A and thus they are more reliable.

Table 5.2 contains temperatures inside the heat exchanger (parts *II* and *III*) of the modified condensation hood and their numerical counterparts. The points T1-T8 have been located in the same manner as in the original construction (see Figure 4.31). Results, again, are characterized by high discrepancies, but cases B and C indicate that more steam has been directed to the right hand side bundle. Experimental temperatures T1-T4 (left hand side bundle) and T5-T8 (right hand side bundle) are more uniform than in the original device (Table 4.8).

Experimental inlet-outlet parameters of both examined constructions are presented in Table 5.3. OC denotes the original construction while MC modified construction. In case A modified condensation hood has lower condensation efficiency η_{cond} than original one (88% with respect to the 98%). Measurements were conducted in similar conditions, yet steam flow rates $\dot{m}_{steam}$ differ by approximately 10% to the disadvantage of the MC. Nonetheless, modified condensation-hood condensed almost the same amount of steam (1,14 g/s) as the OC (1,16 g/s). Case B showed that, maximum condensation potential decreased from about 3 g/s (OC) to 2,4 g/s (MC). Hence, η_{cond} decreased from almost 27% to 21% respectively. Due to the difficulties encountered during measurements with the combi-steamer, results in case C are not a fully reliable source of information. According to them, condensation efficiency η_{cond} of MC dropped from 88% (OC) to

Table 5.1: Model of the modified condensation-hood: inlet and outlet parameters. Exp - experiment; CFD - CFD model.

Case:		A		B		C	
	Unit:	Exp:	CFD:	Exp:	CFD:	Exp:	CFD:
p_{amb}	Pa	98700		100480		100670	
ϕ_in	%	55.0	56.5	42.6	43.0	31.5	31.7
t_{in}	°C	27.6	27.6	29.6	29.6	27.4	27.4
$\dot{m}_{air.in}$	kg/s	0.184	0.184	0.184	0.184	0.188	0.188
$\dot{m}_{steam}$	g/s	1.29	1.29	11.49	11.49	1.35	1.35
$\dot{m}_{cond}$	g/s	1.14	1.29	2.41	2.32	1.00	1.35
t_{out}	°C	42.3	43.7	72.6	63.7	40.4	44.1
ϕ_{out}	%	25.9	23.8	25.5	40.2	19.3	13.0
η_{cond}	%	88.0	99.7	21.0	20.2	73.5	99.6

Table 5.2: Model of the modified condensation-hood: comparison of temperatures inside the heat exchanger. Exp - experiment; CFD - model.

Case:		A		B		C	
Point:	Unit:	Exp:	CFD:	Exp:	CFD:	Exp:	CFD:
T1	°C	70.5	75.3	96.9	100.0	51.6	75.9
T2		55.2	78.9	96.9	100.0	42.2	79.8
T3		49.3	77.3	74.4	100.0	52.2	77.8
T4		38.9	81.0	68.9	100.0	34.0	82.4
T5		55.9	41.3	97.4	61.5	46.7	41.6
T6		49.6	37.3	97.7	61.2	37.7	37.5
T7		56.6	37.3	68.4	60.9	46.7	37.8
T8		34.7	39.8	69.8	60.8	32.5	40.4

about 74%. It is unlikely considering other cases: A where η_{cond} loss does not exceed 10% (with approximately 10% higher $\dot{m}_{steam}$); case B where in similar conditions and almost identical $\dot{m}_{steam}$, the condensation efficiency decreased by just 6%.

Table 5.3: Comparison of the original and modified condensation-hood. OC - original construction; MC - modified construction. Only experimental results included.

Case:		A		B		C	
	Unit:	OC:	MC:	OC:	MC:	OC:	MC:
ϕ_{in}	%	57.6	55.0	29.5	42.6	29.3	31.5
t_{in}	°C	27.5	27.6	26.1	29.6	26.1	27.4
$\dot{m}_{air,in}$	kg/s	0.184	0.184	0.185	0.184	0.185	0.188
$\dot{m}_{steam}$	g/s	1.18	1.29	11.5	11.5	1.62	1.35
$\dot{m}_{cond}$	g/s	1.16	1.14	3.08	2.41	1.42	1.0
t_{out}	°C	41.7	42.3	64.4	72.6	42.5	40.4
ϕ_{out}	%	26.5	25.9	31.4	25.5	13.7	19.3
η_{cond}	%	98.1	88.0	26.8	21.0	87.7	73.5

5.4 Modified construction summary

Modified condensation hood model was based on the original construction, maintaining the general HE design, flow organisation, and external dimensions of the device. The experiments proved that the original condensation hood is overestimated. This is manifested by a very high condensation efficiency, amounting to approx. 90%. Hence, it was decided not to improve such high efficiency, and instead the focus was laid on simplifying the construction, while maintaining the efficiency with a non-significant loss acceptable. The improvements developed in such direction were implemented in the second model.

The numerical model development covered further geometrical simplifications applied to the inlet zone, i.e., labyrinth baffles were omitted to improve the local mesh quality by replacing tetrahedral elements by hexahedral ones. This positively impacted the overall solution stability and convergence. The model utilised a practically intact pipe UDF implemented and validated in the original construction model and an unchanged fan UDF as well.

Construction modifications were applied to the HE, where two pipe columns were removed, so the modified construction is equipped with 36 pipes, while the original one was in 48. This change allowed to expand the inter-bundle channel, which significantly improved the uniform steam distribution in the HE. Additionally, the measurement results proved that improving steam distribution compensated the negative thermal effect of 25% of heat transfer surface removal. Hence, it can be concluded that the modified construction is comparable to the original one, while having a lower number of pipes (36 compared to 48 of the OC).

MC numerical model was successfully validated for the same three sets of working conditions as the OC, so both constructions can be compared directly. There were 3 test cases in total: case A mimicking real working conditions in a laboratory environment and under fully controlled conditions; case B, that constitutes over ten times larger steam load than nominal working conditions, was used in the maximum condensation capacity examination of the condensation hood in semi-laboratory conditions; and case C, which concerns cooperation with a dedicated combi steamer - a real working conditions.

Gained knowledge and experience regarding the operation principle of the condensation hood were used in the development of a new heat exchanger, which is described in detail in the following chapter.

Chapter 6

New construction

6.1 Genesis and operation principle

In the previous chapters of this PhD thesis, an extensive experimental and numerical analysis of the original condensation hood is described. Results provided by this analysis were utilised in the development of a modified heat exchanger of CH. The modified construction is characterised by an improved steam path and steam distribution in the heat exchanger, which fully compensates the negative effect of heat transfer surface area reduction by 25% (i.e. pipe removal) and, as a result, the total pipe length has been reduced from 13.5 m to 10.1 m. Modified construction CH has comparable condensation efficiency to the OC, while the overall construction concept is maintained, so it can be easily implemented and mass produced at low cost.

Although the flow organisation and, as a result, the general HE construction based on internally finned pipes are ineffective from the heat transfer point of view, the modified construction, as proved by measurements, can be considered a success. Especially if it comes to implementation. Once the main goal of the project was secured, a completely new HE design was developed to test the condensation potential of a device designed in accordance with a heat transfer theory. As a result, a new redesigned construction (RC) was created.

On the left-hand side of Figure 6.1 is an original design for a CH is presented. On the right-hand side of this figure, the construction of the redesigned heat exchanger is shown. Both devices share the same dimensions, inlet zone with a fan and fan outlet (1), location of the steam vents (3), and air outlet (2). The most important parts of these devices are the heat exchangers indicated by black arrows and dashed lines. The steam produced by the combi-steamer are provided by two steam vents (3) located on one side of the device. In both constructions, the coolant air flows above the upper wall of the HE before it leaves the condensation hood through outlet (2).

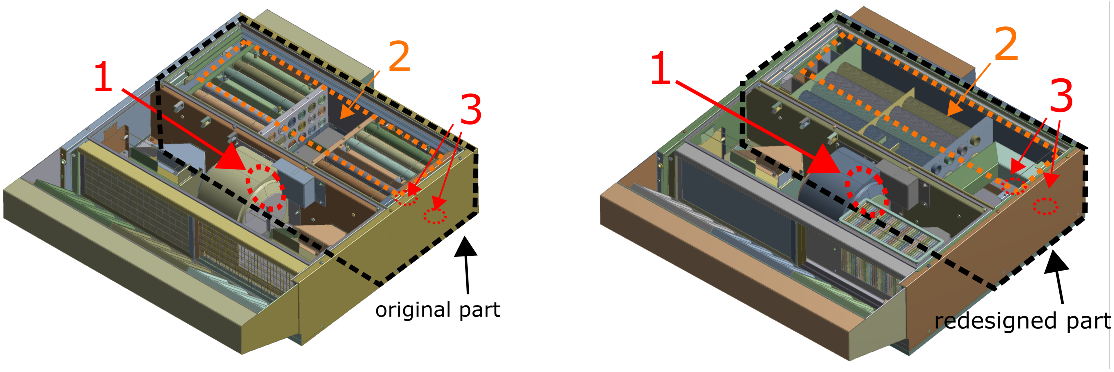

(a) (b)

Figure 6.1: Condensation hood: a) original construction; b) redesigned construction; 1 - fan outlet (coolant air inlet); 2 - air outlet; 3 - steam vents. Figure adapted from images courtesy of Retech Ltd.

In the original construction (Figure 6.1a), the steam is distributed unequally into two bundles of pipes, where flowing through the bundle (through the interpipe space), it is cooled and eventually condenses on the HE pipe's outer surface. The air absorbs the heat released in this process and is withdrawn from the environment by a fan and pulled through the pipes. The steam that did not condense is sucked by the fan, diluted in the coolant air, pulled through the fan outlet (1) to the pipes, and finally released to the environment through the air outlet (2). Because the dominant thermal resistance in the overall heat transfer between steam and air lays on the air side, the pipes are internally finned. Such a solution is technologically complex, expensive, and time-consuming to manufacture. There are also problems to guarantee waterproofed flow paths in the heat exchanger. Taking into account all disadvantages of this solution, it seems to be natural to search for a cheaper and simpler construction, while maintaining the condensation efficiency at a comparable level.

In the redesigned construction (RC), the pipe bundles were merged and moved to the device's right-hand side (opposite side to the steam vents (3)). Instead of flowing into the distribution chamber (space between the bundles where the coolant air is pulled by the fan) and then into the pipes, now the air flows directly into the interpipe space. The total heat transfer surface area is increased using external fins that are much thinner and more numerous than their counterparts in the OC. This solution allowed for reduction in the number of internally finned pipes from 48 (which corresponds to 13.5 m of total pipe length) to only 5 externally finned ones (which corresponds to 4.7 m of total pipe length). In internally finned pipes, the fins' number and geometry are limited by the pipe internal diameter cross-section, which makes that solution cumbersome and less efficient. In the proposed design, the primary constraint is only the HE shell dimension, which affects pipe configuration.

The redesigned heat exchanger finally consists of 5 U-shaped horizontal pipes as shown in Figure 6.2. The pipes are connected by two headers (upper and lower) marked by dashed white lines in Figure 6.2b,c. The lower header is connected with the steam inlets and provides the steam to the lower pipes. All pipes and both headers are slightly inclined towards the steam inlets (Figure 6.2a,b), so the resulting condensate is removed from the CH by the gravitational force back to the oven. The steam condenses inside the pipes while flowing through them. The water vapour that has not condensed leaves the pipes and flows into the steam exit (Figure 6.2b,c) being withdrawn by the fan. Then, the steam is mixed with the air in the fan (i.e., diluted) and finally transported out to the environment.

It is also worth noting that the fluid flowing inside the pipes close to the steam vents contains mainly steam. Then the condensation process starts, and the resulting liquid condensate has a much lower volume than the water vapour, which causes that pressure to drop. As a consequence of that process, from space surrounding the fan, some air is sucked and fluid inside the pipes becomes a steam-air mixture. The steam mass fraction in this mixture gradually decreases as the condensation process continues.

The airflow in the interpipe space (actually between U-shaped pipes) is shown schematically in Figure 6.2c by the green dashed line. Flow is directed utilising a baffle that divides the pipe space into two sections. Then, once the air reaches the heat exchanger's rear wall, it is turned by the flow guides and flows again perpendicularly to the pipes. The air leaves the heat exchanger through an outlet II.c marked in Figure 6.2c by white rectangle (landscape oriented).

6.2 Numerical model - setup and BCs

The sketch of the condensation hood's redesigned heat exchanger model is shown in Figure 6.3. The computational domain has been reduced to heat exchanger only, as

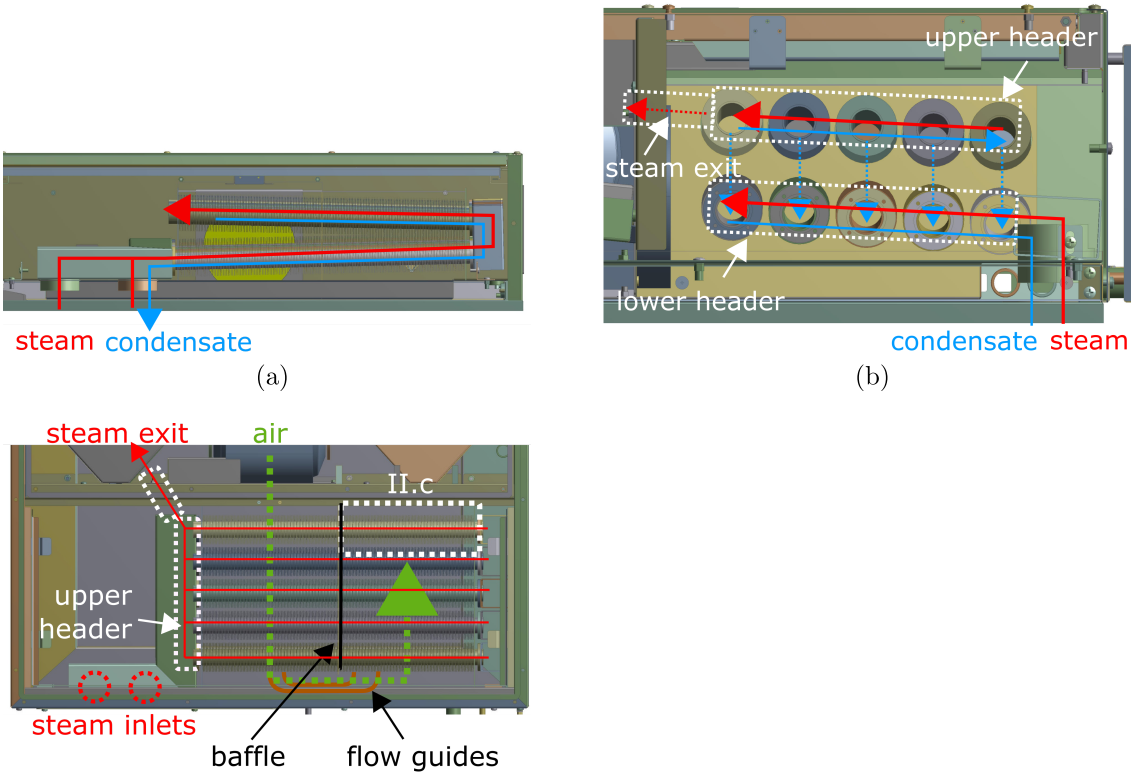

(a) (b) (c)

Figure 6.2: Redesigned heat exchanger: a) rear view; b) side view; c) top view. II.c - air vent. Figure adapted from images courtesy of Retech Ltd.

the rest of the device remains intact (no modifications) and has a limited impact on the model stability and convergence. It should be noted that the fan, steam vents, and air outlet location are the same as in the previous constructions (i.e., original and modified constructions) described above. They are all marked in Figure 6.3a,b together with the inlet and outlet conditions as well as paths and zones of the working fluids: 1 – air inlet implemented as a velocity profile (measured again for this new construction together with flow resistance) with the use of an UDF; 2 – air outlet implemented as a pressure outlet with porous zone simulating air filter; 3 – steam inlets (I.a) and (I.b) (steam is provided by combi-steamer); and 4 – steam exit (I.g) implemented as pressure outlet (negative gauge pressure controlled by the fan). The water traps (I.c) & (I.d); lower header (I.e), and upper header (I.f) are additionally indicated.

The air filter at the air outlet (2) was implemented as a porous zone. Pressure loss measurements of the real filter were conducted for air velocity varying from 1 to 4 m/s. Defining the porous zone in Ansys Fluent requires providing two coefficients for each of the flow directions: the proportionality coefficient and the inertial resistance factor. As the flow through the filter is one-dimensional, i.e., perpendicular to the filter, both coefficients were determined. The remaining components are set as 10^3 times larger. The first parameter was obtained by fitting the pressure loss as a function of velocity [4] was adopted.

$$\Delta p = 0.154\, v^2 \tag{6.1}$$

where Δp stands for the pressure loss, v is the air velocity, and the proportionality coefficient equal to 0.154 is the result of measurement processing.

The polynomial was slightly adjusted to keep positive pressure loss values near the minimal measurement range (velocity around 1 m/s). In the next step, the inertial resistance factor C_2 is calculated according to the Ansys Fluent User's Guide [4]

$$C_2 = \frac{2 \cdot 0.154}{\rho\, \Delta n} \tag{6.2}$$

where $\rho = 1.16$ stands for the air density, kg/m^3 and $\Delta n = 0.013$ is the thickness of the filter, m. Those dates give $C_2 = 20.44$ which is then introduced with the appropriate viscous resistance direction component.

The flow guides II.a and II.b consist of two plates bent on both sides to evenly distribute the air stream downstream so that it could interact with the largest possible

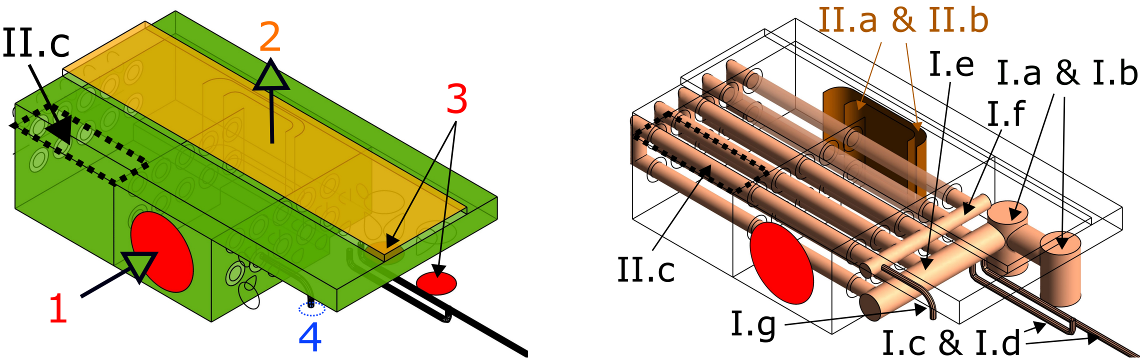

(a) (b)

Figure 6.3: Computational domain: a) air path/zone;b) steam path/zone. 1 - air inlet; 2 - air outlet; 3 - steam inlets; 4 - steam exit. I.a & I.b - steam vent; I.c & I.d - water trap; I.e - lower header; I.f - upper header; I.g - air/steam zone connector; II.a and II.b - flow guides; II.c - air vent.

surface of the pipes. Determination of the dimensions and number of metal sheets in the flow guide was carried out as maximising the area weighted uniformity index (UI) in Ansys Workbench using Design Exploration Response Surface Optimisation system. The uniformity index accounts for the stream distribution on a cross-section of a substrate and can take a value between 0 to 1 (value 0 means nonuniform flow, while value 1 stands for ideally uniform flow). Uniformity indices were calculated in two cross-sections presented in Figure 6.4.a and denoted as A and B. Both UIs were maximised to provide as uniform air flow downstream as possible throughout the HE. In Figure 6.4 four cases are visualised: without flow guides, with one flow guide, two, and three flow guides. Figure 6.4.a stands for the case without any flow guides - the air tends to flow along the external wall, in this case leaving the central part (marked by an ellipse) uncovered. Impact of a single flow guide is visible in Figure 6.4.b, where the flow uniformity downstream is slightly improved.

Exact values of the uniformity indices are gathered in Table 6.1. Data is arranged in two groups: Basic - UI values before optimisation of all four cases; Optimised - UI values after optimisation. As one can see, the basic average UI values range from 0.68 in the case without any flow guides (flow guides 0) to 0.74, when 3 flow guides were employed. All cases, where flow guides are present have a similar average UI value of ≈0.74. After optimisation, this difference is noticeable, as the average UI values spread from 0.74 to even 0.79. In the case of a single flow guide, optimisation brought practically no effect as the average UI remained at 0.74. In the case of the two flow guides, the average UI

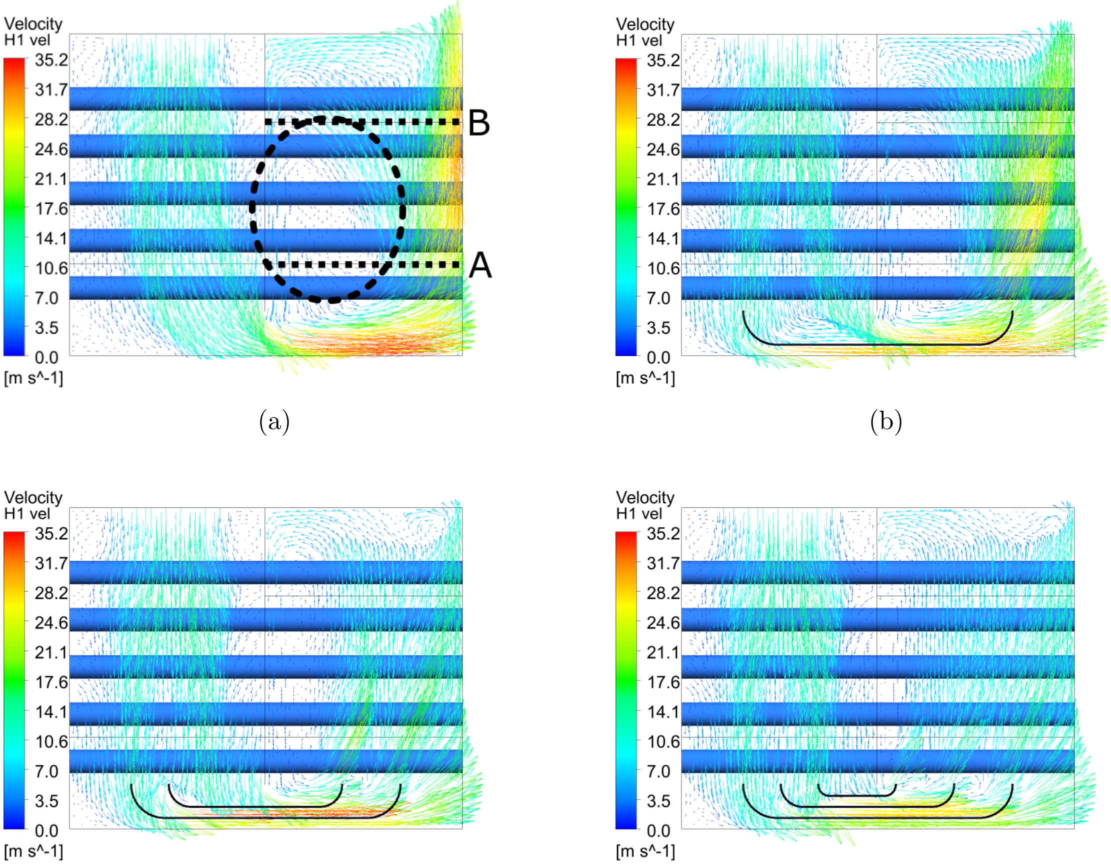

(a) (b)

(c) (d)

Figure 6.4: Flow guides: a) no flow guides; b) single flow guide; c) double flow guide; d) triple flow guide.

value increased from 0.73 to 0.76 (by 0.03), while in the case of the three flow guides, it increased from 0.74 to 0.79 (by 0.05). The presented optimisation results improve the air flow distribution in the inter-pipe space.

Table 6.1: Uniformity indices in A and B cross-sections: before (Basic) and after (Optimised) optimisation.

		Flow guides:			
	Cross-sections:	3	2	1	0
Basic	A	0.70	0.68	0.65	0.62
	B	0.78	0.78	0.82	0.73
	Average:	0.74	0.73	0.74	0.68
Optimised	A	0.77	0.71	0.68	
	B	0.81	0.80	0.80	
	Average:	0.79	0.76	0.74	

Satisfactory uniformity was achieved when two flow guides were employed, as indicated in Figure 6.4.c, where the uncovered pipe surface was reduced to ≈30% of the cross-sectional area. The best results were obtained with three flow guides implemented, as shown in Figure 6.4.d, but the installation of the third flow guide in the real device was hard due to the limited space, so in the end two flow guides were utilised.

Slopes of the pipes and headers are neglected to improve the mesh quality. Those elements' position is an average of the extreme positions of their sloped counterparts in the design project visualised in Figure 6.2. The decision to neglect the slopes also enabled the use of correlations for convective heat transfer for the in-line bundle configuration. Certainly, this approach introduces some minor underestimation regarding the heat transfer coefficients and condensation efficiency, which means the numerical results can be lower than the measured values.

The model was set up in a similar manner as the previous models, i.e., the analysis was in steady-state, k-ε turbulence model with standard wall function was used to solve the continuity equation. A SIMPLE scheme was used for pressure-velocity coupling, PRESTO! for pressure distretization, and second-order upwind was set for mommentum, turbulence, species, and energy discretization. Species transport model was enabled due to already developed condensation and condensate removal UDF allowing for simulating a single phase flow with a phase change.

6.2.1 Condensation model and heat transfer model

This in-house steady-state computational model reduces the number of analysed phases, i.e., only the gas-phase flow was modelled. Liquid condensate resulting from the phase change process was treated as a local mass sink, which closed the mass balance equation for water vapour. The condensation process's energy effect, i.e., latent heat, was also taken into account in the energy balance.

As it was already mentioned, the heat exchanger in the redesigned construction was equipped with five pipes divided into twenty externally-finned pipe sections. Each section is approximately 480 mm long, which results in approximately 3800 fins in total (0.3 mm fin thickness and 2.24 mm fin pitch). Good quality numerical mesh for such geometry would result in an enormous number of elements, which was unacceptable due to the limited computational time and computer memory at disposal. Consequently, it was decided that simulations of heat and mass transfer processes in the condensation hood heat exchanger should be carried out using a kind of hybrid solution (i.e., superposition of numerical and analytical solutions). In practice, this means that the fins have not been included in the computational domain of the air, so the use of a coarser mesh was allowed in the interfin space, called fin cell zone. The fin cell zone is described further in this section. The convective heat transfer within the interpipe space was solved numerically using a relatively coarse numerical mesh and Ansys-Fluent. Heat convection with the steam's condensation inside the pipe, then heat conduction through the pipe wall, and eventually the contribution of fins to the convective heat transfer within the interfin space, have been modelled analytically using formulae widely known from heat transfer theory. Both solutions are finally superpositioned within the interfin space in a way allowing to fulfil the energy balance on the external surface of the pipe. These steps of developing an analytical solution and superpositioning it with the numerical solution implemented utilising Fluent's UDF functionality requires an appropriate iterative loop.

The developed UDF's main components are presented schematically in Figure 6.5. Namely, five main steps can be distinguished: 1 – calculation of the heat transfer coefficients for steam and air inside the pipe as well as for the air in the interfin space; 2 – determination of the overall thermal resistances for steam and air; 3 – determination of a maximum heat rate for steam and for air; 4 – determination of an actual heat transfer rates for the steam and for the air; 5 – computation of the source terms.

As a consequence of the UDF implementation (no liquid water), the flow was reduced to a single-phase, which allowed for the employment of the species transport model. The flow consists of two components: the air treated as a single gas (not a mixture of N_2 and O_2) and steam. Moist air flows in the interpipe space, while the air-steam mixture inside the pipes. In the species transport model, the dominant species mass fraction (here: air) is not calculated from the mass balance equations but is determined as a remaining fraction to close the mass balance ($Y_{air} = 1 - Y_{H_2O}$). As a consequence, the only species transport equation solved by the Fluent concerns the water vapour and takes the form

$$\frac{\partial}{\partial t}(\rho Y_{H_2O}) + \nabla \cdot (\rho \overrightarrow{v} Y_{H_2O}) = -\nabla \cdot \overrightarrow{J}_{H_2O} + S_{H_2O} \tag{6.3}$$

where Y_{H_2O} is the water vapour species mass fraction, $\overrightarrow{J}_{H_2O}$ stands for a water vapour mass diffusion in turbulent flow, and S_{H_2O} denotes an additional negative water vapour source defined by the UDF (equal to a condensation source rate $\dot{m}_{cond,st}$), $\mathrm{kg}/(\mathrm{m}^3 \cdot \mathrm{s})$, defined in the following sections. The term concerning rate of creation due to chemical reactions in this work is equal to 0 and was not shown in the equation above.

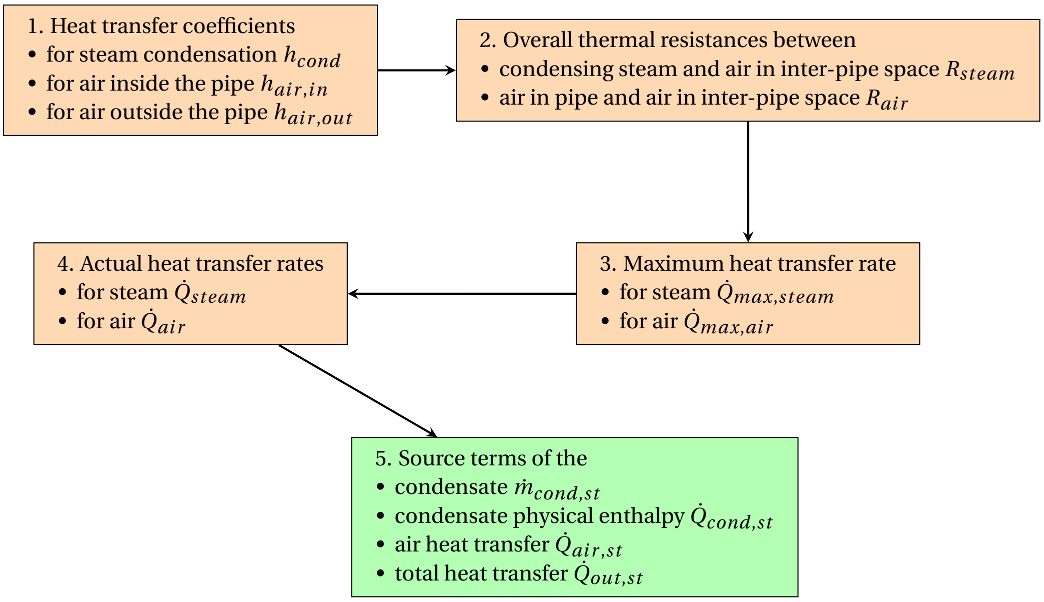

Figure 6.5: Schematic algorithm of the developed condensation and heat transfer model within developed UDF.

Detailed description of the species transport model, momentum, and energy equations can be found in the Ansys Fluent Theory Guide [5].

Numerical mesh within the interfin space was required to implement the UDF mentioned above, to identify the local parameters of the air at the selected cells, and then calculate the coefficients/quantities appearing in the analytical solution. We discuss this in more detail in the following subsection. Discretisation of the interfin space, called the fin cell zone, is schematically shown in Figure 6.6 – blue hollow cylinder having an external diameter identical as the diameter of the fins and an internal diameter equal to the external diameter of the pipe.

The CFD solution for the air within the interpipe space SIMPLE scheme was used as a pressure-velocity coupling. Discretisation schemes of pressure, turbulence, species, and energy were set as a second order upwind. Gradient discretisation was set as least squares cell based due to the mesh consisting of mainly hexahedral elements. The analysis was computed with gravitation enabled.

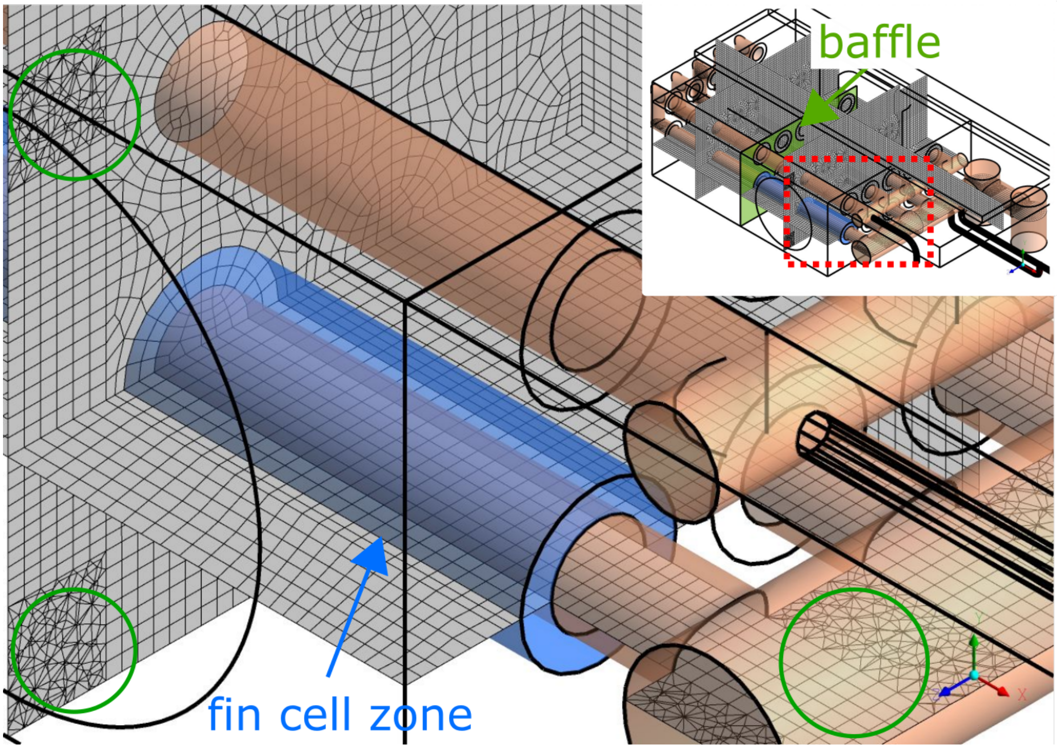

Figure 6.6: Fragment of the numerical mesh. View on the headers, pipe, and fin cell zone.

6.2.2 Heat Transfer Coefficients

To model a film condensation process inside a horizontal tube filled with steam, the following equation [9] for the heat transfer coefficient h_{cond} (in $\mathrm{W/(m^2 \cdot K)}$) was employed

$$h_{cond} = 0.555 \left[\frac{g\, \rho_{cond} \left(\rho_{cond} - \rho_{steam}\right) k_{cond}^3}{\mu_{cond}\, \left(T_{sat} - T_{pipe,wall}\right) d_{pipe}} \left(h_{fg} + \frac{3}{8}\, C_{p,cond}\, \left(T_{sat} - T_{pipe,wall}\right) \right) \right]^{1/4} \tag{6.4}$$

where g stands for gravitational acceleration, $\mathrm{m/s^2}$, ρ_{cond} and ρ_{steam} are densities of the condensate and the steam, respectively, $\mathrm{kg/m^3}$, k_{cond} denotes condensate's thermal conductivity, $\mathrm{W/(m \cdot K)}$, μ_{cond} is a viscosity of the condensate, $\mathrm{kg/(s \cdot m)}$, T_{sat} and $T_{pipe,wall}$ are steam saturation temperature and the average temperature of the pipe surface, respectively, K, h_{fg} is the heat of vapourisation of the fluid (water), J/kg, $C_{p,cond}$ denotes the specific heat of the condensate, $\mathrm{J/(kg \cdot K)}$, and d_{pipe} stands for internal pipe diameter, m.

Equation (6.4) refers to the steam. However, in the pipes, air residues, so another heat transfer coefficient for the air is needed. To calculate the relevant Nusselt number for a turbulent flow in a tube, the Colburn equation [9] was used

$$\mathrm{Nu}_{air,in} = 0.023\, \mathrm{Re}_{air,in}^{0.8}\, \mathrm{Pr}_{air,in}^{\frac{1}{3}} \tag{6.5}$$

where $\mathrm{Nu}_{air,in}$ stands for the Nusselt number, $\mathrm{Re}_{air,in}$ denotes the Reynolds number, and $\mathrm{Pr}_{air,in}$ is the Prandtl number. The air properties in the above mentioned dimensionless numbers are calculated at the average air temperature in the considered pipe section defined as

$$T_{air,in,av} = \frac{\left(T_{air,in,inlet} + T_{air,in,outlet}\right)}{2} \tag{6.6}$$

where $T_{air,in,inlet}$ and $T_{air,in,outlet}$ are the mass-weighted average temperatures of the air at the inlet and at the outlet of the pipe section, respectively, K. Finally, the convective heat transfer coefficient for the air inside the tube is derived using the Nusselt number $\mathrm{Nu}_{air,in}$

$$h_{air,in} = \frac{\mathrm{Nu}_{air,in}\ v_{air,in}}{d_{pipe}} \tag{6.7}$$

where $v_{air,in}$ is a mean air velocity in the pipe, m/s.

The Nusselt number for the finned side of the pipe is based on the correlations for cross flow over tube bundles [9]

$$\mathrm{Nu}_{air,out} = A\,\mathrm{Re}^{b}_{air,out}\,\mathrm{Pr}^{c}_{air,out}\left(\frac{\mathrm{Pr}_{air,out}}{\mathrm{Pr}_{pipe,wall}}\right)^{0.25} \tag{6.8}$$

where $\mathrm{Re}_{air,out}$ is the Reynolds number defined on the basis of maximum velocity that occurs in the pipe bundle (as the flow cross section area decreases due to existence of the pipes having external diameter D_{pipe}), $\mathrm{Pr}_{air,out}$ stands for the Prantdl number defined for the temperature $T_{bundle,av}$, while $\mathrm{Pr}_{pipe,wall}$ is the Prantdl number defined for the temperature $T_{pipe,wall,av}$. Symbols A, b and c denote correlation coefficients for the in-line bundle arrangement and they depend on the $\mathrm{Re}_{air,out}$ value.

The temperature $T_{bundle,av}$ is the arithmetic mean temperature of the fluid at the air inlet 1 (i.e., inlet to the bundle) and at the outlet II.c (see Figure 6.3) which constitutes the bundle outlet

$$T_{bundle,av} = \frac{T_{bundle,in,av} + T_{bundle,out,av}}{2} \tag{6.9}$$

where $T_{bundle,in,av}$ and $T_{bundle,out,av}$ stand for the mass-weighted temperatures of the fluid at the inlet and at the outlet of the bundle, respectively. For instance, the temperature $T_{bundle,in,av}$ is calculated according to the following equation

$$T_{bundle,in,av} = \frac{\sum \rho_{fin,cell,inlet}\, V_{fin,cell,inlet}\, T_{fin,cell,inlet}}{\sum \rho_{fin,cell,inlet}\, V_{fin,cell,inlet}} \tag{6.10}$$

where $\rho_{fin,cell,inlet}$ stands for the density of the fluid in a cell at the inlet/outlet, kg/m^3, $V_{fin,cell,inlet}$ is the volume of the considered cell, m^3, and $T_{fin,cell,inlet}$ denotes for the temperature of the fluid in the cell. All the quantities are provided by the Fluent macros C_R, C_V, and C_T, respectively. Summation is taken over all cells at the inlet and at the outlet surface of the heat exchanger presented in Figure 6.3 as: 1 – air inlet and II.c – air vent. Obviously, temperature $T_{bundle,out,av}$ is determined analogously.

Temperature $T_{pipe,wall,av}$ is calculated as the external pipe wall's arithmetic mean temperature.

$$T_{pipe,wall,av} = \frac{\sum T_{pipe,wall,face}}{\sum N_{pipe,wall,face}} \tag{6.11}$$

where $T_{pipe,wall,face}$ is the temperature of the face adjacent to the pipe wall, K, and $N_{pipe,wall,face}$ stands for the number of faces. The $T_{pipe,wall,face}$ is provided by the Fluent using the F_T macro. Summation is done over all cells at the given pipe wall.

Reynolds number for airflow in the interpipe space $\mathrm{Re}_{air,fin}$ is calculated as follows

$$\mathrm{Re}_{air,fin} = \frac{D_{pipe}\, v_{max}}{\nu} \tag{6.12}$$

where D_{pipe} stands for external pipe diameter, m, v_{max} denotes maximum fluid velocity in the bundle, m/s, and ν is the kinematic fluid viscosity defined at the temperature $T_{bundle,av}$, m^2/s. The heat transfer coefficient on this side $h_{air,out}$ is calculated separately for the each pipe section depending on the location inside the bundle by introduction of the correction factor F described in [9]

$$h_{air,out} = \frac{F\, \mathrm{Nu}_{air,out}\, k_{air,out}}{D_{pipe}} \tag{6.13}$$

where F is the correction factor, –, $k_{air,fin}$ is the fluid thermal conductivity defined in the $T_{bundle,av}$ temperature, $\mathrm{W/(m \cdot K)}$.

Before the thermal resistance can be computed, the external heat transfer coefficient $h_{air,out}$ needs to be modified to take into account the fins. Hence, a correction factor ε_h is calculated according to the following equation

$$\varepsilon_h = \frac{((L_{pipe} - N_{fin}\, \delta_{fin})\, \pi D_{pipe}) + \frac{1}{2}\, \pi\, N_{fin}\, \left((D_{pipe} + 2\, L_{fin})^2 - D_{pipe}^2\right) \eta_{fin}}{L_{pipe}\, \pi\, D_{pipe}} \tag{6.14}$$

where N_{fin} stands for the number of fins, δ_{fin} denotes a fin thickness, m, η_{fin} is a fin efficiency depending on the fin geometry and estimated at 0.95, –, and L_{fin} is a fin length, m.

6.2.3 Thermal Resistances

Once all heat transfer coefficients are determined, the overall thermal resistance can be computed. Because the air-steam mixture flows in the pipes, there are two overall thermal resistances R_{air} and R_{steam}, each one per appropriate mixture component.

$$\begin{aligned} R_{steam} &= R_{cond} + R_{pipe} + R_{air,out} = \frac{1}{\pi\, d_{pipe}\, h_{cond}} + \frac{\log\left(\frac{D_{pipe}}{d_{pipe}}\right)}{2\,\pi\, k_{pipe}} + \frac{1}{\pi\, D_{pipe}\, h_{air,out}\, \varepsilon_h} \\ R_{air} &= R_{air,in} + R_{pipe} + R_{air,out} = \frac{1}{\pi\, d_{pipe}\, h_{air,in}} + \frac{\log\left(\frac{D_{pipe}}{d_{pipe}}\right)}{2\,\pi\, k_{pipe}} + \frac{1}{\pi\, D_{pipe}\, h_{air,out}\, \varepsilon_h} \end{aligned} \tag{6.15}$$

where R_{steam} and R_{air} are overall thermal resistances of the mixture components, $(\mathrm{m} \cdot \mathrm{K})/\mathrm{W}$ and k_{pipe} denotes thermal conductivity of the pipe, $\mathrm{W}/(\mathrm{m} \cdot \mathrm{K})$. These resistances determine the maximal heat fluxes across the pipe wall for steam and air, respectively.

6.2.4 Maximal Heat Transfer Rate

The maximum available heat transfer rate for the air and steam in the considered section of the pipe $\dot{Q}_{max,component}$ equals to

$$\dot{Q}_{max,component} = \frac{T_{mixture,av} - T_{air,out,av}}{R_{component}}\, L_{pipe} \tag{6.16}$$

where $T_{mixture}$ stands for the average temperature of the mixture in the considered pipe section (calculated by the UDF), K, $T_{air,out}$ is an average temperature of the air in the fin cell zone of this pipe section (calculated by the UDF), K, $R_{component}$ is overall thermal resistance of the mixture component R_{air} and R_{steam} (Equation (6.15)), $(\mathrm{m} \cdot \mathrm{K})/\mathrm{W}$, and L_{pipe} is a length of the pipe section, m.

The temperature of the mixture $T_{mixture}$ is calculated based on cells adjacent to the pipe wall (inside the pipe)

$$T_{mixture,av} = \frac{\sum \rho_{pipe,cell,in}\, V_{pipe,cell,in}\, T_{pipe,cell,in}}{\sum \rho_{pipe,cell,in}\, V_{pipe,cell,in}} \tag{6.17}$$

where $\rho_{pipe,cell,in}$ stands for the density of the fluid in a cell adjacent to the pipe wall, $\mathrm{kg/m^3}$, $V_{pipe,cell,in}$ is a volume of the considered cell, $\mathrm{m^3}$, and $T_{pipe,cell,in}$ denotes the temperature of the fluid in the cell. All these quantities are provided by the Fluent macros C_R, C_V, and C_T, respectively. Summation is done over all cells at a given section of the pipe wall. The temperature $T_{air,out}$ is computed similarly as $T_{mixture}$; however, the fluid properties come from the cells in the proper fin cell zone.

6.2.5 Actual Heat Transfer Rates

As the maximum heat transfer rate of the components $\dot{Q}_{max,component}$ represents the excessive energy carried by the pure one-component fluid, it has to be weighted according to the mass fractions of the given components (steam and air) in the mixture

$$\dot{Q}_{component} = u_{component}\,\dot{Q}_{max,component} \tag{6.18}$$

where $\dot{Q}_{component}$ stands for heat rate of the component (i.e., steam or the air), W, while $u_{component}$ is a component mass fraction provided by the Fluent.

6.2.6 Source Terms

The computational model developed for the heat and mass transfer processes utilises four source terms: concerning the condensate, the mass source (actually mass sink) represents condensating water vapour and removing the resulting liquid from the computational domain; the heat source expressing the physical enthalpy of the condensate; and two heat source terms representing the heat transfer rates between the fluid on both sides of the pipe.

The mass sink term $\dot{m}_{cond,st}$, in kg/(s $\cdot$ m^3) accounts for the amount of steam which condensed within a given cell can be calculated from the following equation

$$\dot{m}_{cond,st} = -\frac{\dot{Q}_{steam}}{h^*_{fg}\,V_{cell}} \tag{6.19}$$

where h^*_{fg} stands for a modified latent heat of vaporisation (accounting for the condensate subcooling), J/kg, and V_{cell} denotes volume of the analysed numerical cell, m^3. The heat transfer rate $\dot{Q}_{steam}$ is obtained from Equation (6.18) while the modified latent heat of vaporisation h^*_{fg} is calculated as follows [9]

$$h^*_{fg} = h_{fg} + 0.68\,C_{p,l}\,\left(T_{sat} - T_{wall}\right) \tag{6.20}$$

where h_{fg} is the latent heat in a saturation temperature, J/(kg $\cdot$ K), $C_{p,l}$ denotes the specific heat of the liquid at the average film temperature, J/(kg $\cdot$ K), T_{sat} and T_{wall} stand for the saturation and wall temperatures, respectively, K.

Along with the mass sink $\dot{m}_{cond,st}$, an appropriate energy source term $\dot{Q}_{cond,st}$, in

W/m^3, needs to be introduced into the energy equation. It represents the physical enthalpy and change-phase enthalpy of the condensate which is removed from the computational domain

$$\dot{Q}_{cond,st} = \dot{m}_{cond,st}\Big[h_{fg} + C_{p,l}\ (T - T_{Ref})\Big] \tag{6.21}$$

where T is the fluid temperature in a cell, K, and T_{Ref} is a reference temperature, K.

The rate of heat transfer from the air in the pipe to the air in the interpipe space can be treated as a negative source term $\dot{Q}_{air,st}$, in W/m^3, and should be considered in the energy equation in the pipe

$$\dot{Q}_{air,st} = -\frac{\dot{Q}_{air}}{V_{cell}} \tag{6.22}$$

Analogous heat source $\dot{Q}_{out,st}$, in W/m^3, but representing the heat transfer rate from the steam-air mixture to the air in the fin cell zone can be determined from the following formula

$$\dot{Q}_{out,st} = \frac{\dot{Q}_{steam} + \dot{Q}_{air}}{V_{cell}} \tag{6.23}$$

6.2.7 Model Summary

The developed model constitutes an analytical approach of heat and mass transfer calculation implemented in the numerical model. As presented in Figure 6.5, five main steps can be distinguished during the computational process. At first, the heat transfer coefficients of the condensing steam inside the pipe, the air in the pipe, and the air outside the pipe are computed according to the Equations (6.4), (6.7), and (6.13), respectively. Next, the overall thermal resistances R_{steam} and R_{air} are calculated as in Equation (6.15). There are two resistances, because there are two species in the pipes – the steam and the air – which exchange the heat with the coolant air on the outside of the pipes. Once the thermal resistances are known, the maximal heat transfer rates $\dot{Q}_{max,component}$ of each species are computed as in the Equation (6.16), which is common for both species in the model. Equation (6.16) is suitable in the situation, when the mass fraction of the species equals to 1, which here is not true. Hence, the $\dot{Q}_{max,component}$ is mass fraction-weighted as shown in Equation (6.18) and actual heat transfer rates $\dot{Q}_{component}$ ($\dot{Q}_{steam}$ and $\dot{Q}_{air}$) are calculated. At the end, the source terms are derived. There are three source terms that work inside the pipe: $\dot{m}_{cond,st}$ which stands for the condensate mass flow rate (Equation (6.19)), $\dot{Q}_{cond,st}$ (Equation (6.21)) which constitutes a physical enthalpy of the removed condensate due to $\dot{m}_{cond,st}$, and $\dot{Q}_{air,st}$ from Equation (6.22) which is the heat transferred between the air inside and outside the pipe, but the source term is applied in the pipe. The last source term, $\dot{Q}_{out,st}$ stands for the overall heat that is received by the coolant air outside the pipe and here it is applied.

6.2.8 Mesh

The numerical mesh, with its discretisation presented in Figure 6.6, consists of 1.2 million elements, mainly hexahedral. The element's size is approximately 5 mm and built using the sweep meshing method. Nonsweepable regions meshed with tetrahedral elements are marked with green circles in Figure 6.6. Those regions are peripheral blocks tangent to a fan boundary condition. Additionally, some sections of the upper and lower header and U-shaped pipe sections are also meshed with tetrahedrons.

Mesh independence analysis showed that the condensate mass flow rate weakly depends on the mesh size, as shown in Table 6.2. An extremely high steam load of 11.49 g/s was used as a benchmark. Different meshes were tested, including more fine elements in the fin cell zone and in all cases the mesh density weakly impacted on the condensate flow rate. The final coarse mesh allows for relatively robust and accurate computations keeping the Y+ at 60–280: 60–80 at the pipe walls and over 200 at the flow guide. As a consequence, the *k*-ε turbulence model with standard wall functions could be employed.

Table 6.2: Mesh independence test.

		Mesh	
	Unit:	**1**	**2**
Number of elements	–	0.6×10^6	1.2×10^6
Steam mass flow rate	g/s	11.49	11.49
Condensate mass flow rate	g/s	8.76	8.77

6.3 Results

The condensation hood equipped with the redesigned heat exchanger was examined in the following two cases:

- A – laboratory conditions, steam provided by a 3.4 kW steam generator,
- B* – laboratory conditions, steam provided by a 15 kW steam generator.

Case A corresponds to a typical working condition, whereas case B constitutes an extremely high heat load that allows one to obtain a maximum possible condensation of the new heat exchanger. Normal working conditions (like in the case A) depend on the mode to which the combi-steamer was set. There are three main modes: convection–based on a hot air (low steam production), combi-steam–mixture of hot air and steam (high steam production), and a steam mode–consisting mainly of steam (high steam production). Both combi-steam and steam modes are comparable in regard of the steam production, which was estimated at 1.0–1.5 g/s and provides much more steam than the convection mode, which produces less than 0.23 g/s [42]. For this reason the case A was adjusted so a typical steam production could be maintained during the experiment. The relative humidity of the coolant air ranged from 30 to 40% and the temperature varied from 25°C to over 30°C, depending on day.

Comparing with the previous examined constructions (OC and MC), the RC was not tested on a combi steamer, which corresponds to case C due to difficulties related to this measurement and resulting from this limited reliability.

The condensation hood works in a semi steady-state interrupted by occasional combi-steamer openings to insert or withdraw food. Each opening of the tight combi-steamer door releases a significant amount of steam previously accumulated inside. The steam is sucked by the CH in a short period of time, which lasts a couple of seconds until the whole steam is sucked. Such a short deterioration of the coolant air parameters has a serious impact on the CH condensation capability. As a consequence, case B was proposed as a way to examine the maximum condensation capability of CH.

Results obtained from the experiment and from the numerical model are gathered in Table 6.3. Inlet quantities measured in the experiment were used as the boundary conditions prescribed in the model; hence their experimental and numerical values of the boundary conditions are the same. Numerical values at the outlet are very similar to their experimental counterparts. The most important parameter, condensate mass flow rate $\dot{m}_{cond}$ in both cases, is similar. In case A, the experimental condensate mass flow rate was 1.29 g/s, while the numerical prediction is 1.32 g/s. It should be stated that numerical model predicted condensation of almost the whole of the available steam. Because such a limiting situation does not provide reliable information on the model accuracy, it was decided to carry out the experiment for case B, where the steam's mass flow rate needed to be condensed was much higher. In this case, the steam flow rate was 5.55 g/s, which was almost four times higher than in typical working conditions. The experimental condensate flow rate's value was equal to 3.56 g/s while the same quantity simulated numerically was 3.67 g/s. These results correspond to 64.2% and 66.1% condensation efficiency η_{cond}, respectively. Both values are fairly close to each other. A similar situation applies to the remaining output or boundary quantities. Hence, it can be concluded that the model is accurate in terms of inlet-outlet values, with a tendency to overestimate the condensation performance slightly.

For the performance comparison of RC and OC, Table 6.3 also contains the experimental results obtained for the case A and B (27 kW steam generator). Please, notice that the RC was tested in case B* with lowered power from 27 kW to 15 kW, while OC in case B with original power of 27 kW. In other words: cases B and B* are not the same cases and concern different powers.

The redesigned heat exchanger is a cheaper and simpler alternative to the original construction. It should have, however, at least a comparable condensation potential. The condensate mass flow rates of the OC and RC are presented in Table 6.3. Maximal condensate mass flow rate of the OC has been measured as equal to 3.08 g/s [42] while for RC construction, this quantity is equal to 3.56 g/s, i.e., approx. 16% more. Condensation efficiency η_{cond} of the OC in a relatively demanding case B equals almost to 27%, while for the RC it increases to 66% (but for a lower steam flow rate $\dot{m}_{steam}$ - case B*).

It should still be considered that the number of pipes in the heat exchanger was reduced from 48 in the OC to just 5 in the RC. The externally finned pipes used in the RC already were premanufactured and are available at the market, which constitutes a significant cost reduction. However, the most problematic parts of the new construction were both headers (the issue of connecting them to the pipes while maintaining tightness).

In Figure 6.7, the most important cross-sections used for graphical presentation of

Table 6.3: Experimental and numerical results: RC – redesigned construction; OC – original construction; Exp – experimental values; CFD – numerical values.

		RC:				**OC:**	
Case:		**A**		**B***		**A**	**B**
	Unit:	**Exp:**	**CFD:**	**Exp:**	**CFD:**	**EXP:**	
p_{amb}	Pa	96470		101130			
φ_{in}	%	37.1	39.4	28.8	29.0		
t_{in}	°C	24.5	24.5	31.4	31.4		
$\dot{m}_{air,in}$	kg/s	0.2	0.2	0.2	0.2		
t_{out}	°C	41.7	40.0	75.2	76.1		
φ_{out}	%	14.4	16.4	7.7	3.5		
$\dot{m}_{steam}$	g/s	1.32	1.32	5.55	5.55	1.18	11.5
$\dot{m}_{cond}$	g/s	1.29	1.32	3.56	3.67	1.16	3.08
η_{cond}	%	97.9	100.0	64.2	66.1	98.1	26.8

the field quantities are presented. Cross-sections H1 and H2 are horizontal ones. The first one is located at the height of a lower row of the pipes in such a way that the pipes are crossed along their diameter. The latter one, similarly to H1, crosses the upper row of the pipes alongside diameter. There are two remaining cross-sections, V1 and V2, across both sections of the heat exchanger vertically – upstream and downstream the baffle in the middle of the pipes.

Figure 6.8, presenting the velocity magnitude, shows that the air velocity in the bundle reaches about 16 m/s, but between the pipes, row-wise, the velocity reduces to less than 4.6 m/s. However, it should be remembered that the configuration of the pipes in the geometrical model has been simplified by neglecting all slopes. Hence, the numerical results in terms of velocity field should be treated with some reserve and the model probably also slightly overestimates the heat fluxes. Velocity fields in both cases look similarly, except for the pipes in Figure 6.8.b, where the steam velocity inside the tube approaches 4.6 m/s. Air steam flow rate in case B was slightly higher than in case A, hence maximum velocity in Figure 6.8.b is also slightly higher.

The velocity profiles shown in Figure 6.9 are similar to the ones presented in Figure 6.8. In this case, the air still tends to flow between the pipes without a thorough flowing around them. As a result, row-wisely regions of low velocity (i.e., $\leqslant$2 m/s) are distributed between neighbouring pipes. However, these regions are not as dominant as in Figure 6.8c. The highest velocity is found right after the air vent (II.c).

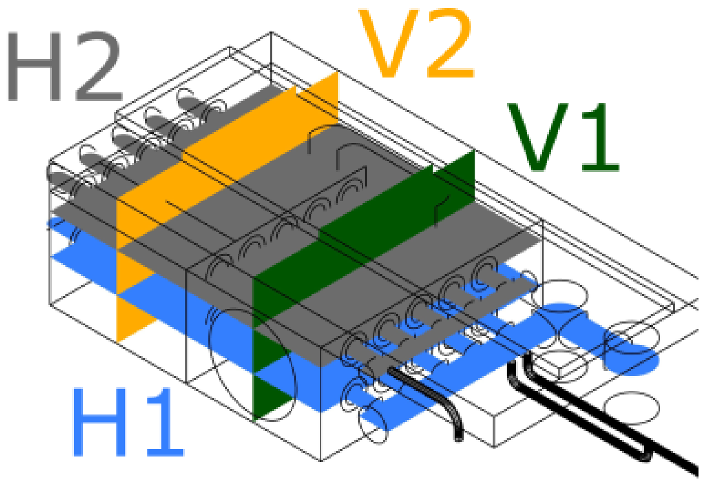

(a)

Figure 6.7: Model of the redesigned construction: cross-sections employed for presentation of the results.

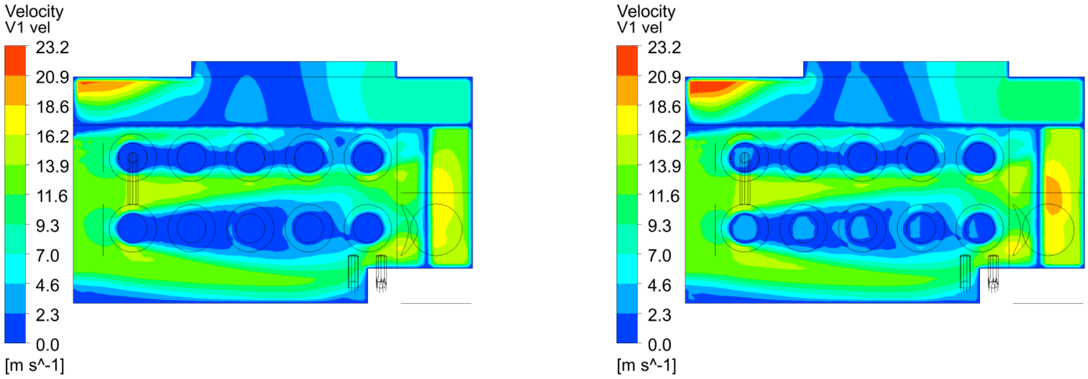

(a) (b)

Figure 6.8: Redesigned construction, velocity fields in plane V1: a) case A; b) case B.

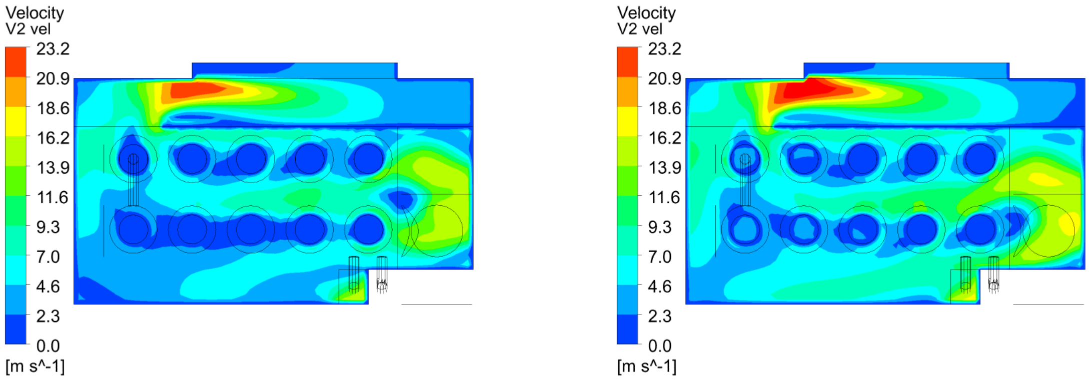

(a) (b)

Figure 6.9: Redesigned construction, velocity fields in plane V2: a) case A; b) case B.

Figure 6.10 presents the velocity magnitude in the H1 cross-section. In both cases, the highest velocity values are in the flow guide region, where the air has to squeeze between the flow guide sheets and radically changes its direction.

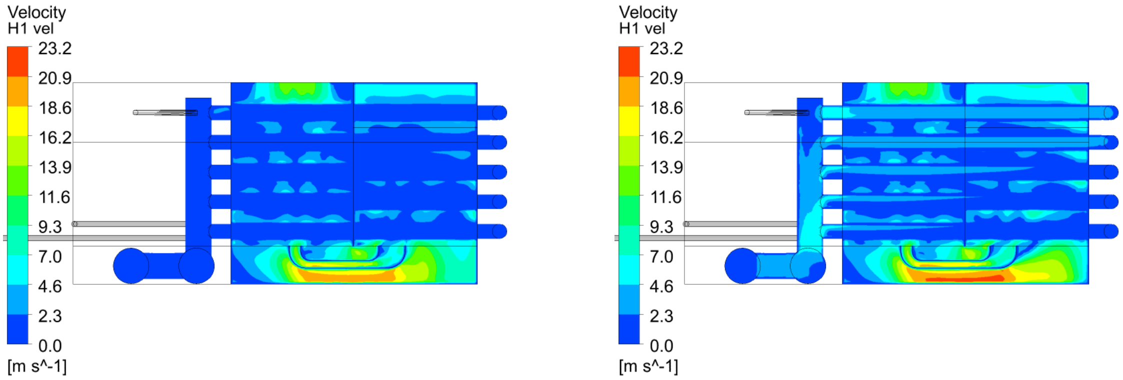

(a) (b)

Figure 6.10: Redesigned construction, velocity fields in plane H1: a) case A; b) case B.

Contour map of the velocity magnitude is presented in Figure 6.11. Velocities below 1 m/s generally occur inside the pipes in case A (Figure 6.11.a), while in case B (Figure 6.11.b) steam velocity does not excess 7 m/s. In both cases, the velocity fields on the air side are similar. The highest velocity of approximately 21 m/s can be observed in the flow guide region. As it can be noted, the uniformity of the velocity profile downstream the flow guide is not perfect but plausible. Hence, further improvements may include improvement of the flow guide shape and location.

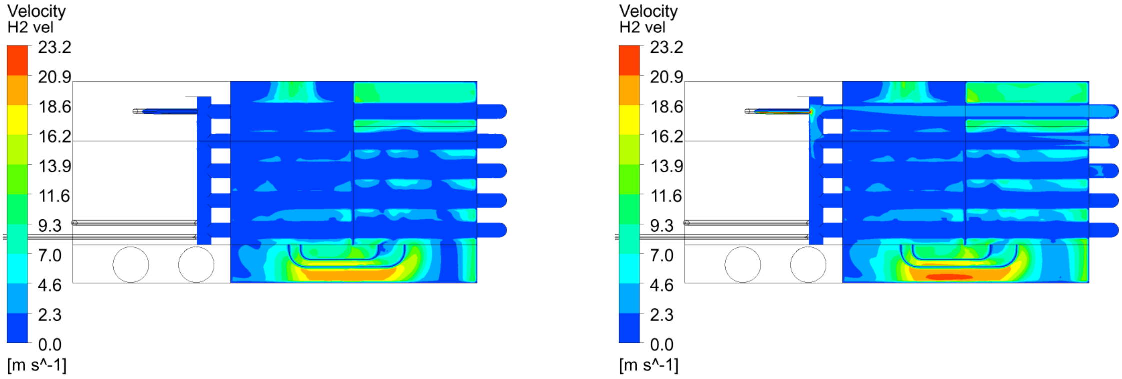

(a) (b)

Figure 6.11: Redesigned construction, velocity fields in plane H2: a) case A; b) case B.

Temperature distribution is presented in Figure 6.12. As expected, the air is heated up noticeably only around the lower pipes occupied by the steam in case A. Upper pipes in this cross-section practically do not participate in the heat transfer. In case B (Figure 6.12.b) however both pipe rows are releasing heat to the air that reaches ≈77°C at the outlet.

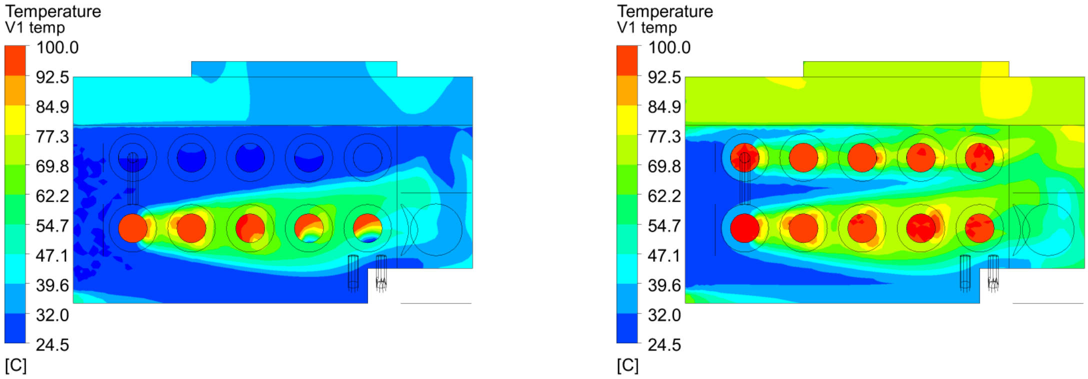

(a) (b)

Figure 6.12: Redesigned construction, temperature fields in plane V1: a) case A; b) case B.

Temperature distribution in plane V2 is presented in Figure 6.13 and in both cases is much more uniform than in the cross-section V1 in the Figure 6.12. The temperature in case A in the majority of the section is in the range 32–40 °C, while in case B in the range 62–92 °C. The highest temperature of approx. 92 °C can be observed right after the first (to the left) lower pipe—the one filled with steam. Next, the hot air flows upwards to near the upper pipe and then leaves the heat exchanger.

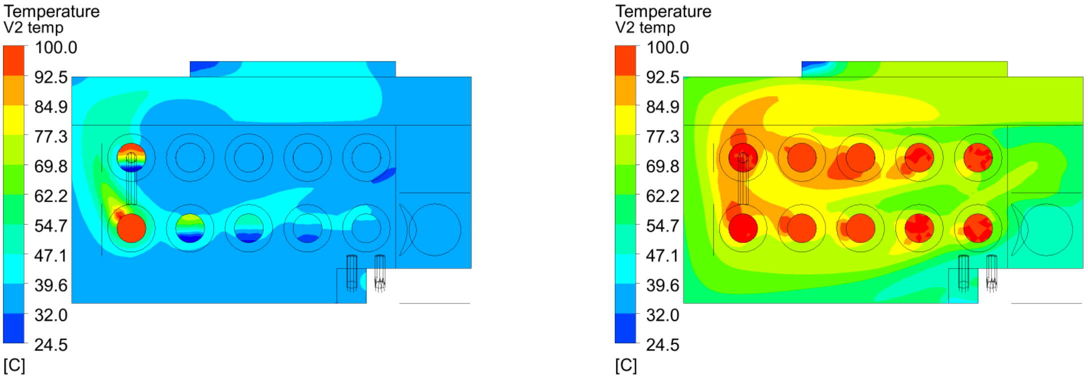

(a) (b)

Figure 6.13: Redesigned construction, temperature fields in plane V2: a) case A; b) case B*.

Temperature field RC model in H1 plane is presented in Figure 6.14. In case A, presented in Figure 6.14.a, a nonuniform heat load of the pipes is clearly visible. The majority of the steam flows through the pipe located farthest from the steam inlets. The steam flow rate is great enough that it flows through the whole lower section of this pipe. When considering other pipes, the situation is different. The steam reaches half the length of the lower last but one pipe and less than half of the remaining three pipes closer to the steam inlets. From this figures, the following statement can be formulated: the current design, despite having better condensation performance than the OC, can still be improved by driving the additional pressure drop and forcing more steam to go through the less loaded pipes, for instance, using pipes of different diameters or introducing orifices in the pipes. These options, however, were not tested yet. Temperature field in case B, shown in Figure 6.14.b, is quite different. Here, all pipes are filled with steam due to much greater steam flow rate. Temperature of the coolant air is also much higher in this case (around 60°C compared to ≈40°C in case A).

Figure 6.15 present temperature distribution in H2 cross-section. Relatively low temperature in the upper pipes (and low in their initial parts) in Figure 6.15.a indicates that there is still a lot of unused heat transfer surface during casual work, whereas Figure 6.15.b shows that, all upper pipes work almost equally as the steam mass flow rate is high enough to fill them all.

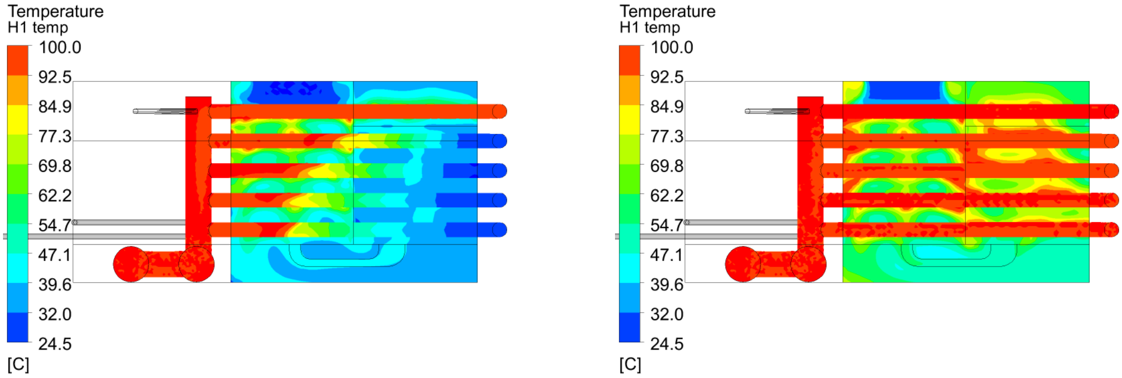

(a) (b)

Figure 6.14: Redesigned construction, temperature fields in plane H1: a) case A; b) case B*.

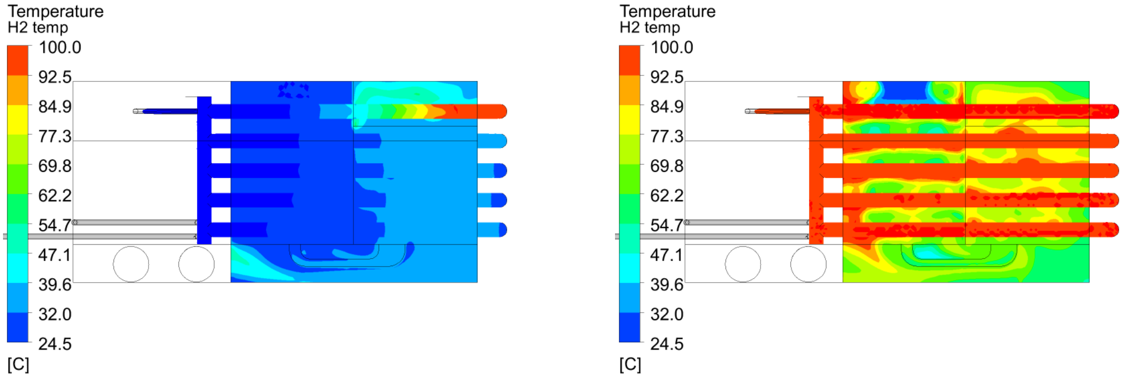

(a) (b)

Figure 6.15: Redesigned construction, temperature fields in plane H2: a) case A; b) case B*.

It should also be noted that to guarantee that the air mass flow rate flowing through the device, being forced by the same fan as in the earlier devices, the II.c vent (presented in Figure 6.3) in RC has been slightly enlarged, and the middle baffle was slightly shortened to weaken the resistance of the flow bottleneck.

In contrast to the original device, in the redesigned construction the steam flows and is condensed inside the pipes while the cooling air flows through the interpipe space. The pipes are externally finned with plain circular fins.

The basis of all these analyses is the steady-state computational model which accounts for the condensation and heat transfer processes taking place within the heat exchanger. The model has been built using Ansys-Fluent package and its UDF functionality. The UDF utilises the geometry of the fins and the appropriate mass and energy sources. Thanks to that approach, the analysis of complex two-phase flows with a phase change has been substantially simplified and only the gas phase could be modelled. The developed model used $k - \varepsilon$ turbulence model and accounted for the mass balance of air and water including liquid condensate.

6.4 Summary

As the original and modified condensation hoods employ internally finned pipes for steam condensation, according to the heat and mass transfer theory, there is a room for rapidly better use of the available space in the heat exchanger, when externally finned tubes are used. Led by the academic theory, a new construction of the condensation hood was designed numerically and then validated experimentally. However, the use of such pipes required to reorganise the air and steam flow, which resulted in an overhaul of the HE.

Redesigned (new) HE construction has one pipe bundle (instead of 2), the pipes are externally finned as the coolant air flows in the inter-pipe space, while steam flows and condenses inside the tubes. External fins significantly increased the overall heat transfer surface despite the fact that the number of pipes has been reduced from 48 (OC) or 36 (MC) to just 5. For better clarity, total pipe length can be compared. Thus, OC pipe length equals to 13.5 m, MC pipe length is 10.1, and RC pipe length coresponds to 4.7 m.

The RC numerical model covers steady-state analysis of a single phase flow with phase change, where (similarly to previous models) the condensate is removed by means of additional source terms implemented using UDF. Additionally, the whole heat transfer between steam and coolant air is done through the UDF.

Numerical results regarding the condensation capacity of the new design were optimistic and were confirmed by the measurements done later. The numerical model was validated in two laboratory cases: A emulating real working conditions and B that constitutes an extremely high heat load. In case B heater power was reduced from 30 kW (at this power OC and MC were tested) to 15 kW, which was sufficient to surpass the maximum condensation capacity of the RC and allowed for more stable measurements twice as long as the 30 kW case.

Chapter 7

Discussion and final conclusions

This PhD thesis covers the development of three numerical models of a condensation hood: the model of original construction (OC), which emulates already existing and produced devices; the model with HE modifications implemented - a modified construction (MC), which constitutes an improved design; and the model of a new construction (RC) with a redesigned heat exchanger. All models rely heavily on UDF, which is responsible for steam condensation and mass and heat transfer, to keep the models as simple and rapid as possible.

As this device was not investigated previously, nor experimental data was available, the operation principle of the condensation hood was unclear. Hence, a thorough experimental analysis was necessary.

Within this PhD thesis, over 50 measurement series were conducted with the use of a dedicated combi-steamer and steam generator in laboratory conditions. Each measurement lasted for 3 hours on average, which results in ≈150 hours of measurements. The measurements cover air mass flow rate, air temperature and relative humidity, steam temperature, steam mass flow rate, ambient temperature and relative humidity, and temperature distribution inside the heat exchanger. I participated in all measurements, part of them was performed solely by me.

Based on the experimental data, a mathematical model of the condensation hood was developed. The model is based on the mass, moisture, and energy balances of the CH. It allowed for measurement and CH work evaluation, the necessary quantities for numerical model validation also were derived and provided, i.e., outlet air temperature and relative humidity, and condensation efficiency.

As the experiments were time-consuming, when combined with limited time within the project, the numerical simulations needed to be robust, accurate, and doable with computational resources at disposal. For these reasons, practically the whole heat transfer in the conducted simulations is carried out via the UDF. It was a faster solution to develop the UDF instead of simulating two-phase flow with a phase change. The UDF has been designed in such a way to provide significant computing savings by limiting the flow to just one phase and by allowing for the geometrical simplification, i.e., to replace a fan with a moving rotor by a set of boundary conditions, and to replace the internally finned pipes in the HE by another set of boundary conditions. Such an approach was necessary, because additional analysis showed that, to properly simulate the air flow through a single pipe, over 1 million elements are required. While the heat exchanger is equipped with 48 of these pipes, it gives over 48 million elements to emulate the HE alone. Considering the available time and computational resources, it was impossible to fit in the project's time frame. Hence, the UDF has been developed that allows for mesh size reduction by approximately an order of magnitude. Another aspect complicating the development of the UDF is the lack of general heat and mass transfer formulas regarding the internally finned pipes. There are studies concerning this issue, but do not provide any wider applicable value above the strict cases covering the fin geometry and flows presented there.

Development of the UDF (condensation part) covers the mass and energy source terms for the air and steam, and a set of minor functions to read and calculate the necessary quantities known in the heat transfer theory. I co-developed the UDFs. The implementation of UDFs to the numerical models as well as validation was done by me. I was also responsible for the development of numerical models (geometry, mesh, boundary conditions, solver set-up).

As it was mentioned, three numerical models were created, each utilising the UDFs. OC model was used for diagnostic purposes to discover flaws of the original construction, which turned out to be the heat exchanger: ineffective internally finned pipes and highly nonuniform steam distribution on the heat transfer surface.

Then, a MC model was developed with the most promising improvements (proposed by me) to the HE implemented. In the next step, it was validated experimentally, when the prototype was ready. Modified construction has reduced the heat transfer surface area by 25% (total pipe length was reduced from 13.5 m to 10.1 m), which significantly reduces the manufacturing time and cost, and improved the steam distribution in the heat exchanger to compensate the lost heat transfer surface area. UDF in MC model was practically intact compared to OC.

Additionally, a redesigned construction (RC) was developed. In this case, both pipe bundles were merged into one, the flow of coolant air and steam was reorganised, so the use of externally finned pipes became possible (the new construction utilises 5 pipes of total length equal to 4.7 m). Once the prototype of RC was built, the model was validated as well. In this model, I adjusted the UDF to fit in a completely new geometry and boundary conditions and implemented it to the model.

All three numerical models (OC, MC, and RC) were validated: OC model was walidated with original CH; MC and RC models were validated with a two prototypes that were tested experimentally and are compared in Table 7.1. Only crucial parameters are taken into account: condensation efficiency η_{cond} and condensate mass flow rate $\dot{m}_{cond}$. Additionally, a $\dot{m}_{cond}$ difference in relation to the OC is reported.

Table 7.1: Condensation comparison of all constructions. OC - original construction; MC - modified construction; RC - new construction. Experimental velues only.

Case	Quantity:	Unit:	OC	MC	RC
A	η_{cond}	%	98.1	88.0	97.9
	$\dot{m}_{cond}$	kg/s	1.16	1.14	1.29
	Difference:	%	0	**-1.8**	**11.4**
B	η_{cond}	%	26.8	21.0	31.0
	$\dot{m}_{cond}$	kg/s	3.08	2.41	3.56
	Difference:	%	0	**-21.9**	**15.5**

As all constructions were tested in similar laboratory conditions (case A and B), they can be compared directly. In case A, which stands for an emulation of normal working conditions, MC has the lowest condensation efficiency, which results in less than negative 2% difference regarding the OC. Such a small difference close to 0 is a good indicator that the modified construction is not worse than the original one, despite having 25% less heat transfer surface area. Redesigned construction, however, has $\dot{m}_{cond}$ 11% higher than the OC, which confirms that the externally finned pipes are much more effective.

Extremely high steam load in case B was utilised to examine the maximal condensation capacity of all constructions. Moreover, here the OC condensation capacity was taken as a reference. In this case the MC did not as well as in case A, this however was expected, as the heat transfer surface was significantly limited. Although, the condensation hood will never work with such extremal heat loads, so 22% lower maximum condensation capacity is in this case acceptable.

The situation is different in the case of new construction RC, where the maximal condensation capacity is over 15% higher than the OC's. This result proves the RC design already is noticeably better than the original condensation hood and still has room for improvement, as the steam and air distributions still can be enhanced.

As a result of this work, two concepts of new condensation hoods inspired by the redesigned construction RC have been developed and implemented by Retech company and now are in production: one concept covers the further improved idea of U-shaped externally finned pipes from RC, while the other utilises a completely different configuration of such pipes.

7.1 Possible future reserach

The company already adopted part of the solutions designed during this PhD thesis, but there is another benefit of the performed work: the UDF condensation model. This model has a potential for generalisation thanks to which it could be implemented in any other numerical model concerning a phase change. It can be any gas condensing in any application (only a matter of adjusting material properties and phase change temperature/pressure) - the CFD model most likely will base on similar kind of boundary conditions. In practise, the condensate covers the heat transfer surface reducing the overall heat transfer coefficient. If there is a significant amount of condensing steam, the condensate removal (done via UDF) might introduce a noticeable overestimation of the heat transfer rate, resulting in serious accuracy loss. This is why this approach applies only when low intensity film condensation is involved. Nevertheless, in any case where the approach is applicable, the benefits from the implementation of this UDF model will be the same: significant mesh size reduction by lowering the computational cost; and enhancing CFD model convergence and stability by sticking to a single phase flow without condensate modelling.

Ultimately, this PhD provided not only set of solutions adopted by the industrial partner, but also a versatile tool for better solving complex multi phase problems.

Bibliography

[1] Afshin Ahmadi Nadooshan, Rasool Kalbasi, and Masoud Afrand. Perforated fins effect on the heat transfer rate from a circular tube by using wind tunnel: An experimental view. *Heat and Mass Transfer/Waerme- und Stoffuebertragung*, 54(10):3047–3057, 10 2018. `doi:10.1007/s00231-018-2333-3`.

[2] Amir Hesam Alinia Kashani, Alireza Maddahi, and Hassan Hajabdollahi. Thermal-economic optimization of an air-cooled heat exchanger unit. *Applied Thermal Engineering*, 54(1):43–55, 5 2013. URL: `https://www.sciencedirect.com/science/article/pii/S1359431113000446`, `doi:10.1016/J.APPLTHERMALENG.2013.01.014`.

[3] Refrigerating American Society of Heating and Air-Conditioning Engineers. *2001 ASHRAE Handbook - Fundamentals.* ASHRAE, Atlanta GA., s.i. ed. edition, 2001. URL: `http://www.worldcat.org/title/2001-ashrae-handbook-fundamentals/oclc/895979260`.

[4] Ansys Inc. *Ansys® Academic Research CFD, Release 14.0, Help System, Fluent User's Guide.* 2011.

[5] Ansys Inc. *Ansys® Academic Research CFD, Release 15.0, Help System, Fluent Theory Guide.* 2013.

[6] You Ma Bang, Seung Ryong Park, Chong Pyo Cho, Minjeong Cho, and Sungwook Park. Thermal and flow characteristics of a cylindrical superheater with circular fins. *Applied Thermal Engineering*, 181, 11 2020. `doi:10.1016/j.applthermaleng.2020.115895`.

[7] Arafat A. Bhuiyan and A. K.M.Sadrul Islam. Thermal and hydraulic performance of finned-tube heat exchangers under different flow ranges: A review on modeling and experiment, 10 2016. `doi:10.1016/j.ijheatmasstransfer.2016.05.022`.

[8] Haozhi Bian, Zhongning Sun, Xiang Cheng, Nan Zhang, Zhaoming Meng, and Ming Ding. CFD evaluations on bundle effects for steam condensation in the presence of air under natural convection conditions. *International Communications in Heat and Mass Transfer*, 98:200–208, 11 2018. URL: `https://www.sciencedirect.com/science/article/pii/S0735193318302227`, `doi:10.1016/J.ICHEATMASSTRANSFER.2018.09.003`.

[9] Yunus A. Çengel. *Heat Transfer: A practical approach.* McGraw-Hill Series in Mechanical Engineering, Boston [etc.], 3rd edition, 2007.

[10] A. Dehbi, F. Janasz, and B. Bell. Prediction of steam condensation in the presence of noncondensable gases using a CFD-based approach. *Nuclear Engineering and Design*, 258:199–210, 5 2013. URL: `https://www.sciencedirect.com/science/article/pii/S002954931300040X`, `doi:10.1016/J.NUCENGDES.2013.02.002`.

[11] Xuebo Dong, Wei Chen, Qian Cheng, Yi Liu, and Hao Dai. Numerical analysis of thermal-hydraulic characteristics of steam-air condensation in vertical sinusoidal corrugated tubes. *International Journal of Heat and Mass Transfer*, 164, 1 2021. `doi:10.1016/j.ijheatmasstransfer.2020.120558`.

[12] Carlos A. Dorao and Maria Fernandino. Simple and general correlation for heat transfer during flow condensation inside plain pipes. *International Journal of Heat and Mass Transfer*, 122:290–305, 7 2018. `doi:10.1016/j.ijheatmasstransfer.2018.01.097`.

[13] A. El Mansouri, M. Hasnaoui, A. Amahmid, and Y. Dahani. Transient theoretical model for the assessment of three heat exchanger designs in a large-scale salt gradient solar pond: Energy and exergy analysis. *Energy Conversion and Management*, 167:45–62, 7 2018. URL: `https://www.sciencedirect.com/science/article/pii/S0196890418304357`, `doi:10.1016/J.ENCONMAN.2018.04.087`.

[14] Guangming Fan, Pan Tong, Zhongning Sun, and Yitung Chen. Development of a new empirical correlation for steam condensation rates in the presence of air outside vertical smooth tube. *Annals of Nuclear Energy*, 113:139–146, 3 2018. URL: `https://www.sciencedirect.com/science/article/pii/S0306454916311252`, `doi:10.1016/J.ANUCENE.2017.11.021`.

[15] Guangming Fan, Pan Tong, Zhongning Sun, and Yitung Chen. Experimental study of pure steam and steam–air condensation over a vertical corrugated

tube. *Progress in Nuclear Energy*, 109:239–249, 11 2018. URL: `https://www.sciencedirect.com/science/article/pii/S0149197018302178`, `doi:10.1016/J.PNUCENE.2018.08.020`.

[16] Shiquan He, Xiaoqing Zhou, Feng Li, Huijun Wu, Qiliang Chen, and Zhiwei Lan. Heat and mass transfer performance of wet air flowing around circular and elliptic tube in plate fin heat exchangers for air cooling. *Heat and Mass Transfer/Waerme- und Stoffuebertragung*, 55(12):3661–3673, 12 2019. `doi:10.1007/s00231-019-02683-1`.

[17] Henny Penny Corp. Combi cooking. 2007.

[18] Kamran Hirbodi and Mahmood Yaghoubi. Flow structure of natural dehumidification over a horizontal finned-tube. *Heat and Mass Transfer/Waerme- und Stoffuebertragung*, 52(8):1455–1468, 8 2016. `doi:10.1007/s00231-015-1659-3`.

[19] Mafizul Huq, A.M. Aziz-ul Huq, and Muhammad Mustafizur Rahman. Experimental measurements of heat transfer in an internally finned tube. *International Communications in Heat and Mass Transfer*, 25(5):619–630, 7 1998. URL: `https://www.sciencedirect.com/science/article/pii/S0735193398000499`, `doi:10.1016/S0735-1933(98)00049-9`.

[20] Ian J. Kennedy, Stephen W.T. Spence, Gordon R. Spratt, and Juliana M. Early. Investigation of heat exchanger inclination in forced-draught air-cooled heat exchangers. *Applied Thermal Engineering*, 54(2):413–421, 5 2013. URL: `https://www.sciencedirect.com/science/article/pii/S135943111300118X`, `doi:10.1016/J.APPLTHERMALENG.2013.02.013`.

[21] Dong-Kwon Kim. Thermal optimization of internally finned tube with variable fin thickness. *Applied Thermal Engineering*, 102:1250–1261, 6 2016. URL: `https://www.sciencedirect.com/science/article/pii/S1359431116305464`, `doi:10.1016/J.APPLTHERMALENG.2016.04.060`.

[22] Diane Lane. ONE FOR ALL. *Caterer & Hotelkeeper*, 203(4799):56 – 58, 2013. URL: `http://search.ebscohost.com/login.aspx?direct=true&db=bth&AN=91707436&lang=pl&site=ehost-live`.

[23] B.E. Launder and D.B. Spalding. The numerical computation of turbulent flows. *Computer Methods in Applied Mechanics and Engineering*, 3(2):269–

289, 3 1974. URL: `https://www.sciencedirect.com/science/article/pii/0045782574900292`, `doi:10.1016/0045-7825(74)90029-2`.

[24] Dong H. Lee, Jin M. Jung, Jong H. Ha, and Young I. Cho. Improvement of heat transfer with perforated circular holes in finned tubes of air-cooled heat exchanger. *International Communications in Heat and Mass Transfer*, 39(2):161–166, 2 2012. URL: `https://www.sciencedirect.com/science/article/pii/S0735193311002533`, `doi:10.1016/J.ICHEATMASSTRANSFER.2011.11.009`.

[25] Karl Lindqvist and Erling Næss. A validated CFD model of plain and serrated fin-tube bundles. *Applied Thermal Engineering*, 143:72–79, 10 2018. `doi:10.1016/j.applthermaleng.2018.07.060`.

[26] P. Liu, R. Kandasamy, J. Y. Ho, and T. N. Wong. An experimental investigation on the effects of air on filmwise condensation of PF-5060 dielectric fluid on plain and finned tube bundles. *International Journal of Heat and Mass Transfer*, 162, 12 2020. `doi:10.1016/j.ijheatmasstransfer.2020.120349`.

[27] Youwei Long, Shugang Wang, Jihong Wang, and Tengfei Zhang. Mathematical Model of Heat Transfer for a Finned Tube Cross-flow Heat Exchanger with Ice Slurry as Cooling Medium. *Procedia Engineering*, 146:513–522, 1 2016. URL: `https://www.sciencedirect.com/science/article/pii/S1877705816308414`, `doi:10.1016/J.PROENG.2016.06.386`.

[28] X.F. Loyseau, P.G. Verdin, and L.D. Brown. Scale-up and turbulence modelling in pipes. *Journal of Petroleum Science and Engineering*, 162:1–11, 3 2018. URL: `https://www.sciencedirect.com/science/article/pii/S0920410517309750`, `doi:10.1016/J.PETROL.2017.12.019`.

[29] Kailash Mohapatra and Dipti Prasad Mishra. Effect of fin and tube configuration on heat transfer of an internally finned tube. *International Journal of Numerical Methods for Heat and Fluid Flow*, 2015. `doi:10.1108/HFF-05-2014-0129`.

[30] Mi Sandar Mon and Ulrich Gross. Numerical study of fin-spacing effects in annular-finned tube heat exchangers. *International Journal of Heat and Mass Transfer*, 47(8-9):1953–1964, 2004. `doi:10.1016/j.ijheatmasstransfer.2003.09.034`.

[31] S.M.A. Noori Rahim Abadi, M. Mehrabi, and Josua P. Meyer. Numerical study of steam condensation inside a long, inclined, smooth tube at different saturation temperatures. *International Journal of Heat and Mass Transfer*, 126:15–25, 11 2018. URL: `https://www.sciencedirect.com/science/article/pii/S0017931017353723`, `doi:10.1016/J.IJHEATMASSTRANSFER.2018.05.136`.

[32] Alan O'Donovan and Ronan Grimes. Pressure drop analysis of steam condensation in air-cooled circular tube bundles. *Applied Thermal Engineering*, 87:106–116, 8 2015. URL: `https://www.sciencedirect.com/science/article/pii/S1359431115004329`, `doi:10.1016/J.APPLTHERMALENG.2015.04.072`.

[33] Francisco Payri, Pablo Olmeda, Jaime Martín, and Ricardo Carreño. Experimental analysis of the global energy balance in a DI diesel engine. *Applied Thermal Engineering*, 89:545–557, 10 2015. URL: `https://www.sciencedirect.com/science/article/pii/S135943111500558X`, `doi:10.1016/J.APPLTHERMALENG.2015.06.005`.

[34] Hao Peng, Lin Liu, Xiang Ling, and Yang Li. Thermo-hydraulic performances of internally finned tube with a new type wave fin arrays. *Applied Thermal Engineering*, 98:1174–1188, 4 2016. URL: `https://www.sciencedirect.com/science/article/pii/S1359431116000065`, `doi:10.1016/J.APPLTHERMALENG.2015.12.115`.

[35] Parinya Pongsoi, Santi Pikulkajorn, Chi Chuan Wang, and Somchai Wongwises. Effect of number of tube rows on the air-side performance of crimped spiral fin-and-tube heat exchanger with a multipass parallel and counter cross-flow configuration. *International Journal of Heat and Mass Transfer*, 55(4):1403–1411, 1 2012. `doi:10.1016/j.ijheatmasstransfer.2011.09.064`.

[36] Bastian E. Rapp. *Chapter 29 - Computational Fluid Dynamics.* Elsevier, Oxford, 2017. URL: `https://www.sciencedirect.com/science/article/pii/B9781455731411500290`, `doi:10.1016/B978-1-4557-3141-1.50029-0`.

[37] P. Senthilkumar, S. Rajesh Babu, B. Koodalingam, and T. Dharmaprabhakaran. Design and thermal analysis on circular fin. In *Materials Today: Proceedings*, volume 33, pages 2901–2906. Elsevier Ltd, 2019. `doi:10.1016/j.matpr.2020.02.784`.

[38] Jiqiang Su, Zhongning Sun, and Dongyang Zhang. Numerical analysis of steam condensation over a vertical surface in presence of air. *Annals of Nuclear Energy*, 72:268–276, 10 2014. URL: `https://www.sciencedirect.com/science/article/pii/S0306454914002333`, `doi:10.1016/J.ANUCENE.2014.05.019`.

[39] D. Taler. Model matematyczny oraz badania aerodynamiczne i przepływowo-cieplne chłodnicy samochodowej. *Archiwum Motoryzacji*, Nr 4:145–162, 2001. URL: `http://yadda.icm.edu.pl/baztech/element/bwmeta1.element.baztech-article-BGPK-2121-8166`.

[40] G. I. Tarasov, M. A. Bol'shukhin, A. N. Sinitsyn, A. G. Vasyatkin, and S. V. Kustov. Experimental studies of heat transfer during steam condensation on a vertical multirow on-line bundle of slightly inclined coil tubes with and without noncondensable gas in the bundle. *Thermal Engineering*, 59(1):26–32, 1 2012. URL: `http://link.springer.com/10.1134/S0040601512010120`, `doi:10.1134/S0040601512010120`.

[41] Liting Tian, Yaling He, Yubing Tao, and Wenquan Tao. A comparative study on the air-side performance of wavy fin-and-tube heat exchanger with punched delta winglets in staggered and in-line arrangements. *International Journal of Thermal Sciences*, 48(9):1765–1776, 9 2009. URL: `https://www.sciencedirect.com/science/article/pii/S1290072909000234`, `doi:10.1016/J.IJTHERMALSCI.2009.02.007`.

[42] Mieszko Tokarski, Arkadiusz Ryfa, Piotr Buliński, Marek Rojczyk, Krzysztof Ziarko, and Andrzej J Nowak. Mathematical model and measurements of a combi-steamer condensation hood. *Archives of Thermodynamics*, 41(1):125–149, 2020. `doi:10.24425/ather.2020.132952`.

[43] Mieszko Tokarski, Arkadiusz Ryfa, Piotr Buliński, Marek Rojczyk, Krzysztof Ziarko, Ziemowit Ostrowski, and Andrzej J. Nowak. Development of a Condensation Model and a New Design of a Condensation Hood—Numerical and Experimental Study. *Energies*, 14(5):1344, 3 2021. URL: `https://www.mdpi.com/1996-1073/14/5/1344`, `doi:10.3390/en14051344`.

[44] Mieszko Tokarski, Arkadiusz Ryfa, Piotr Bulinski, Marek Rojczyk, Krzysztof Ziarko, Ziemowit Ostrowski, and Andrzej J. Nowak. Experimental analysis and

development of an in-house CFD condensation hood model. *Heat and Mass Transfer*, 7 2021. `doi:10.1007/s00231-021-03109-7`.

[45] Sebastian Unger, Eckhard Krepper, Matthias Beyer, and Uwe Hampel. Numerical optimization of a finned tube bundle heat exchanger arrangement for passive spent fuel pool cooling to ambient air. *Nuclear Engineering and Design*, 361, 5 2020. `doi:10.1016/j.nucengdes.2020.110549`.

[46] Ladislav Vyskocil, Josef Schmid, and Jiri Macek. CFD simulation of air–steam flow with condensation. *Nuclear Engineering and Design*, 279:147–157, 11 2014. URL: `https://www.sciencedirect.com/science/article/pii/S0029549314001034`, `doi:10.1016/J.NUCENGDES.2014.02.014`.

[47] Piotr Wais. Fluid flow consideration in fin-tube heat exchanger optimization. *Archives of Thermodynamics*, 2010. `doi:10.2478/v10173-010-0016-7`.

[48] Qiu-Wang Wang, Mei Lin, and Min Zeng. Effect of lateral fin profiles on turbulent flow and heat transfer performance of internally finned tubes. *Applied Thermal Engineering*, 29(14-15):3006–3013, 10 2009. URL: `https://www.sciencedirect.com/science/article/pii/S1359431109000982`, `doi:10.1016/J.APPLTHERMALENG.2009.03.016`.

[49] Xianmao Wang, Huajian Chang, and Michael Corradini. A CFD study of wave influence on film steam condensation in the presence of non-condensable gas. *Nuclear Engineering and Design*, 305:303–313, 8 2016. `doi:10.1016/j.nucengdes.2016.06.003`.

[50] Yungang Wang, Qinxin Zhao, Qulan Zhou, Zijin Kang, and Wenquan Tao. Experimental and numerical studies on actual flue gas condensation heat transfer in a left–right symmetric internally finned tube. *International Journal of Heat and Mass Transfer*, 64:10–20, 9 2013. URL: `https://www.sciencedirect.com/science/article/pii/S001793101300210X`, `doi:10.1016/J.IJHEATMASSTRANSFER.2013.03.005`.

[51] Dalin Zhang, Jiangtao Yu, Wenxi Tian, G. H. Su, and Suizheng Qiu. Heat transfer characteristics in super-low finned-tube bundles of moisture separator reheaters. *Nuclear Engineering and Design*, 341:368–376, 1 2019. `doi:10.1016/j.nucengdes.2018.11.018`.

[52] Qi Zhang, Henan Yi, Zaihai Yu, Jintong Gao, Xiaozhuang Wang, Heyong Lin, and Bo Shen. Energy-exergy analysis and energy efficiency improvement of coal-fired industrial boilers based on thermal test data. *Applied Thermal Engineering*, 144:614–627, 11 2018. URL: `https://www.sciencedirect.com/science/article/pii/S1359431118310196`, `doi:10.1016/J.APPLTHERMALENG.2018.08.069`.

Appendix A

UDF - OC/MC Source terms and heat transfer model

```
#include "udf.h"

real temp_vect[48]; //pipe temperature increase vector
DEFINE_EXECUTE_AT_END(zrodla_koniec)
{
face_t f;
cell_t c;
Domain *d;
Thread *th1;
Thread *thread1;
Thread *thread2;
Thread *t1;
Thread *thre1;
Thread *thre2;
int nfaces1=0;
int nfaces2=0;
int nfaces3=0;
int sum_nfaces=0;
real flow=0;
real moc=0;
real temperature=0;
real cp=1005;
real temp=0.0;
real poprawka_t=1.0;
real poprawka_s=1.0;
real deltaT=0.0;
```

```
real cieplo=0.0;
real temperatura; //condensation temperature
real cudmi=0.0;
real alpha_konw;
real alpha_kond;
real lambda;
real delta;
real pole_p;
real strumien;
real strumien_calk=0.0;
real strumien_posredni=0.0;
real temperatura_pary;
real temperatura_pow;
real docudmi=0.0;
real cisnienie_ot=0.987;  //ambient pressure, bar
real cisnienie_pary;  //steam saturation pressure, bar
real den_vol;      //product of density and volume
real den_vol_temp;     //product of density, volume, and temperature
real den_vol_sum=0.0; //sum of products
real den_vol_temp_sum=0.0;  //sum of products
d=Get_Domain(1);
thread1= Lookup_Thread(d, 1603);
t1= Lookup_Thread(d, 71);
thre1=Lookup_Thread(d, 167);

//pipe #1
//mass flow rate and temperature of air at the pipe inlet
begin_f_loop(f,t1)
{
flow+=F_FLUX(f,t1);
temp=temp+F_T(f,t1)*F_FLUX(f,t1);
}
end_f_loop(f,t1)
//flow-weighted temperature
temperature=temp/flow;
//pipe heat power
if (flow >0.0)
{
moc=(-1118839*pow(flow,2.0)+34691*flow)*moc_wsp;
}
if (flow <0.0)
{
```

```
flow=-1.0*flow;
moc=(-1118839*pow(flow,2.0)+34691*flow)*moc_wsp;
}
//air temperature correction factor
poprawka_t=1.0+(298.15-temperature)*0.0129;
//total heat power
begin_f_loop(f,thread1)
{
nfaces1=nfaces1+1;
}
end_f_loop(f,thread1)
sum_nfaces=nfaces1+nfaces2+nfaces3;
begin_f_loop(f,thread1)
{
cisnienie_pary=C_YI(F_C0(f,thread1),THREAD_T0(thread1),0)*cisnienie_ot;
temperatura=22.0*log(cisnienie_pary)+371.66;
if (temperatura<300.0)
{
temperatura=300.0;
}
poprawka_s=1.0+(temperatura-373.15)*0.013;
C_UDMI(F_C0(f,thread1),THREAD_T0(thread1),0)=1.0/sum_nfaces*moc*
    poprawka_t*poprawka_s;
cieplo=cieplo+1.0/sum_nfaces*moc*poprawka_t*poprawka_s*C_YI(F_C0(f,
    thread1),THREAD_T0(thread1),0);
}
end_f_loop(f,thread1)
//temperature increase
deltaT=cieplo/cp/flow+temperature;
temp_vect[1]=deltaT;
temp=0.0;
cieplo=0.0;
flow=0.0;
moc=0.0;
nfaces1=0;
nfaces2=0;
nfaces3=0;
sum_nfaces=0;
temperature=0.0;
deltaT=0.0;
//mean temperature
thre2=Lookup_Thread(d,1719);
```

```c
begin_c_loop(c,thre2)
{
den_vol=C_VOLUME(c,thre2)*C_R(c,thre2);
den_vol_sum=den_vol_sum+den_vol;
den_vol_temp=C_VOLUME(c,thre2)*C_R(c,thre2)*C_T(c,thre2);
den_vol_temp_sum=den_vol_temp_sum+den_vol_temp;
}
end_c_loop(c,thre2)
temperatura_pary=den_vol_temp_sum/den_vol_sum;
//wall_p2_WC_st
thread1= Lookup_Thread(d, 2183);
alpha_konw=5.3;
alpha_kond=4000;
lambda=15;
delta=0.001;
pole_p=2.7144e-002;
temperatura_pow=299.25;    //26.1
strumien=pole_p*1.0/(1.0/alpha_konw+1.0/alpha_kond+delta/lambda)*(temperatura_pary-temperatura_pow);
//cell quantity
begin_f_loop(f,thread1)
{
nfaces1=nfaces1+1;
}
end_f_loop(f,thread1)
begin_f_loop(f,thread1)
{
docudmi=1.0/nfaces1*strumien*C_YI(F_C0(f,thread1),THREAD_T0(thread1),0);
C_UDMI(F_C0(f,thread1),THREAD_T0(thread1),6)=docudmi;
strumien_posredni=strumien_posredni+docudmi;
}
end_f_loop(f,thread1)
strumien_calk=strumien_calk+strumien_posredni;
nfaces1=0;
strumien_posredni=0;
//air-side
thread1= Lookup_Thread(d, 1770);
//cell quantity
begin_f_loop(f,thread1)
{
nfaces1=nfaces1+1;
}
```

```
end_f_loop(f,thread1)
begin_f_loop(f,thread1)
{
C_UDMI(F_C0(f,thread1),THREAD_T0(thread1),5)=(1.0/nfaces1)*(strumien_calk);
}
end_f_loop(f,thread1)
}
DEFINE_SOURCE(zrodlo_energii_powietrza, c, t, dS, eqn)
{
double source;
source=C_UDMI(c,t,5) /C_VOLUME(c,t);
C_UDMI(c,t,9)=source;
C_UDMI(c,t,10)=source*C_VOLUME(c,t);
dS[eqn]=0.0;
return source;
}

DEFINE_SOURCE(zrodlo_sciany_WC, c, t, dS, eqn)
{
double source;
double entalpia;
entalpia=2257000+4190*(100.0-70.0);
source=-1.0*C_UDMI(c,t,6)/entalpia/C_VOLUME(c,t);
C_UDMI(c,t,7)=source;
dS[eqn]=0.0;
return source;
}

DEFINE_SOURCE(zrodlo_energii_scianyWC, c, t, dS, eqn)
{
double source;
double entalpia;
double cppary=2014;
source=C_UDMI(c,t,7)*cppary*(C_T(c,t)-298.15);
C_UDMI(c,t,11)=source;
dS[eqn]=C_UDMI(c,t,7)*cppary;
return source;
}

DEFINE_SOURCE(zrodlo, c, t, dS, eqn)
{
```

```
double source;
double entalpia;  //evaporation enthalpy in 100C, J/kg
entalpia=2257000+4190*(100.0-70.0); //term after "+" denotes condensate subcooling
source=-1.0*C_UDMI(c,t,0)*C_YI(c,t,0)/entalpia/C_VOLUME(c,t);
C_UDMI(c,t,1)=source; //maximal pipe power, W
C_UDMI(c,t,2)=source*C_VOLUME(c,t); //condensate mass flow rate, kg/s
C_UDMI(c,t,8)=source*entalpia*C_VOLUME(c,t);  //actual pipe power
dS[eqn]=0.0;
return source;
}

DEFINE_SOURCE(zrodlo_energii, c, t, dS, eqn)
{
double source;
double cppary=2014; //steam specific heat
double chlodz_pow;
double ent_fiz_pary;
chlodz_pow=0.0;
ent_fiz_pary=C_UDMI(c,t,1)*cppary*(C_T(c, t) - 298.15);
source = ent_fiz_pary+chlodz_pow; //performing the equation: mass flow rate*specific heat*temperature difference //unit: W/m3
C_UDMI(c,t,3)=chlodz_pow;
C_UDMI(c,t,4)=ent_fiz_pary;
dS[eqn] = C_UDMI(c,t,1)*cppary;
return source;
}

DEFINE_PROFILE(hflux_rurek,t,i)
{
face_t f;
   begin_f_loop(f,t)
   {
   F_PROFILE(f,t,i)=-(1.0)*(1-C_YI(F_C0(f,t),THREAD_T0(t),0))*(C_T(F_C0(f,t),THREAD_T0(t)) - 313.65)/0.6;
   }
   end_f_loop(f,t)
}

DEFINE_PROFILE(hflux_wymiennika,t,i)
{
face_t f;
```

```
  begin_f_loop(f,t)
  {
  F_PROFILE(f,t,i)=-(1.0)*(1-C_YI(F_C0(f,t),THREAD_T0(t),0))*(C_T(F_C0(f,
    t),THREAD_T0(t)) - 313.65)/0.6;
  }
  end_f_loop(f,t)
}
```

Appendix B

UDF - OC/MC internally finned pipe model

```c
#include ”udf.h”
#define podrelaksacja 0.01

DEFINE_PROFILE(rurka1,t,i)
{
real outlet_0=0;
real outlet_1=0;
real outlet_final=0;
int curr_iter;
face_t f;
Domain *d;
Thread *thread;
d = Get_Domain(1);
thread= Lookup_Thread(d, 71);
curr_iter=N_ITER;

if (curr_iter >300.0)
{
  begin_f_loop(f,thread)
  {
  outlet_1+=F_FLUX(f,thread);
  }
  end_f_loop(f,thread)
  begin_f_loop(f,t)
  {
```

```
  outlet_0+=F_FLUX(f,t);
  }
  end_f_loop(f,t)
  outlet_0=outlet_0*(-1.0);
  begin_f_loop(f,t)
  {
  outlet_final=outlet_0*(1-podrelaksacja)+outlet_1*podrelaksacja;
  F_PROFILE(f,t,i)=outlet_final;
  }
  end_f_loop(f,t)
}
if (curr_iter <=300.0)
{
  begin_f_loop(f,t)
  {
  outlet_final=0.0045;
  F_PROFILE(f,t,i)=outlet_final;
  }
  end_f_loop(f,t)
}
}

DEFINE_PROFILE(koncentracja_rurka1,t,i)
{
face_t f;
Domain *d;
Thread *thread;
real fan_flow_1=0.0;
real fan_conc_1=0.0;
real concentration=0.0;
d = Get_Domain(1);
thread= Lookup_Thread(d, 71);
begin_f_loop(f,thread)
{
fan_flow_1+=F_FLUX(f,thread);
fan_conc_1=fan_conc_1+F_FLUX(f,thread)*F_YI(f,thread,0);
}
end_f_loop(f,thread)
concentration=fan_conc_1/fan_flow_1;
begin_f_loop(f,t)
{
F_PROFILE(f,t,i)=concentration;
```

```
}
end_f_loop(f,t)

}

DEFINE_PROFILE(temperatura_rurka1,t,i)
{
face_t  f;
begin_f_loop(f,t)
{
F_PROFILE(f,t,i)=temp_vect[1];
}
end_f_loop(f,t)
}
```

Appendix C

UDF - Fan model

```c
#include ”udf.h”
#define podrelaksacja 0.8

DEFINE_PROFILE(wentylator,t,i)
{
real fan_outlet_1=0.0;
real fan_outlet_2=0.0;
real fan_outlet=0.183958928198223;
real fan_outlet_real=0.0;
real fan_inlet=0.0;
real fan_inlet_moisture=0.0;
real fan_inlet_dair=0.0;
int curr_iter;
real p;
real p_old;
face_t f;
Domain *d;
Thread *thread;
Thread *th;
d = Get_Domain(1);
thread= Lookup_Thread(d, 679);
th= Lookup_Thread(d, 680);

begin_f_loop(f,thread)
{
  fan_outlet_1+=F_FLUX(f,thread);
}
end_f_loop(f,thread)
```

```

begin_f_loop(f,th)
{
  fan_outlet_2+=F_FLUX(f,th);
}
end_f_loop(f,th)

begin_f_loop(f,t)
{
  fan_inlet+=F_YI(f,t,1)*F_FLUX(f,t);
}
end_f_loop(f,t)

curr_iter=N_ITER;

fan_inlet=pow(pow(fan_inlet,2),0.5);

if (curr_iter <=20.0)
{
p=0.94;
C_UDMI(1,t,12)=p;
}

if (curr_iter >20.0)
{
  p=(C_UDMI(1,t,12)-podrelaksacja)+podrelaksacja*(fan_outlet/fan_inlet);
}

C_UDMI(1,t,12)=p;

F_PROFILE(0,t,i)=6.4468*p;
.
.
.
F_PROFILE(1157,t,i)=2.4034*p;
}

DEFINE_PROFILE(koncentracja_went,t,i)
{
face_t f;
Domain *d;
Thread *thread;
```

```
Thread *th;
real fan_flow_1=0.0;
real fan_flow_2=0.0;
real fan_conc_1=0.0;
real fan_conc_2=0.0;
real concentration=0.0;
d = Get_Domain(1);
thread= Lookup_Thread(d, 679);
th= Lookup_Thread(d, 680);
begin_f_loop(f,thread)
{
fan_flow_1+=F_FLUX(f,thread);
fan_conc_1=fan_conc_1+F_FLUX(f,thread)*F_YI(f,thread,0);
}
end_f_loop(f,thread)
begin_f_loop(f,th)
{
fan_flow_2+=F_FLUX(f,th);
fan_conc_2=fan_conc_2+F_FLUX(f,th)*F_YI(f,th,0);
}
end_f_loop(f,th)
concentration=(fan_conc_1+fan_conc_2)/(fan_flow_1+fan_flow_2);
begin_f_loop(f,t)
{
F_PROFILE(f,t,i)=concentration;
}
end_f_loop(f,t)
}

DEFINE_PROFILE(temperatura_went,t,i)
{
face_t f;
Domain *d;
Thread *thread;
Thread *th;
real fan_flow_1=0.0;
real fan_flow_2=0.0;
real fan_temp_1=0.0;
real fan_temp_2=0.0;
real went_temp=0.0;
d = Get_Domain(1);
thread= Lookup_Thread(d, 679);
```

```
th= Lookup_Thread(d, 680);
begin_f_loop(f,thread)
{
fan_flow_1+=F_FLUX(f,thread);
fan_temp_1=fan_temp_1+F_FLUX(f,thread)*F_T(f,thread);
}
end_f_loop(f,thread)
begin_f_loop(f,th)
{
fan_flow_2+=F_FLUX(f,th);
fan_temp_2=fan_temp_2+F_FLUX(f,th)*F_T(f,th);
}
end_f_loop(f,th)
went_temp=(fan_temp_1+fan_temp_2)/(fan_flow_1+fan_flow_2);
begin_f_loop(f,t)
{
F_PROFILE(f,t,i)=went_temp;
}
end_f_loop(f,t)

}
```

Appendix D

UDF - RC externally finned pipe model

```
#include "udf.h"
#define podrelaksacja 0.01
DEFINE_EXECUTE_AT_END(zrodla_koniec)    //calculating source terms of the pipes
{
//UDM 0 - condensation heat in a single cell
//UDM 1 - air-air heat transfer rate in a single cell
//UDM 2 - total heat transferred to air (sum of udm0 and udm1), W/M3
//UDM 3 - condensate flow rate kg/s in a single cell (total condensate flow rate obtained after summation over all cells)
//UDM 4 - steam physical enthalpy removed from a single cell

face_t f;
cell_t c;
Domain *d;
Thread *tf1;
Thread *tc1;

real temperature_air;      //mean air temperature in the inter-fin space
real temperature_steam;      //mean steam temperature near-wall
real mianownik;
real mianownik_suma=0;
real licznik;
real licznik_suma=0;
real objetosc_calkowita=0.0;
real temperature_in;       //mean temperate at the pipe inlet
```

```
real temperature_s;          //mean wall pipe temperature on the steam-side
real temperature_s_fin;      //mean wall pipe temperature on the fin-side
real temperature_out;      //mean temperature at the pipe outlet
real temperature_bulk;       //mean temperature at the pipe inlet and outlet
real temperature_in_fin;     //mean temperature at the bundle inlet
real temperature_out_fin;    //mean temperature at the bundle outlet
real temperature_bulk_fin;     //mean temperature at the bundle inlet and outlet - for material properties derival
real velocity_max=0.0;
real v_loc;

real temperature_ave;      //mean pipe wall-steam temperatre - for material properties derival
real rho_water;
real rho_steam;
real entalpia_parowania;
real lambda_water;
real mi_water;
real cp_water;
real gravity=9.81;
real alpha_skr_podstawa;

real velocity_in;
real ve_air;
real density_air;
real Pr_air;
real lambda_air;
real Re_air_pipe;
real Nusselt_air_pipe;

real ve_air_fin;
real density_air_fin;
real Pr_air_fin;
real lambda_air_fin;
real Re_air_fin;
real Nusselt_air_fin;
real Pr_air_fin_s;
real poprawka;

real opor_calkowity;
```

```
real alpha_air=65.925258;
real alpha_skr=9415.368517;
real alpha_air_pipe=20.955153;
real delta_wall=0.0015;
real diameter_in=0.025;
real lambda=160.0;
real dlugosc_zebra=0.01085;
real grubosc_zebra=0.0005;
real podzialka_szczyt=0.00254;
real s_dolina=0.00204;
real sprawnosc_zebra=0.95;
real liczba_pi=3.14;
real m_zebro;
real A_r;
real liczba_zeber;
real Lnz;
real Anz;
real Az;
real korekcja_alphy;
real Rkond;
real Rsciany;
real Rpow;
real Rpow_wew;

//pipe_length=0.234 m;
//pole_powierzchni_rury=0.02113373 m2;
real dlugosc_rury_1_1=0.234;
real pole_powierzchni_rury_1_1=0.02113373;
real dlugosc_rury_1_2=0.237;
real pole_powierzchni_rury_1_2=0.02139687;

real q_max_steam;
real q_cell_steam;
real area_pipe[ND_ND];
real area_value_pipe;
real Cieplo_steam=0.0;
real moc_steam;

real opor_calkowity_air;

real q_max_air;
real q_cell_air;
```

```
real Cieplo_air=0.0;
real moc_air;
int r11=100.0;  //the last pipe downstream before flow guides
int r21=100.0;
int r31=100.0;
int r41=100.0;
int r51=100.0;  //the last pipe downstream before flow guides
int stale_male_alfy=300.0;  //at first, the UDF runs with small constant
    heat transfer coefficients
int zmienne_alfy=600.0; //secondly, small constant coefficients are
    shifted to high constant coefficients to facilitate stability; finally
     the coefficients are calculated
int r12=100.0;  //the first pipe downstream after flow guides
int r22=100.0;
int r32=100.0;
int r42=100.0;
int r52=100.0;  //the last pipe downstream after flow guides
real cieplo_do_powietrza;
real weight=100.0;
int curr_iter;
curr_iter=N_ITER;



if(curr_iter<stale_male_alfy)
{
alpha_air=50.0;
alpha_skr=5000.0;
alpha_air_pipe=5.0;
}
d=Get_Domain(1);


tf1=Lookup_Thread(d,93);

begin_f_loop(f,tf1)
{
mianownik=C_R(F_C0(f,tf1),THREAD_T0(tf1))*C_VOLUME(F_C0(f,tf1),THREAD_T0(
    tf1));
licznik=C_R(F_C0(f,tf1),THREAD_T0(tf1))*C_VOLUME(F_C0(f,tf1),THREAD_T0(
    tf1))*C_T(F_C0(f,tf1),THREAD_T0(tf1));
mianownik_suma=mianownik_suma+mianownik;
```

```
licznik_suma=licznik_suma+licznik;
}
end_f_loop(f,tf1)

temperature_in_fin=licznik_suma/mianownik_suma; //mass weighted steam temperature at the pipe inlet

licznik_suma=0;
mianownik_suma=0;




tf1=Lookup_Thread(d,69);

begin_f_loop(f,tf1)
{
mianownik=C_R(F_C0(f,tf1),THREAD_T0(tf1))*C_VOLUME(F_C0(f,tf1),THREAD_T0(tf1));
licznik=C_R(F_C0(f,tf1),THREAD_T0(tf1))*C_VOLUME(F_C0(f,tf1),THREAD_T0(tf1))*C_T(F_C0(f,tf1),THREAD_T0(tf1));
mianownik_suma=mianownik_suma+mianownik;
licznik_suma=licznik_suma+licznik;
}
end_f_loop(f,tf1)

temperature_out_fin=licznik_suma/mianownik_suma;
licznik_suma=0;
mianownik_suma=0;

if(curr_iter>r11)
{
//PIPE #1_1_dol
//temperature of air in the inter-fin spaceO
tc1=Lookup_Thread(d,266);     e

begin_c_loop(c,tc1)
{
mianownik=C_R(c,tc1)*C_VOLUME(c,tc1);
licznik=C_R(c,tc1)*C_VOLUME(c,tc1)*C_T(c,tc1);
mianownik_suma=mianownik_suma+mianownik;
licznik_suma=licznik_suma+licznik;
```

```
objetosc_calkowita=objetosc_calkowita+C_VOLUME(c,tc1);
}
end_c_loop(c,tc1)

temperature_air=licznik_suma/mianownik_suma;   //mass weighted average air temperature
licznik_suma=0;
mianownik_suma=0;

//steam temperature near inner wall pipe
tf1=Lookup_Thread(d,506);       //id shadow

begin_f_loop(f,tf1)
{
mianownik=C_R(F_C0(f,tf1),THREAD_T0(tf1))*C_VOLUME(F_C0(f,tf1),THREAD_T0(tf1));
licznik=C_R(F_C0(f,tf1),THREAD_T0(tf1))*C_VOLUME(F_C0(f,tf1),THREAD_T0(tf1))*C_T(F_C0(f,tf1),THREAD_T0(tf1));
mianownik_suma=mianownik_suma+mianownik;
licznik_suma=licznik_suma+licznik;
}
end_f_loop(f,tf1)

temperature_steam=licznik_suma/mianownik_suma;   //mass weighted average steam temperature near wall
licznik_suma=0;
mianownik_suma=0;

//temperature at pipe inlet
tf1=Lookup_Thread(d,39);        //id pipe inlet

begin_f_loop(f,tf1)
{
mianownik=C_R(F_C0(f,tf1),THREAD_T0(tf1))*C_VOLUME(F_C0(f,tf1),THREAD_T0(tf1));
licznik=C_R(F_C0(f,tf1),THREAD_T0(tf1))*C_VOLUME(F_C0(f,tf1),THREAD_T0(tf1))*C_T(F_C0(f,tf1),THREAD_T0(tf1));
mianownik_suma=mianownik_suma+mianownik;
licznik_suma=licznik_suma+licznik;
}
end_f_loop(f,tf1)

```

```
temperature_in=licznik_suma/mianownik_suma;
licznik_suma=0;
mianownik_suma=0;

//temperature pipe outlet
tf1=Lookup_Thread(d,407);      //id pipe outlet

begin_f_loop(f,tf1)
{
mianownik=C_R(F_C0(f,tf1),THREAD_T0(tf1))*C_VOLUME(F_C0(f,tf1),THREAD_T0(tf1));
licznik=C_R(F_C0(f,tf1),THREAD_T0(tf1))*C_VOLUME(F_C0(f,tf1),THREAD_T0(tf1))*C_T(F_C0(f,tf1),THREAD_T0(tf1));
mianownik_suma=mianownik_suma+mianownik;
licznik_suma=licznik_suma+licznik;
}
end_f_loop(f,tf1)

temperature_out=licznik_suma/mianownik_suma;
licznik_suma=0;
mianownik_suma=0;

//mean steam-side wall pipe temperature
tf1=Lookup_Thread(d,506);      //id wall pipe steam-side

begin_f_loop(f,tf1)
{
mianownik_suma=mianownik_suma+1.0;
licznik_suma=licznik_suma+F_T(f,tf1);
}
end_f_loop(f,tf1)

temperature_s=licznik_suma/mianownik_suma;
licznik_suma=0;
mianownik_suma=0;

//mean air-side wall pipe temperature
tf1=Lookup_Thread(d,387);      //id wall pipe air-side

begin_f_loop(f,tf1)
{
mianownik_suma=mianownik_suma+1.0;
```

```
licznik_suma=licznik_suma+F_T(f,tf1);
}
end_f_loop(f,tf1)

temperature_s_fin=licznik_suma/mianownik_suma;
licznik_suma=0;
mianownik_suma=0;

//mean inlet pipe velocity
velocity_in=4; //mean velocity upstream the bundle
licznik_suma=0;
mianownik_suma=0;

//maximal velocity in the air-side
velocity_max=5.93;

//steam and air thermal resistance

//condensation
temperature_s=(weight/(weight+1))*temperature_steam+(1/(weight+1))*
    temperature_air;
temperature_ave=(temperature_steam+temperature_s)/2.0;

//material properties, range 350-375 K
rho_water=-0.0023*pow(temperature_ave,2.0)+0.9811*temperature_ave+910.34;
lambda_water=-0.000007*pow(temperature_ave,2.0)+0.005785*temperature_ave
    -0.457807;
mi_water=-0.000004*temperature_ave+0.001656;
cp_water=1000*(0.000007*pow(temperature_ave,2.0)-0.003921*temperature_ave
    +4.685714);
rho_steam=0.000216*pow(temperature_ave,2.0)-0.141948*temperature_ave
    +23.425225;
entalpia_parowania=1000*(-0.003571*pow(temperature_ave,2.0)+0.017857*
    temperature_ave+2747.430);

alpha_skr_podstawa=gravity*rho_water*(rho_water-rho_steam)*pow(
    lambda_water,3.0)/(mi_water*(temperature_steam-temperature_s))*(
    entalpia_parowania+3.0/8.0*cp_water*(temperature_steam-temperature_s))
    ;

//air in the pipe
//material properties, range 273-373 K
```

```c
temperature_bulk=(temperature_in+temperature_out)/2.0;

ve_air=(0.000101*pow(temperature_bulk,2.0)+0.031962*temperature_bulk-2.982390)/1000000.0;
density_air=0.000010*pow(temperature_bulk,2.0)-0.009617*temperature_bulk+3.205387;
Pr_air=-0.000110*temperature_bulk+0.745380;
lambda_air=0.000071*temperature_bulk+0.004965;

Re_air_pipe=diameter_in*velocity_in/ve_air;

Nusselt_air_pipe=0.023*pow(Re_air_pipe,0.8)*pow(Pr_air,1.0/3.0);

//air outside the pipe
temperature_bulk_fin=(temperature_in_fin+temperature_out_fin)/2.0;

//material properties, range 273-373 K
lambda_air_fin=0.000071*temperature_bulk_fin+0.004965;
density_air_fin=0.000010*pow(temperature_bulk_fin,2.0)-0.009617*temperature_bulk_fin+3.205387;
ve_air_fin=(0.000101*pow(temperature_bulk_fin,2.0)+0.031962*temperature_bulk_fin-2.982390)/1000000.0;
Pr_air_fin=-0.000110*temperature_bulk_fin+0.745380;
Pr_air_fin_s=-0.000110*temperature_s_fin+0.745380;

Re_air_fin=(diameter_in+2.0*delta_wall)*velocity_max/ve_air_fin;

if (Re_air_fin>200000.0)
{
Nusselt_air_fin=0.033*pow(Re_air_fin,0.8)*pow(Pr_air_fin,0.4)*pow(Pr_air_fin/Pr_air_fin_s,0.25);
}

if (Re_air_fin<200000.0)
{
Nusselt_air_fin=0.27*pow(Re_air_fin,0.63)*pow(Pr_air_fin,0.36)*pow(Pr_air_fin/Pr_air_fin_s,0.25);
}

if (Re_air_fin<1000.0)
{
Nusselt_air_fin=0.52*pow(Re_air_fin,0.5)*pow(Pr_air_fin,0.36)*pow(
```

```
    Pr_air_fin/Pr_air_fin_s,0.25);
}

if  (Re_air_fin <100.0)
{
Nusselt_air_fin=0.9*pow(Re_air_fin ,0.4)*pow(Pr_air_fin ,0.36)*pow(
    Pr_air_fin/Pr_air_fin_s,0.25);
}


poprawka=0.93;          //correction factors in regard of pipe position in
    the bundle
        //row 1 - 0.7
        //row 2 - 0.8
        //row 3 - 0.86
        //row 4 - 0.9
        //row 5 - 0.93



m_zebro=pow(2.0*alpha_air/grubosc_zebra/lambda,0.5);
A_r=dlugosc_rury_1_1*liczba_pi*(diameter_in+2.0*delta_wall);
liczba_zeber=dlugosc_rury_1_1/podzialka_szczyt;
Lnz=dlugosc_rury_1_1-liczba_zeber*grubosc_zebra;
Anz=Lnz*liczba_pi*(diameter_in+2.0*delta_wall);
Az=liczba_pi*2.0/4.0*(pow(diameter_in+2.0*delta_wall+2.0*dlugosc_zebra
    ,2.0)-pow(diameter_in+2*delta_wall,2.0));

korekcja_alphy=(Anz+liczba_zeber*Az*sprawnosc_zebra)/A_r;

Rkond=1.0/(liczba_pi*diameter_in*alpha_skr);
Rpow_wew=1.0/(liczba_pi*diameter_in*alpha_air_pipe);
Rsciany=log((diameter_in+2.0*delta_wall)/diameter_in)/(2.0*liczba_pi*
    lambda);
Rpow=1.0/(liczba_pi*(diameter_in+2.0*delta_wall)*alpha_air*korekcja_alphy
    );

opor_calkowity=Rkond+Rsciany+Rpow;
opor_calkowity_air=Rpow_wew+Rsciany+Rpow;


//total heat transfer rate for steam
```

```
tf1=Lookup_Thread(d,506);          //!!!!!!!!!!!

q_max_steam=(temperature_steam-temperature_air)/opor_calkowity*dlugosc_rury_1_1;

  q_max_steam=q_max_steam*podrelaksacja+(1-podrelaksacja)*C_UDMI(F_C0(9,tf1),THREAD_T0(tf1),5);
  C_UDMI(F_C0(9,tf1),THREAD_T0(tf1),5)=q_max_steam;


q_cell_steam=q_max_steam/pole_powierzchni_rury_1_1;      //divided by pipe area to multiple by cell area later

begin_f_loop(f,tf1)
{
F_AREA(area_pipe,f,tf1);
area_value_pipe=NV_MAG(area_pipe);          //single cell area at the tf1 BC
moc_steam=C_YI(F_C0(f,tf1),THREAD_T0(tf1),0)*q_cell_steam*area_value_pipe;
if(moc_steam<0)
{
  moc_steam=0.0;
}
C_UDMI(F_C0(f,tf1),THREAD_T0(tf1),0)=moc_steam;
Cieplo_steam=Cieplo_steam+moc_steam;
}
end_f_loop(f,tf1)

//total heat transfer rate for the air in the pipe
tf1=Lookup_Thread(d,506);          //!!!!!!!!!!!

q_max_air=(temperature_steam-temperature_air)/opor_calkowity_air*dlugosc_rury_1_1;

q_cell_air=q_max_air/pole_powierzchni_rury_1_1;

begin_f_loop(f,tf1)
{
F_AREA(area_pipe,f,tf1);
area_value_pipe=NV_MAG(area_pipe);
moc_air=(1.0-C_YI(F_C0(f,tf1),THREAD_T0(tf1),0))*q_cell_air*
```

```
    area_value_pipe;
C_UDMI(F_C0(f,tf1),THREAD_T0(tf1),1)=moc_air;
Cieplo_air=Cieplo_air+moc_air;
}
end_f_loop(f,tf1)

//total heat transfer flux from the pipe to the coolant air (W/M3)
tc1=Lookup_Thread(d,266);       // id fin cell zone

cieplo_do_powietrza=(Cieplo_steam+Cieplo_air)/objetosc_calkowita;

begin_c_loop(c,tc1)       //tc1 is an air domain id in the fin cell zone
{
C_UDMI(c,tc1,2)=cieplo_do_powietrza;

}
end_c_loop(c,tc1)
if(cieplo_do_powietrza<0)
{
  cieplo_do_powietrza=0;
}
```

Abstract

This PhD Thesis was carried out as part of the project POIR.03.02.01-18-0019/15-00 financed by the Polish Agency for Enterprise Development, in cooperation with an industrial partner - Retech Ltd. The project, titled *Implementation of anew generation of condensation hoods for combi-steamer* covers development of a new generation of condensation hood by means of computational fluid dynamics (CFD).

The condensation hood (CH) is a device widely used in gastronomy. It is designed to work with a combi steamer (CS) that produces a significant amount of steam. The steam is condensed by the CH in a dedicated heat exchanger (HE) and is returned to the oven that enables free relocation of the CS and allows for its normal operation without appropriate infrastructure. The steam has direct contact with food in the CS working chamber, and hence it can carry solid particles, grease droplets, and scents. The condensation hood captures them to avoid the nearest surroundings additional pollution. This, however, is not the subject of this dissertation.

Already mentioned heat exchanger, in which the CH is equipped with, has a non-standard construction: it consists of two bundles of internally finned tubes - 24 per bundle (48 in total). This results from the flow organisation, where coolant air flows through the pipes, while the steam around them contacts with their smooth outer surface. From the heat transfer point of view, such a solution has several drawbacks: firstly, the diameter of the tube (as well as the technological limitations) limits the number and geometry of the fins (which limits the overall heat transfer surface); secondly, the inner fins increase the tube's flow resistance; and thirdly, the steam flowing across the bundle in the inter-pipe space has low velocity ($\leqslant$1 m/s), which makes contact with the pipe's wall more difficult.

For the purposes of the project, and as part of this work, three condensation hood models were developed. All three models utilise user-defined functions (UDF) to perform the process of steam condensation and its heat exchange with the coolant air.

The simulations were steady-state with the use of the species transport model, which was enabled because of the implemented UDF. The main idea of the UDF was to remove the condensed steam from the computational domain, so the flow could remain gaseous. This allowed to reduce the mesh size by approximately an order of magnitude. The turbulent flow was calculated in the standard k-ε model using the standard wall function. Implementation of the UDF enabled not only a single phase flow simulation, but also allowed for the project's completion within limited resources and time.

The first numerical model concerns the original CH already produced by Retech company. In this work, it is denoted as OC - original construction. It was developed to validate the UDF model and to diagnose the actual device. As the condensation hood turned out to be overestimated, but with a very high condensation efficiency, amounting to approx. 90%, it was decided not to improve such high efficiency, and instead the focus was laid on simplifying the construction. The improvements developed in such direction were implemented in the second model.

The second numerical model (denoted as MC - modified construction) is an implementation of the most promising improvements to the HE design. Those improvements include: removal of 12 from 48 pipes, which equals to 25% of overall heat transfer surface - as a result total pipe length was reduced from 13.5 m (OC) to 10.1 m (MC) - which allowed to improve the steam distribution in the HE and to reduce manufacturing cost; modification of the size and location of the steam side baffles to extend the steam residence time in the inter-pipe space. Once the results were satisfactory, i.e., the condensation efficiency was maintained at 90%, it was decided to build a prototype, which was then successfully validated.

The last (third) numerical model is marked as RC - redesigned (new) construction. In this concept, the cooling air is rearranged so that it flows around the tubes and the steam flows inside them. This allowed to utilise tubes with external fins and reduce their number from the original 48 to only 5. Compared to the previous design, both bundles were merged into one large additionally equipped with an air side flow guide to enhance air distribution in the inter-pipe space. Total pipe length was reduced from 13.5 m (OC) to just 4.7 m (RC). As the obtained results were very optimistic, a new prototype was built, tested, and the model was validated. The RC is able to condense over 15% more steam, when compared to the original CH.

The redesigned construction was used as a basis for Retech in designing two new concepts of condensation hoods that are now in the company's offer.

Streszczenie

Niniejsza praca doktorska została zrealizowana w ramach projektu POIR.03.02.01-18-0019/15-00 sfinansowanego przez Polską Agencję Rozwoju Przedsiębiorczości we współpracy z partnerem przemysłowym - firmą Retech Sp. z o.o. Projekt, o tytule *Wdrożenie do produkcji nowej generacji pochłaniaczy pary do pieców konwekcyjno-parowych*, zakładał opracowanie nowej konstruckji pochłaniacza pary z wykorzystaniem metod numerycznych, co jest głównym przedmiotem tej rozprawy.

Pochłaniacz pary to urządzenie cieplno-przepływowe szeroko stosowane w gastronomii. Zaprojektowane jest do współpracy z piecami konwekcyjno-parowymi produkującymi znaczne ilości pary wodnej. Pochłaniacz pary wyposażony jest w odpowiedni wymiennik ciepła, który umożliwia wychwycenie pary wodnej pochodzącej z pieca, skroplenie jej i skierowanie z powrotem do pieca. Umożliwia to swobone przestawianie pieca oraz pozwala na jego normalną pracę bez odpowiedniej infrastruktury. Para produkowana przez piec ma bezpośredni kontakt z potrawami w komorze roboczej pieca, co sprawia, że towarzyszyć jej mogą cząsteczki stałe i krople tłuszczu, które mogą być również nośnikami zapachów. Dodatkową funkcją pochłaniacza pary jest wychwytywanie tych cząstek, kropel i zapachów tak, by nie doszło do zanieczyszczenia pomieszczenia - jest to jednak funkcja dodatkowa i nie jest przedmiotem ani projektu ani tej rozprawy.

Wspomniany wymiennik ciepła, w jaki wyposażony jest pochłaniacz pary, ma niestandardową konstrukcję: składa się z dwóch pęczków po 24 wewnętrznie żebrowane rurki z powodu powietrza chłodzącego, które płynie rurkami. Para wodna natomiast opływa rurki z zewnątrz kontaktując się z ich gładką powierzchnią zewnętrzną. Z punktu widzenia wymiany ciepła jest to rozwiązanie niekorzystne z kilku powodów: po pierwsze, średnica rurki (jak również kwestie technologiczne) ogranicza wymiary i liczbę żeber, co ogranicza możliwość rozwinięcia powierzchni ciepła w takim rozwiązaniu; po drugie, wewnętrzne żebra zwiększają opory przepływu przez rurkę; i po trzecie, para wodna opływając rurki w przestrzeni między rurkowej ma niską prędkość (¡1 m/s),

co negatywnie wpływa na jej kontakt ze ścianką rurki.

Na potrzeby projektu - a w ramach tej pracy - opracowano trzy modele numeryczne pochłaniacza pary. Wszystkie trzy oparto o funkcje użytkownika UDF realizujące proces kondensacji pary wodnej oraz jej wymiany ciepła z powietrzem będacym czynnikiem chłodniczym. Symulacje wykonano w stanie ustalonym wykorzystując model species transport, co było możliwe dzięki zastosowaniu wspomnianych UDF-ów. Główną ideą modelu UDF było usuwanie z domeny obliczeniowej skroplonej pary wodnej, co pozwoliło liczyć tylko fazę gazową. To z kolei pozwoliło zmniejszyć rozmiar siatki o ok. rząd wielkości. Symulowano przepływ turbulentny modelem standard k-ε przy użyciu standard wall function. Zaimplementowanie modelu kondensacji i transportu ciepła przy pomocy UDF nie tylko pozwoliło uniknąć modelowania przepływu wielofazowego ze zmianą fazy i, co za tym idzie, zastosować mniejszą siatkę numeryczną, ale w ogóle policzyć opracowane modele dysponując ograniczonymi zasobami obliczeniowymi i ograniczonym czasem.

Pierwszy opracowany model numeryczny dotyczył oryginalnego pochłaniacza pary już produkowanego przez firmę Retech. W pracy oznaczony został jako OC - oryginal construction. Model ten posłużył do zwalidowania modelu UDF oraz do zdiagnozowania rzeczywistego urządzenia pod kątem potencjalnych zmian konstrukcji wymiennika ciepła. Jako, że pochłaniacz pary okazał się być przewymiarowany, ale o bardzo wysokiej sprawności wykraplania wynoszącej ok. 90%, postanowiono nie poprawiać już wysokiej sprawności, a zamiast tego skupić się na utrzymaniu jej na stałym poziomie przy jednoczesnym odchudzeniu konstrukcji. W tym kierunku opracowano zmiany konstrukcyjne, które zostały potem przeniesione do drugiego modelu.

Drugi model numeryczny (oznaczony jako MC - modified construction) stanowi implementację wyselekcjonowanych i najbardziej obiecujących zmian konstrukcyjnych wymiennika ciepła. Zmiany te obejmują: usunięcie 12 z 48 rurek, co stanowi 25% ogółu powierzchni wymiany ciepła i odpowiada zredukowaniu łącznej długości rur z 13.5 m do 10.1 m, w celu poprawy rozpływu pary wodnej po pęczkach rurek i obniżenia kosztów produkcji; zmiana wymiarów i lokalizacji przegród po stronie parowej tak, aby wydłużyć czas kontaktu pary wodnej z rurkami. Gdy otrzymane wyniki okazały się być zadowalające, tzn. sprawność wykraplania była na poziomie 90%, zdecydowano o budowie egzemplarza prototypowego na podstawie wytycznych z modelu numerycznego, który następnie został z sukcesem zwalidowany.

Ostatni, trzeci, model numeryczny oznaczono jako RC - redesigned (new) construc-

tion. W koncepcji tej przeorganizowano wymiennik ciepła tak, aby to powietrze opływało rurki, a para wodna płynęła wewnątrz nich. Pozwoliło to na zastosowanie rurek zewnętrznie żebrowanych oraz na ograniczenie ich liczby z pierwotnych 48 (o łącznej długości 13.5 m) do zaledwie 5 (o długości 4.7 m). W rezultacie, dotychczasowe dwa pęczki rurek połączono w jeden duży wyposażony w kierownicę po stronie powietrza. Wyniki symulacji numerycznej okazały się być bardzo optymistyczne, więc zbudowano odpowiedni prorotyp i wykonano pomiary, którymi zwalidowano model. Okazało się, że nowa konstrukcja wykrapla o ponad 15% więcej pary wodnej, niż oryginalny pochłaniacz pary będąc przy tym znacznie prostszą.

Na podstawie rozwiązań z trzeciej konstrukcji (RC) Firma zaprojektowała dwie nowe wersje pochłaniacza pary znajdujące się obecnie w Jej ofercie.